

**High Energy Particle Telescope Suite Design: Electron Microburst
Detector and Read-out Electronics**

by

Anant Kumar Telikicherla Kandala

A thesis submitted in partial fulfillment of the requirements for the degree of

Master of Science

in

Photonics and Plasmas

Departments of Electrical and Computer Engineering and Physics
University of Alberta

© Anant Kumar Telikicherla Kandala, 2024

Abstract

In-situ measurements of energetic particle precipitation in the near-Earth space environment are essential for understanding the governing physical processes responsible for this precipitation, as well as to elucidate the possible impacts of space radiation on the Earth's atmosphere. This thesis describes the design elements of a High Energy Particle Telescope, which is being developed to fly onboard the RAdiation Impacts on Climate and Atmospheric Loss Satellite (RADICALS) mission. The particular focus of this thesis is the design and development of two components of the particle telescope: (a) a miniaturized radiation detector and (b) accompanying signal processing electronics. The designed detector is a novel multi-pixel photon counter (silicon photomultiplier) based scintillation detector, that is optimized to measure electron microbursts, which are bursty and short timescale (< 1 s) bursts of electron precipitation arising from the scattering of energetic (having energies ranging from a few keV to MeV) electrons from the Van Allen belts into the Earth's atmosphere. The detector can resolve sub-relativistic and relativistic microbursts with energies between 200 keV and 3 MeV at 10 ms cadence. The detector and electronics have been designed with a modular architecture enabling use on future cubesats, balloons, sounding rockets and small-satellite missions. A version of this detector has also been realized as a part of the Payload for Energetic Particle Precipitation Education and Research-eXperiment (PEPPER-X), which is slated to launch on the NASA RockSat-X student sounding rocket mission in August 2024. A successful launch on the sounding rocket platform would raise the Technology Readiness Level (TRL) of the detector and electronics, in advance of the RADICALS mission.

Preface

This thesis is an original work by ‘Anant Kumar Telikicherla Kandala’.

Details of the instrument designed, realized and tested for the sounding rocket test flight has been submitted and accepted as a student paper finalist at the 32nd Annual Frank J. Redd Student Competition of the American Institute of Aeronautics and Astronautics SmallSat Conference, to be held from August 3rd to 8th, 2024 in Utah, USA. The paper will be published in the online conference proceedings, and the citation is as follows: Telikicherla, A. 2024. “Miniaturized scintillation based detector for characterizing energetic electron precipitation,” Proceedings of the AIAA/USU Conference on Small Satellites, Frank J. Redd Student Competition, SSC24-VI-03.

Details of the instrument design for the RADICALS microsatellite mission were submitted as a conference paper to the 2024 IEEE Nuclear and Space Radiation Effects Conference (NSREC). The authors and title of the paper are as follows: Anant Telikicherla, Bo Yu, Kai Ernn Gan, John M. Gjevre, Talwinder Kaur Sraw, Henry Tiedje, Robert Fedosejevs, Louis Ozeke, Ian R. Mann; “Design of a miniaturized scintillation detector for energetic electron precipitation measurements on the RADICALS mission”. This paper is being currently prepared for potential publication in the IEEE Transactions on Nuclear Science (TNS) journal after including additional design, calibration, and modelling details.

In both publications, I was responsible for the prototype development, data analysis, and manuscript composition. R. Fedosejevs and I. R. Mann were the supervisors for the whole research presented in this thesis, and reviewed the manuscripts submitted for publication.

Acknowledgements

First and foremost, I would like to thank my supervisors Dr. Robert Fedosejevs and Dr. Ian R. Mann. It has been a pleasure working under their guidance, and their passion for research has motivated me throughout my M.Sc. I thank them for giving me the opportunity to contribute to the development of multiple space missions during my M.Sc. degree.

I would like to thank all RADICALS, SWEPT and PEPPER-X team members: building space missions is a interdisciplinary pursuit and would not be possible without the efforts of these amazing teams. I gratefully acknowledge that the RADICALS mission is funded through grants from the Canadian Space Agency, the Canadian Foundation of Innovation, and the Government of Alberta. I also thank the NASA RockSat-X program for selecting our instrument for a ride onboard their sounding rocket, as well as providing guidance and launch support for PEPPER-X.

I also extend my thanks to all group members of the Space Physics research group as well as the Laser-Plasma research group. I also thank my football (/soccer) friends, my squash club friends, and Juniper house residents who have made my time outside the lab enjoyable. Finally, I would like to thank my parents and my brother, whose constant support and encouragement has enabled me to pursue this thesis.

Table of Contents

1	Introduction	1
1.1	Motivation	1
1.2	RADICALS Mission	5
1.3	High Energy Particle Telescope	5
1.4	Thesis Objectives	7
1.5	Thesis Outline	7
2	Electron Microburst Precipitation	8
2.1	Theory and Background	8
2.2	Particle Motion	10
2.2.1	Gyration	10
2.2.2	Bounce Motion	11
2.2.3	Drift Motion	12
2.3	Energetic Particle Precipitation	13
2.3.1	Microburst Precipitation	14
2.4	Previous Electron Microburst Measurements	17
2.5	Microburst Instrumentation Motivation	19
2.6	Summary and Discussion	20
3	Microburst Detector Design	22
3.1	Microburst Detector Measurement Requirements	22
3.2	Detector Conceptual Overview	22
3.3	Detector Design Elements	24
3.3.1	Silicon Photomultiplier	24
3.3.2	Scintillator	25
3.3.3	Reflector & Optical Glue	26
3.3.4	Mechanical & Thermal Design	27
3.4	Detector Design and Trade-Offs	27
3.4.1	Geometric Factor and Field of View	27

3.4.2	Geometric Factor versus Maximum Measurable Flux	28
3.4.3	Geometric Factor versus Maximum Energy Range	30
3.4.4	Microburst Detector Design and Realization for Sounding Rocket Test flight	32
3.5	Summary and Discussion	34
4	RADHEPT Electronics Design	35
4.1	RADHEPT Electronics Design Requirements	36
4.2	RADHEPT Electronics System Architecture	37
4.2.1	Component Selection Strategy	39
4.3	Power Management Board Design	39
4.4	Digital Processing Board Design	42
4.4.1	System-on-Module (SoM)	43
4.4.2	Peripherals	43
4.5	Detector Interface Board Design	45
4.6	Electronics Unit Realization for the Sounding Rocket Test flight . . .	46
4.7	RADHEPT Electronics Design Summary	50
5	Testing and Calibration	51
5.1	Detector Testing	52
5.1.1	Dark Noise Characterization	52
5.1.2	Radio-isotope Calibration	55
5.2	Electronics Testing	63
5.3	Detector and Electronics Integrated Testing	64
5.3.1	Electronics Unit Telemetry Plots	65
5.4	Environmental Tests	70
5.4.1	Vacuum Tests	70
5.4.2	Vibration Tests	71
5.5	Integrated Instrument Calibration	73
5.5.1	LYSO Self-scintillation	73
5.5.2	Sr-90 Spectrum	75
5.5.3	Ba-133 Spectrum	76
5.6	Discussion and Conclusions	77
6	Summary, Conclusions, and Future Work	82
6.1	Summary and Conclusions	82
6.1.1	Instrument Scientific Performance	84
6.2	Future Work	85

Bibliography	89
Appendix A: RADHEPT Electronics Schematics	95
A.1 Power Management Board	95
A.1.1 Voltage Regulators - Digital Supply	95
A.1.2 Voltage Regulators - Analog Supply	95
A.1.3 Voltage Regulators - High Voltage Bias	96
A.1.4 Housekeeping - Voltage Current Sensors	97
A.1.5 Housekeeping - Thermistor Monitoring	98
A.2 Digital Processing Board	99
A.2.1 Peripherals RS-485/RS-232 Transceivers	99
A.2.2 On-Board Memory	100
A.2.3 Reset Watchdog and Real Time Counter	100
A.3 Detector Interface Board	102
A.3.1 ADC	102

List of Tables

2.1	Previous microburst measurement parameters and proposed goals for the RADICALS micoburst detector.	21
3.1	Comparison of Scintillator Material Properties [33, 34].	27
4.1	RADHEPT Electronics Unit Design Requirements	37
4.2	Component Selection	40
4.3	Digital Processing Board Interfaces.	42
5.1	Estimated responsivity of the three scintillator crystals. These results are calculated using a approximate gain value corresponding to 57V Bias voltage.	77
5.2	Estimated energy ranges of histogram bins of the CsI(Na) crystal . . .	78
5.3	Estimated energy ranges of histogram bins of the LYSO crystal . . .	79
5.4	Radioisotope Source Calibration results	79
6.1	Previous microburst measurement parameters and proposed goals for the RADICALS micoburst detector (SSD = Solid State Detector, SiPM = Silicon Photomultiplier)	84

List of Figures

1.1	Simulated relative change in HO _x (left column), NO _x (middle column), and O ₃ (right column) for the mean (top row) and median Microburst flux (bottom row), during a microburst storm that takes place in the first 6 hours. Time on the x axis is local time from the start of the simulation. Reproduced from reference [9](Seppälä, A., Douma, E., Rodger, C. J., Verronen, P. T., Clilverd, M. A., & Bortnik, J. (2018). Relativistic electron microburst events: Modeling the atmospheric impact. <i>Geophysical Research Letters</i> , 45, 1141–1147, DOI:10.1002/2017GL075949) with permission.	3
1.2	Approaches to Understand Space-Radiation Dynamics. Instrumentation development for in-situ particle measurements is highlighted in green, which is the focus of this thesis	4
1.3	Top: Artistic rendition of the RADICALS mission with different instruments labelled, Image Credit: Andy Kale, Bottom: Overview of RADICALS instruments, text in blue indicates the physical parameter measured by each instrument.	6
2.1	Earth’s Magnetosphere and the Van Allen radiation belts, Source: Van Allen radiation belt, <i>Encyclopedia Britannica</i> , 25 Jan. 2024, https://www.britannica.com/science/Van-Allen-radiation-belt . Accessed 5 March 2024.	9
2.2	Particle Pitch Angle: The yellow arrow indicates velocity vector of the particle, the red arrows indicate the perpendicular and parallel components, and the blue line indicates the magnetic field.	11
2.3	Motion of charged particles due to the Earth’s magnetic field. The figure depicts the three types of particle motion, gyration, bounce, and drift. Figure Credit: Andy Kale.	13

2.4	(a) Microburst precipitation and (b) band precipitation as observed by the Solar, Anomalous, and Magnetospheric Particle Explorer (SAMPEX) satellite taken from reference [17].	15
2.5	Different ways to measure particle precipitation: (1) In-situ electron measurements in the radiation belts, (2) In-situ measurements in low Earth orbit, (3) In-situ measurements using sounding rockets, (4) Remote-sensing using balloon-based measurements of Bremsstrahlung X-rays, (5) Remote-sensing using ground-based instruments (e.g., all-sky imagers, riometers etc).	17
3.1	Microburst Detector Concept: The diagram shows a schematic of the detector, that consists of scintillator crystal mounted on a multi-pixel photon counter, an incoming electron generates multiple photons in the scintillator, that are then counted by the MPPC. The scintillator crystal is coated with Aluminium to reflect photons into the MPPC detector.	23
3.2	MPPC Characteristics (taken from reference [32])	26
3.3	Approximate geometric factor (cm^2str) of a 0.5 cm cubic crystal for different angles of incidence of electrons.	29
3.4	Maximum measurable flux versus size of crystal (cm) for different maximum count rate capabilities of the signal processing electronics. . . .	30
3.5	Maximum Energy measurable with respect to the size of the crystal. . .	31
3.6	Exploded view of the detector design for the PEPPER-X sounding rocket mission. CAD Model Credit: Carl Berresheim, Dept. of Mechanical Engineering, University of Alberta	33
3.7	(a) Zoomed-in picture of the LYSO crystal and MPPC in the prototype (after aluminium and parylene protective coating is added), the crystal and MPPC are to the left of the pasted LYSO text label; (b) The detector prototype during assembly with two scintillator crystals (CsI(Na) and LYSO); (c) The flight model of the detector with the aluminium protective cover added	34
4.1	Schematic showing elements in the RADHEPT electronics readout chain.	35
4.2	RADHEPT Electronics Architecture.	38
4.3	RADHEPT Electronics Powering Scheme.	41
4.4	RADHEPT Electronics Grounding Scheme.	41
4.5	SmartFusion2 SoM Block Diagram [37].	44
4.6	Serial (I2C) Bus for Housekeeping Data Collection.	45

4.7	High Voltage Bias Feedback System.	45
4.8	3D Render of the Power Management Board.	47
4.9	3D Render of the Digital Processing Board.	47
4.10	Electronics Board Stack design for the sounding rocket test flight. CAD Model Credit: Carl Berresheim, Dept. of Mechanical Engineering, University of Alberta.	48
4.11	Top: Power Management Board and Bottom: Digital processing board pictures taken during Flight Model Assembly.	49
5.1	Left: Dark count rate (kcps) variation with temperature, Right: Crosstalk probability variation with overvoltage for an MPPC with 50 micrometer pixel pitch. Reproduced from reference [32], for typical MPPC parameters of M (Gain) = 1.7×10^6 and Temperature of 25 Celsius	53
5.2	Microburst detector Dark noise characterization test setup. (left) Schematic of electrical connections; (right) the test set up as implemented in the laboratory.	54
5.3	Top: LYSO Crystal 1 Photo-electron (PE), 2-PE, 3-PE Pulses (measured using a 50 Ohm termination with the scope); Bottom: Leakage current and self scintillation pulses of the LYSO crystal in the detector, measured using a 1 MOhm termination with the oscilloscope	56
5.4	Top: Schematic of the microburst detector Radioisotope Calibration test setup; Bottom-Left: Implementation of test-setup in the laboratory; Bottom-Right: Zoomed-in picture of the source	58
5.5	Top: Measured LYSO self-scintillation spectrum; Bottom: LYSO self-scintillation spectra for a $1 \times 1 \times 1$ cm ³ crystal (reproduced from reference [40]).	60
5.6	Top: Barium source spectrum observed with the BGO detector; Bottom: Barium reference spectra (reproduced from reference [42]).	61
5.7	Top: Strontium source spectrum with BGO detector; Bottom: Strontium reference spectrum (reproduced from reference [43]).	62
5.8	Electronics testing setup for validating the performance of the electronics digitisation using an analog source signal.	64
5.9	Analog sine wave input signal and digitized sine wave output signal.	64
5.10	Detector and electronics integrated test setup.	65
5.11	Electronics Board Temperatures.	66
5.12	Detector Board Temperatures.	66

5.13	Electronics Component Temperatures.	67
5.14	High Voltage Bias Supply and high voltage regulator temperature. . .	68
5.15	Correlation between high voltage bias and regulator temperature. . .	68
5.16	DC-DC Regulator Output Voltages.	69
5.17	DC-DC regulator output currents.	70
5.18	Vacuum Tests; Left: Image showing the interior of the chamber with the detector mounted on the bottom plate. Right: Image showing the exterior of the chamber, and telemetry monitoring consoles.	71
5.19	Vibration Tests; Left: vibration test of the microburst detector in the longitudinal axis. Right: vibration test of the integrated detector and electronics unit.	72
5.20	LYSO self scintillation spectrum obtained by measuring 2000 peaks .	74
5.21	LYSO self scintillation spectrum processed and binned into 16 bins by the FPGA	74
5.22	Strontium-90 spectrum obtained by measuring 2000 peaks	75
5.23	Strontium-90 spectrum processed and binned into 16 bins by the FPGA	75
5.24	Ba-133 spectrum obtained by measuring 2000 peaks	76
5.25	Ba-133 spectrum processed and binned into 16 bins by the FPGA . .	76
6.1	Design evolution of the Microburst Detector (right) and Electronics Unit (left) from breadboard prototypes (first row) to flight models (last row).	83
6.2	Maximum integral flux above a given energy from previous mission data. The figure shows comparison between the ELFIN flux between L=4.5 and 5 with the trapped (left) and precipitating flux (right) per- centiles detected by POES over the same L-shell range. The circles indicate the percentiles derived from the POES 90 degree and 0 de- gree detectors between L=4.5 and 5. The vertical red lines indicate different energy thresholds (>0.2 MeV, >0.5 MeV, >0.6 MeV and >2 MeV). Figure Credit: RADHEPT Measurement requirements docu- ment, Louis Ozeke, Department of Physics	85
6.3	Block diagram showing the conceptual design of an instrument using two crystals and adopting a bi-directional pulse approach for simul- taneous readout of both crystals using the same electronics.	87
A.1	Voltage Regulators - Digital.	96
A.2	Voltage Regulators - Analog.	97
A.3	Voltage Regulators - High Voltage.	98

A.4 Voltage Current Sensors.	98
A.5 Thermistor Monitoring.	99
A.6 RS-485 and RS-232 Transceivers.	100
A.7 NAND Flash.	101
A.8 SD Card.	101
A.9 Reset Watchdog and RTC.	102
A.10 ADC Schematic.	102

Abbreviations

ADC Analog to Digital Converter.

DAC Digital to Analog Converter.

EEP Energetic Electron Precipitation.

FGM Flux-Gate Magnetometer.

FPGA Field Programmable Gate Array.

PEPPER-X Payload for Energetic Particle Precipitation Education and Research
- eXperiment.

RADHEPT RADICALS High Energy Particle Telescope.

RADHEPT-MBD RADICALS High Energy Particle Telescope: Microburst De-
tector.

RADHEPT-LE RADICALS High Energy Particle Telescope: Low Energy.

RADHEPT-HE RADICALS High Energy Particle Telescope: High Energy.

RADICALS RAdiation Impact on Climate and Atmospheric Loss Satellite.

SCM Search Coil Magnetometer.

XRI X-Ray Imager.

Chapter 1

Introduction

1.1 Motivation

The near-Earth space environment comprises of regions of energetic charged particles known as the Van Allen radiation belts. There are predominantly two belts, the inner and outer, with the outer belt primarily consisting of electrons and inner belt primarily consisting of protons [1]. The electron population in the outer belt is highly dynamic and shows variability across a wide energy range and at multiple time scales ranging from minutes, days and years [2, 3]. Even though the radiation belts were discovered by James Van Allen over half a century ago [4], the various physical processes responsible for the variability in the radiation environment are not yet completely understood.

Understanding the various loss and acceleration processes causing the dynamics of the near-Earth space radiation environment are important for a variety of reasons. Firstly, energetic electron precipitation (EEP) from the magnetosphere into the Earth's atmosphere can also play an important role in the Earth's climate system. Understanding the impact of energetic electron precipitation on the Earth's atmosphere and climate, for example through the catalytic destruction of ozone in the middle atmosphere by NO_x and HO_x [5], remains an active area of Magnetosphere-Ionosphere-Thermosphere (MIT) coupling studies. Furthermore, these energetic charged particles, pose considerable risks to both astronauts and spacecraft avionics [6]. As

humanity prepares to return to the moon in the coming years through the Artemis program, a thorough understanding of the radiation environment becomes imperative for effective mission planning. Knowledge of the radiation environment is essential for devising appropriate shielding measures against this space radiation, ensuring the safety of astronauts and the nominal operation of spacecraft subsystems.

One particular form of energetic particle precipitation that has recently been the subject of many studies in the space physics community is electron microburst precipitation. These result from bursty and short timescale (< 1 s) scattering of energetic (few keV to MeV) electrons from the Van Allen belts into the Earth's atmosphere. Microbursts are important to study since they may represent a major loss mechanism for outer radiation belt electrons during geomagnetic storm main and recovery phases [7, 8]. Despite their very short timescales (tens of milliseconds), microbursts are thought to be a major driver of Mesosphere-Ionosphere-Thermosphere (MIT) coupling through creation of NO_x/HO_x, which in turn can cause Ozone destruction in the mesosphere and upper stratosphere, with potential impacts on climate [9].

In particular, previous studies (for example [9] and references therein) have shown that a modeled magnetic storm containing microburst precipitation for six hours increased mesospheric HO_x by 15–25% and NO_x by 1,500–2,250%. Together, these drive 7–12% upper mesospheric ozone losses, as shown in Figure 1.1 for a summer season simulation. These changes in ozone have been shown to cause Mesospheric warming, as well as an air surface temperature effect in the Antarctic regions (for example see reference [10]). Additionally, although a single magnetic storm duration lasts less than a few days, the high frequency of the magnetic storm events during geomagnetically active years has been shown to cause variability in mesospheric ozone on solar cycle timescales (for example see reference [11]). Thus, energetic particle precipitation can have a potential impact on the climate, and is currently not included in most climate models, due to a lack of comprehensive measurements [9–11].

Microbursts are often missed by traditional particle instruments, due to insuffi-

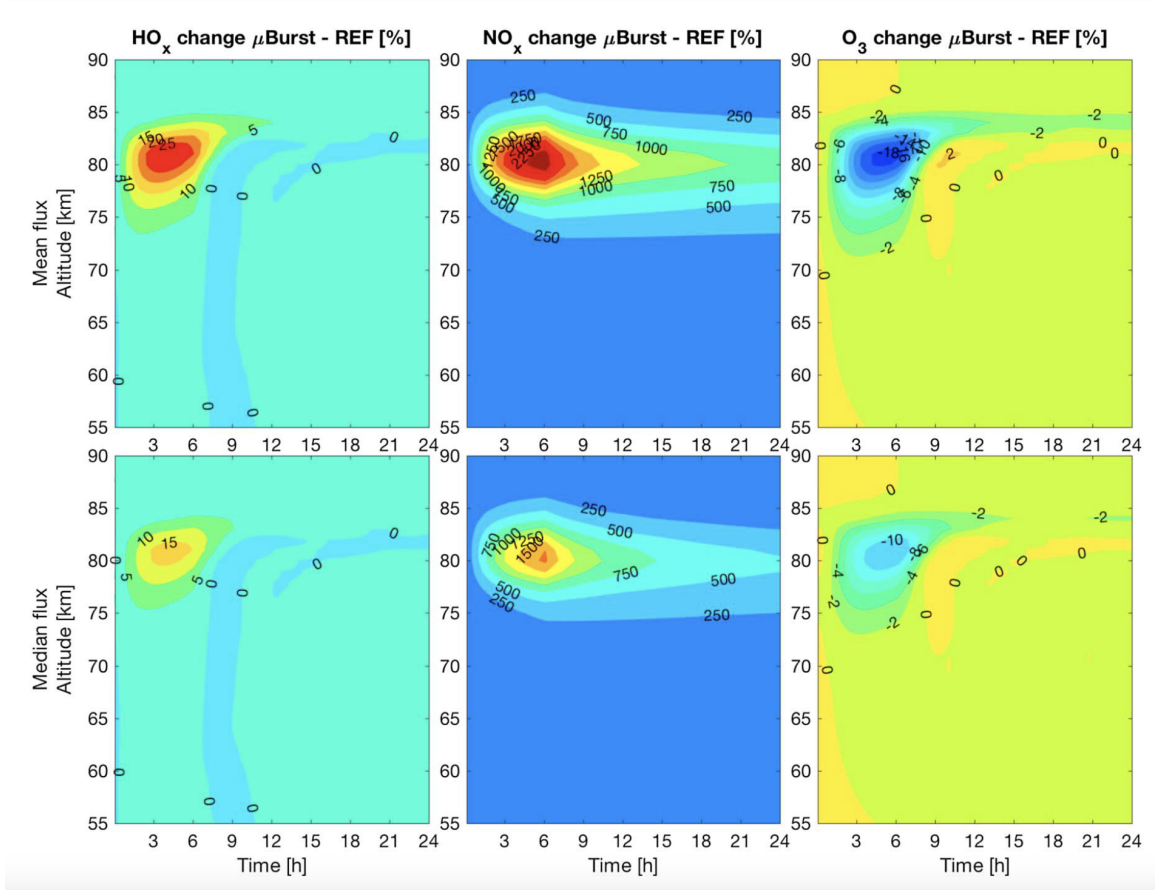


Figure 1.1: Simulated relative change in HO_x (left column), NO_x (middle column), and O_3 (right column) for the mean (top row) and median Microburst flux (bottom row), during a microburst storm that takes place in the first 6 hours. Time on the x axis is local time from the start of the simulation. Reproduced from reference [9](Seppälä, A., Douma, E., Rodger, C. J., Verronen, P. T., Clilverd, M. A., & Bortnik, J. (2018). Relativistic electron microburst events: Modeling the atmospheric impact. *Geophysical Research Letters*, 45, 1141–1147, DOI:10.1002/2017GL075949) with permission.

cient time resolution in measurements. Thus, additional extensive measurements of microbursts are required to better understand their impact on atmospheric chemistry, and role as a potentially significant radiation belt loss mechanism [12]. This thesis aims to develop new instrumentation to characterize microburst precipitation to answer some of these open questions in radiation belt physics.

Overall, the methodologies to better understand the dynamics of space radiation can be broadly grouped into three categories, (a) Theory & Simulation, (b) Instru-

mentation and (c) Observation & modelling (Figure 1.2). This thesis focuses on instrumentation; with the goal of developing a miniaturized instrument to focus on Microburst precipitation, as a part of a High Energy Particle Telescope suite designed to make in-situ measurements of energetic electrons and protons in low-Earth Orbit. This instrument is planned to fly onboard the RADIation Impacts on Climate and Atmospheric Loss Satellite (RADICALS), a micro-satellite mission which aims to study the precipitation of energetic particles from the Van Allen belts into the Earth’s atmosphere. The subsequent sections of this chapter introduce the RADICALS mission, the High Energy Particle Telescope suite and summarize the various objectives of this thesis.

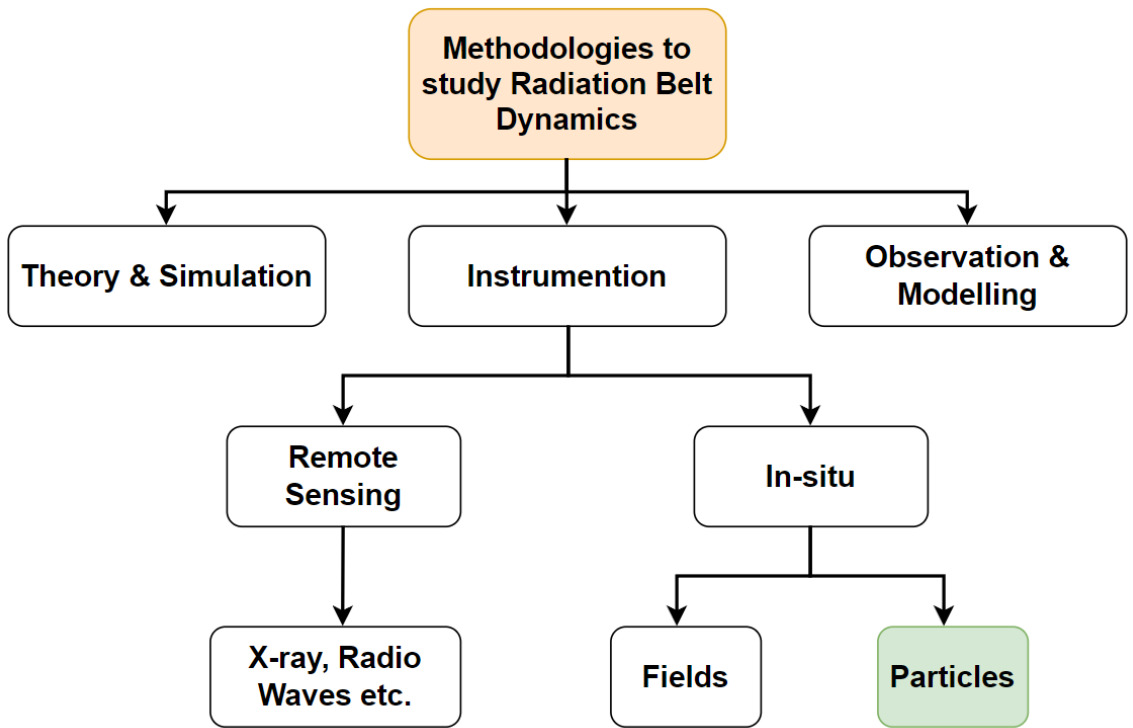


Figure 1.2: Approaches to Understand Space-Radiation Dynamics. Instrumentation development for in-situ particle measurements is highlighted in green, which is the focus of this thesis

1.2 RADICALS Mission

The RADiation Impacts on Climate and Atmospheric Loss Satellite (RADICALS) is a low-Earth orbiting micro-satellite mission investigating the transport of space radiation into the atmosphere, and its impact on Earth's climate. The RADICALS mission is planned to launch in a Low-Earth polar orbit (≈ 500 -600 km altitude) and utilizes a spin-stabilized configuration, spinning with a nominal period of 30 seconds, which enables the telescopic instruments in the payload to monitor full directionality and energy spectrum of the precipitating particles as a result of spacecraft spin. Figure 1.3 shows an artistic rendition of the RADICALS mission, with various instruments labelled. For in-situ characterization of precipitating radiation, the satellite consists of a particle instrument suite, referred to as the RADICALS High Energy Particle Telescope (RADHEPT). This suite further consists of multiple detectors, which are described in the next section. The satellite's scientific payload also includes an X-Ray Imager (XRI) to remote sense energetic particle precipitation using back-scattered Bremsstrahlung X-rays, and a boom mounted Flux-Gate Magnetometer (FGM) and Search Coil Magnetometer (SCM). These instruments on-board RADICALS and their measurements are summarized in Figure 1.3. Simultaneous measurements from RADHEPT, XRI, FGM and SCM will provide a unique set of data products, that aim to improve our understanding of the energetic particle precipitation effects and their underlying causes.

1.3 High Energy Particle Telescope

In order to make comprehensive in-situ energetic particle measurements, each RADHEPT consists of three different detector heads, the RADHEPT-HE (High Energy), RADHEPT-LE (Low Energy) and the RADHEPT-MB (Micro-Burst). Together, these detectors provide the capability to measure electrons with energies from 0.1 to 4 MeV, and protons with energies from 1 to 40 MeV. The RADHEPT-HE and

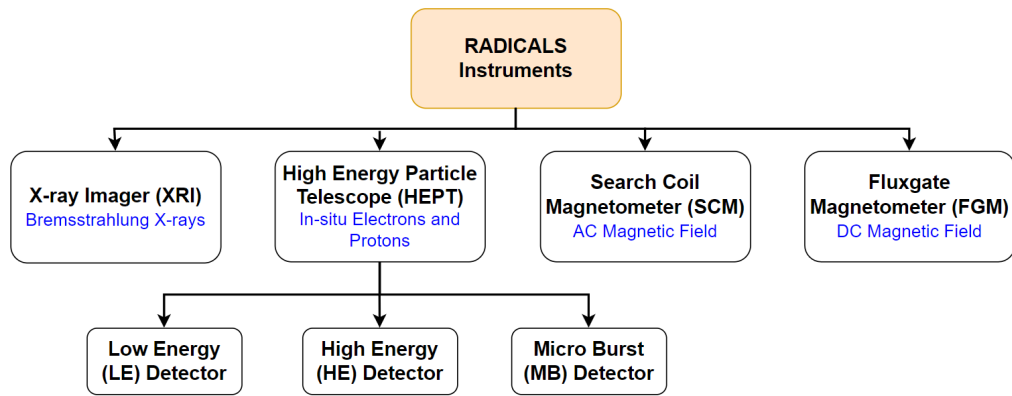


Figure 1.3: Top: Artistic rendition of the RADICALS mission with different instruments labelled, Image Credit: Andy Kale, Bottom: Overview of RADICALS instruments, text in blue indicates the physical parameter measured by each instrument.

RADHEPT-LE instruments are telescopic instruments with detectors which consist of concentric solid state detectors stacked together. Depending on the amount of energy transferred to each detector, the energy and species of the incoming charged particle can be measured. The RADHEPT-MB detector uses a Multi-Pixel Photon Counter and scintillator to detect electron microbursts at a much higher timing resolution (approx. 10 milliseconds). The instrument also consists of an electronics unit that is responsible for interfacing with the detectors and generating the science data products. This thesis focuses on developing two parts of the RADHEPT suite, namely the Microburst Detector and the instrument electronics.

1.4 Thesis Objectives

- **Objective-1: Microburst Detector design and development for the RADICALS mission** This involves defining the science measurement requirements for the detector, and designing the detector to satisfy the measurement requirements. In this thesis, this includes hardware realization, testing, calibration and performance characterization of the microburst detector.
- **Objective-2: RADHEPT electronics design and development** This includes developing an electronics system architecture, to satisfy the readout and processing of all detectors. In this thesis, this includes prototype development and testing of the electronics.
- **Objective-3: Payload development for sounding rocket flight** This comprises of developing a rendition of the Microburst Detector and RADHEPT electronics for a sounding rocket test flight. In this thesis, this includes realization and performance testing of the payload. The main motivation behind this is to increase the Technology Readiness Level (TRL) of the detector and electronics in advance of the RADICALS mission.

1.5 Thesis Outline

Chapter-2 summarizes the theory behind some aspects of energetic particle precipitation, particularly focusing on microburst precipitation. A literature review of previous microburst measuring instruments is also provided. The chapter concludes with the proposed instrument's measurement requirements most useful for the scientific community. Chapter-3 and Chapter-4 describe the design of the Microburst Detector and RADHEPT electronics respectively. Chapter-5 discusses the testing performed on the Detector and RADHEPT electronics. Chapter-6 presents the conclusions from this thesis and the future work to be completed in advance of the RADICALS mission.

Chapter 2

Electron Microburst Precipitation

This chapter gives a brief introduction to electron microbursts - characteristics, causes and effects. Microbursts are short timescale (< 1 s) bursts of precipitation resulting from scattering of energetic (few keV to MeV) electrons from the Van Allen belts into the Earth's atmosphere [12]. In order to devise a detector that returns the most scientific value in the study of microbursts, the current state-of-the-art measurements of microbursts must be well understood and areas where scientific questions remain unanswered identified. This chapter first gives a brief overview of the near-Earth radiation environment, focusing on particle motion and precipitation. Then, a literature review of previous microburst measurements through balloon missions, sounding rocket missions, and satellite missions is presented. Based on the literature survey, measurement requirements for the microburst detector are developed, which would be most useful to the scientific community.

2.1 Theory and Background

The Earth's magnetosphere forms as a result of the interaction between the interplanetary magnetic field and Earth's magnetic field. It takes on a "tear-drop" like shape, compressed on the day-side and elongated on the night-side. Within the Magnetosphere, energetic charged particles can be accelerated and confined in toroidal regions known as the Van Allen radiation belts. The inner belt exists within 1.2-3

Earth radii (R_E), while the outer belt spans from approximately 3 to 7 R_E [1]. Figure 2.1 shows an artistic representation of the near-Earth space environment, showcasing the magnetosphere and the radiation belts.

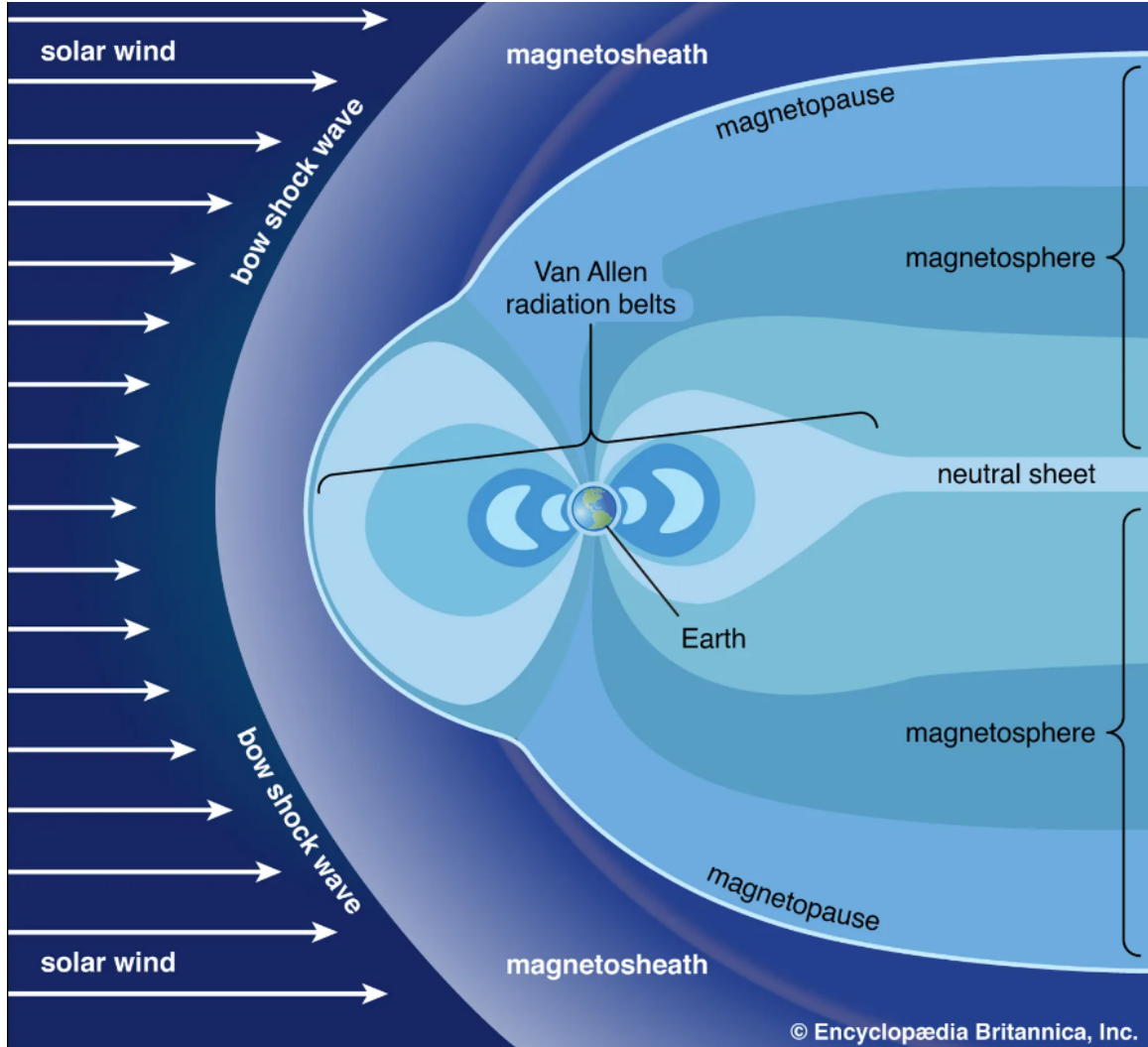


Figure 2.1: Earth's Magnetosphere and the Van Allen radiation belts, Source: Van Allen radiation belt, Encyclopedia Britannica, 25 Jan. 2024, <https://www.britannica.com/science/Van-Allen-radiation-belt>. Accessed 5 March 2024.

The inner Van Allen belt is primarily composed of protons (with energies ranging from 10 MeV to 1 GeV [13]) and electrons with energies below 900 keV [14]. On the other hand, the outer Van Allen belt mainly contains trapped relativistic electrons with energies surpassing 0.5 MeV ([15]). The population of particles especially in the

outer radiation belt undergoes dynamic changes due to various loss and acceleration processes. The subsequent sections delve into the motion of energetic charged particles in the magnetosphere and examples of some of the mechanisms responsible for particle loss.

2.2 Particle Motion

The trajectories of charged particles in the magnetosphere can be characterized by three types of periodic motion: cyclotron motion about the magnetic field lines, bounce motion along the field lines, and drift motion around the Earth. The motion of charged particles in the magnetosphere is dictated by the local electric and magnetic fields. The total force \mathbf{F} experienced by a particle due to the combination of the Coulomb and Lorentz forces is given by:

$$\mathbf{F} = q\mathbf{E} + (q\mathbf{v} \times \mathbf{B}) \quad (2.1)$$

where, \mathbf{v} denotes velocity, charge q , and the local electric field \mathbf{E} and magnetic field \mathbf{B} . The velocity of the particle can be split into two components, perpendicular (v_{\perp}) and parallel (v_{\parallel}) to the local magnetic field, as shown in figure 2.2. The angle between the velocity vector and the magnetic field is known as the pitch angle (α).

2.2.1 Gyration

From equation Equation (2.1), the perpendicular component of the velocity leads to a circular motion around a center of circular motion known as the guiding center, with a radius given as:

$$r = \frac{mv_{\perp}}{qB} \quad (2.2)$$

This is known as the gyration radius. Since, the magnetic field of the Earth is not constant, this leads to a changing gyration radius of the particle as it moves along the magnetic field lines. For radiation belt particles it can be often assumed that the

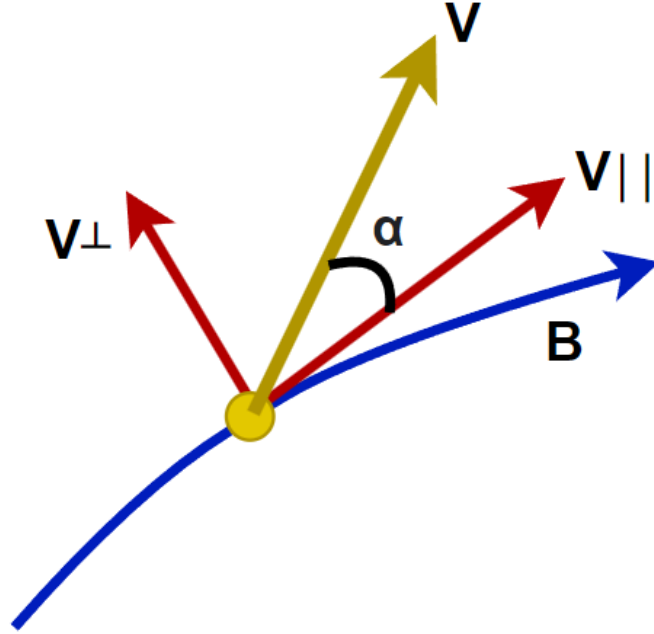


Figure 2.2: Particle Pitch Angle: The yellow arrow indicates velocity vector of the particle, the red arrows indicate the perpendicular and parallel components, and the blue line indicates the magnetic field.

magnetic field B changes slowly compared to the gyration period of the particle. This assumption implies that the particles magnetic moment is conserved, which is known as the first adiabatic invariant, μ :

$$\mu = \frac{m(v_{\perp})^2}{2B} = \frac{mv^2(\sin(\alpha))^2}{2B} = \text{constant} \quad (2.3)$$

2.2.2 Bounce Motion

As the energetic particle travels towards from the equator to the poles, the magnitude of Earth's non-uniform magnetic field increases. Thus to keep the first adiabatic invariant constant, it's pitch angle must increase. Eventually the pitch angle increases to 90 degrees, and the particle has no velocity along the field line, and “mirrors” back towards the equatorial region. The location at which the particles mirror are called the “mirror points”. This creates a “magnetic bottle” configuration which traps the charged particles, as they move along the Earth's magnetic field. The second adiabatic

invariant associated with bounce motion (J), is given as:

$$J = \oint m v_{\parallel} ds \quad (2.4)$$

where, v_{\parallel} is the parallel velocity along the field line, m is the mass of the particle, and the integral is taken over the length s of the particle's trajectory.

2.2.3 Drift Motion

The third periodic motion of radiation belt particles is longitudinal drift about around the Earth. There are three types of drift motion, (a) Gradient Drift, (b) Curvature Drift and (c) $\mathbf{E} \times \mathbf{B}$ Drift. Gradient drift occurs due to a gradient in the magnetic field. The speed of the guiding center due to the gradient drift is given as

$$\mathbf{v}_G = \frac{m v_{\perp}^2}{2qB^3} (\mathbf{B} \times \nabla B) \quad (2.5)$$

Here, \mathbf{B} is the magnetic field, ∇B is the gradient of the magnetic field, m and q denote the mass and charge of the particle respectively. Since the gradient drift depends on the charge of the particle, it makes electrons and protons (or ions) drift around the Earth in opposite directions as schematically shown in figure 2.3. These particles create an electrical current, which is known as the ring current. The second type of drift occurs due to the curvature of the magnetic field and is known as curvature drift, the velocity due to curvature drift is:

$$\mathbf{v}_C = \frac{m v_{\parallel}^2}{q R^2 B^2} (\mathbf{R} \times \mathbf{B}) \quad (2.6)$$

Here, \mathbf{R} is the radius of curvature of the particle trajectory. The third type of drift is due to the Electric field (\mathbf{E}) in the magnetosphere. The velocity due to this drift is independent of charge of the particle and is given by:

$$\mathbf{v}_E = \frac{\mathbf{E} \times \mathbf{B}}{B^2} \quad (2.7)$$

Figure 2.3 shows example trajectories of particles in the radiation belts, which is a combination of these three types of periodic motion. The particles bounce between

the mirror points, and during this motion their gyration radius changes. The gyration radius is larger in the equatorial region and smaller at the poles. Additionally particles also move across the Earth's longitudes due to the various drift effects. A more detailed explanation of the motion of trapped particles can be found in [15]. Trapped particles in the radiation belts can be lost or taken out of this region due to variety of phenomena, especially wave-particle interactions, with a variety of plasma waves, some of which are discussed in the next section.

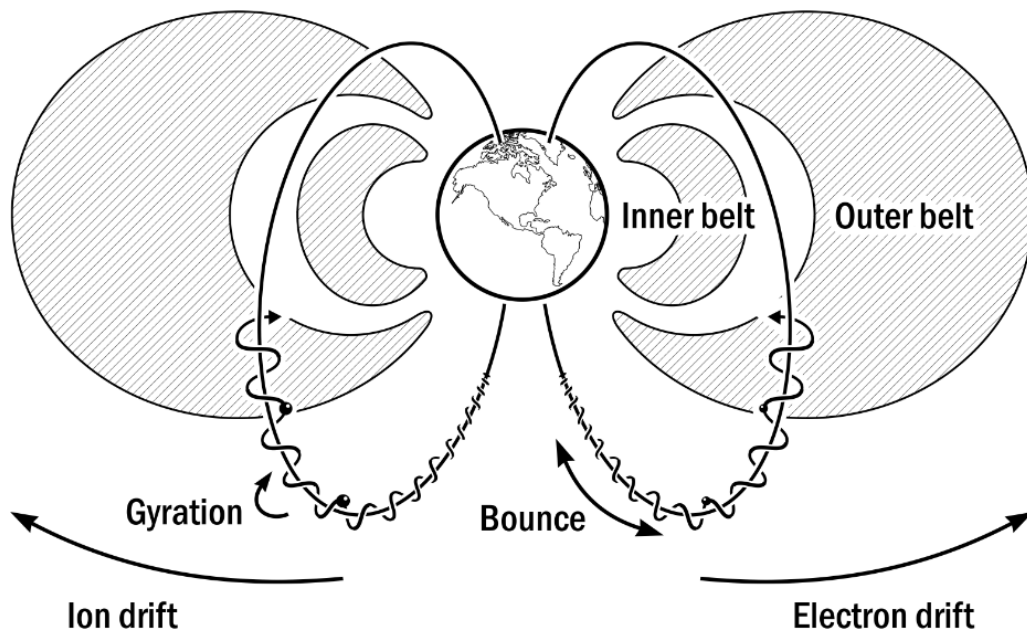


Figure 2.3: Motion of charged particles due to the Earth's magnetic field. The figure depicts the three types of particle motion, gyration, bounce, and drift. Figure Credit: Andy Kale.

2.3 Energetic Particle Precipitation

Particles in the magnetosphere are lost (taken out of the magnetosphere) mainly through two processes (a) precipitation into the Earth's atmosphere, and (b) magnetopause shadowing. Particle precipitation occurs when energetic particles reach a low enough altitude to interact with the earth's atmosphere and are subsequently lost [5].

Magnetopause shadowing, on the other hand, is the process by which particles are lost through the outer boundary of magnetosphere where their drift trajectories reach a compressed magnetopause. These losses can also be enhanced by outward radial diffusion of electrons to the magnetopause[16]. The relative importance of these two mechanisms as well as their driving mechanism are still under debate. The focus of this thesis is particle precipitation into the atmosphere, which occurs when the magnetic mirror point falls below a certain altitude limit (often considered to be 100 km) such that the particle is lost to the atmosphere.

The altitude of the mirror point of the bounce motion depends on the local pitch angle of an energetic particle. When the pitch angle of the particle enters within a certain limit (called the local loss cone), the altitude of the mirror point becomes low enough so that the particle is lost in the atmosphere. Based on the temporal duration, precipitation can be divided into two categories: band precipitation, and microburst precipitation. Precipitation bands are longer in duration and exhibit a gradual increase in observed particle flux, as compared to microbursts which are shorter in duration, as shown in Figure 2.4. This thesis focuses on microburst precipitation, which is described in more detail in the next subsection.

2.3.1 Microburst Precipitation

Microburst precipitation is bursty and short timescale (< 1 s) precipitation resulting from the scattering of energetic (having energies in the range from few keV to MeV) electrons from the Van Allen belts into the Earth's atmosphere. As shown in Fig. 2.4, they can often exhibit a order of magnitude increase in flux as compared to the background rates of precipitation. Previous studies have shown that microbursts may represent a major loss mechanism from the outer radiation belt electrons during geomagnetic storm main and recovery phases [7, 8]. Despite their very short timescales (tens of milliseconds), microbursts are thought to be a major driver of Mesosphere-Ionosphere-Thermosphere (MIT) coupling through creation of NO_x/HO_x, which in

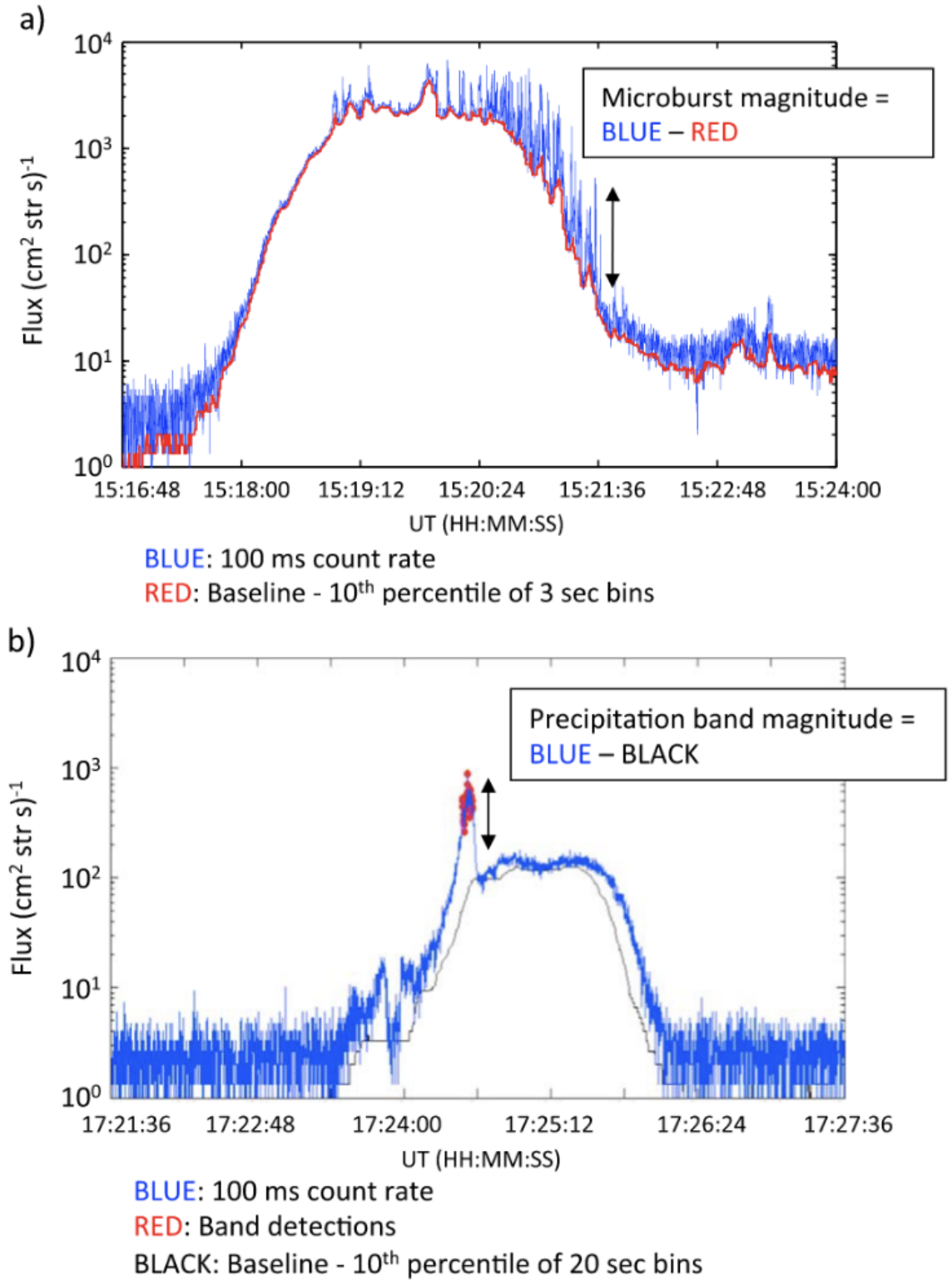


Figure 2.4: (a) Microburst precipitation and (b) band precipitation as observed by the Solar, Anomalous, and Magnetospheric Particle Explorer (SAMPEX) satellite taken from reference [17].

turn can cause Ozone destruction [9]. The dominant cause of microbursts are considered to be due to wave-particle interactions with different plasma waves which cause pitch angle scattering of electrons into the local loss cone. This happens when the energetic particles interact strongly with plasma waves, and this can occur when the following condition for wave-particle Doppler shifted gyro-resonance is satisfied:

$$\omega - k_{\parallel}v_{\parallel} = n|\Omega|/\gamma \quad (2.8)$$

Here, ω denotes the wave frequency, $|\Omega|$ denotes the gyro-frequency, γ is the relativistic correction factor, n is the harmonic number ($n = 0, 1, 2, \dots$), k_{\parallel} and v_{\parallel} are the wave vector and electron velocity component along the ambient magnetic field \mathbf{B} . The condition indicates that resonance occurs when the Doppler shifted wave frequency (left hand side) is same as a multiple of the relativistic gyrofrequency of the particle (right hand side) [18]. The relativistic correction factor is calculated as, $\gamma = 1/\sqrt{1 - v^2/c^2}$, where v is the speed of the electron and c is the vacuum speed of light. The value of the relativistic correction factor, ranges from approximately 0.58 (for a 300 keV electron) to 5.8 (for a 3 MeV electron).

Various studies have shown that Microbursts are caused due to interactions with whistler mode chorus waves (For e.g., reference [12, 19, 20]). Additionally, relativistic energy microbursts have also been hypothesised to occur due to interactions with electromagnetic ion cyclotron (EMIC) waves (For e.g., reference [21]). However, the exact driving mechanism and energy of precipitating electrons that result from the interaction with different types of plasma waves are still under debate. This motivates the need for further and more extensive measurements. Summarized in the next section are the various previous electron microburst measurements and detection methodologies.

2.4 Previous Electron Microburst Measurements

Figure 2.5 shows a pictorial representation of the different methods of measuring microburst precipitation (or energetic particle precipitation in general). This section describes each of these methods, with examples from previous missions.

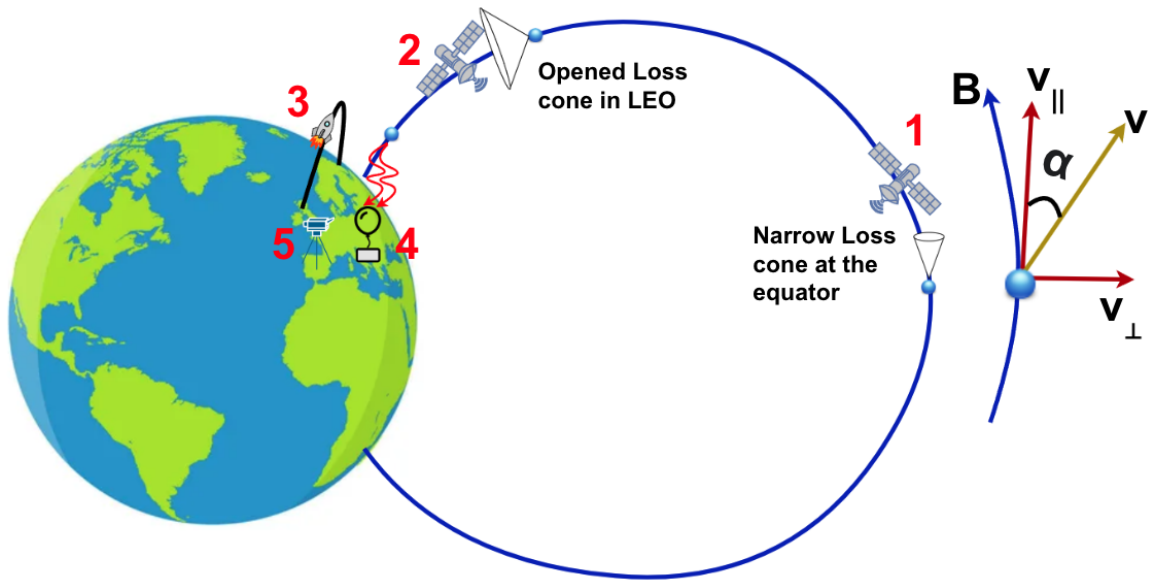


Figure 2.5: Different ways to measure particle precipitation: (1) In-situ electron measurements in the radiation belts, (2) In-situ measurements in low Earth orbit, (3) In-situ measurements using sounding rockets, (4) Remote-sensing using balloon-based measurements of Bremsstrahlung X-rays, (5) Remote-sensing using ground-based instruments (e.g., all-sky imagers, riometers etc).

1. **In-situ electron measurements in the radiation belts:** Missions such as the Van Allen Probes have measured in-situ electron flux in the radiation belts, e.g., reference [22]. Although such data is useful for analysing the source region of precipitating particles, it is difficult to resolve precipitating particles at this altitude since the loss cone is very narrow. However, such spacecraft are useful for making plasma wave measurements that are hypothesised to be the drivers of particle precipitation in the equatorial region.
2. **In-situ electron measurements in low Earth orbit:** As the energetic electrons travel along the magnetic field lines from the equator towards the poles,

the local loss cone angle increases as shown in figure 2.5. Thus, low Earth orbiting satellites in the polar region provide an ideal location for making pitch angle resolved energetic particle precipitation measurements. Multiple low Earth orbit missions ranging from cubesats (for example FIREBIRD-II [23], AeroCube-6 [24], ELFIN [25]) as well as small satellites (for example SAMPEX [26]) have measured microburst precipitation.

3. **In-situ measurements using sounding rockets:** Sounding rockets can be used to measure precipitating particles as they enter the atmosphere. Missions like the Loss through Auroral Microburst Pulsations (LAMP) sounding rocket have been launched to measure both low energy energy electrons (10s keV) as well as high energy relativistic electrons (MeV). The disadvantage of using sounding rockets is that such missions typically have a very short duration (approx. 15-30 mins) and also need to be launched during a geomagnetically active time.
4. **Remote-sensing using balloon-based measurements of Bremsstrahlung X-rays:** The first electron microbursts were detected by balloon-borne instrumentation in the 1960's [27]. Balloon-borne instruments can measure Bremsstrahlung X-rays produced by precipitating electrons when they enter Earth's atmosphere. The X-ray spectrum can then be inverted to estimate the energy spectrum of the incoming electrons. Missions such as BARREL have made multiple measurements of precipitating microbursts by remote-sensing Bremsstrahlung X-rays [28]. However, since these are indirect measurements, they possess inherent uncertainties as compared to direct in-situ measurements, due to the inversion process involved.
5. **Ground-based measurements (e.g., all-sky imagers, riometers etc.):** These are also indirect methods which can detect the effects of particle precipitation. All sky imagers such as THEMIS-ASI have been used to image aurora,

which are caused by precipitating particles [29]. Recent studies have also shown a correlation between pulsating auroras and microburst precipitation [12]. Riometers are used to measure the absorption of radio signals which pass through the ionosphere, which changes as a result of ionization from the precipitating energetic particles. However, since these measurements are indirect, they reveal limited information about the energy spectrum of the precipitating electrons.

2.5 Microburst Instrumentation Motivation

Even though multiple previous missions have measured microburst precipitation in the past, due to limitations in instrumentation pertaining to energy range, temporal resolution, and directionality, these measurements to date have not been able to definitely answer questions pertaining to microbursts. Listed below are some of the open science questions pertaining to microburst precipitation (See [12] and references therein, for a detailed summary of the current understanding and open questions pertaining to microburst precipitation):

- **Science Question 1:** What is the energy spectrum of electron microbursts?
- **Science Question 2:** Do low-energy (100s keV) and relativistic (MeVs) microbursts occur simultaneously?
- **Measurements Required:** *Differential electron flux measurements of microbursts in both the sub-relativistic (100s keV) and relativistic energy ranges (MeVs)*
- **Science Question 3:** What is the contribution of microburst precipitation to the overall precipitation budget? Additionally, what is the temporal variation of microburst flux?
- **Measurements Required:** *Long term systematic measurements of microbursts, with a broad energy range and high max. flux measurable limit*

- **Science Question 4:** What are the driving mechanisms for microbursts of different energies (sub-relativistic and relativistic)?
- **Measurements Required:** *Simultaneous measurements of microbursts and plasma waves (Chorus, EMIC etc.)*
- **Science Question 5:** What is the spatial extent of microbursts? i.e. are they localised over a small region or spread over a larger region.
- **Measurements Required:** *Simultaneous measurements of microbursts precipitation and backscattered Bremsstrahlung X-rays can reveal spatial extent*

Based on the science questions pertaining to microbursts described in the previous section, it is clear that a detector designed to measure high energy microbursts must have a broad energy range spanning from at least 100s keV to a few MeV. Additionally, the detector must have a fast response time (on the order of Milliseconds) to resolve the microbursts. The detector must also be able to measure a large maximum flux as the microburst flux is known to increase an order of magnitude above the baseline (Appendix A provides a overview of microburst flux measured through previous missions). Additionally, due to the power, mass, and volume constraints of a micro-satellite mission, the detector must be compact and have low power consumption. Table 2.1 summarizes the measurement parameters by previous missions, and proposes measurement goals for the RADICALS mission.

2.6 Summary and Discussion

In this section a brief overview of the theory governing single charged particle motion in the magnetosphere was given. This consists of three periodic motions: Gyration, Bounce and Drift. Then some particle loss mechanisms from the magnetosphere were explained including band precipitation and microburst precipitation. A literature review of previous microburst measurements was provided, highlighting the gap in

Table 2.1: Previous microburst measurement parameters and proposed goals for the RADICALS micoburst detector.

Parameter	Previous Measurement Made		Proposed Goal
Mission	FIREBIRDII [23]	SAMPEX-HILT [26]	RADICALS
Energy Range	0.2 to 1 MeV, > 1 MeV	> 1 MeV	0.2 to 3 MeV
Energy Res.	5 channels	N/A	> 8 channels
Time Res.	18.75 ms	20 ms	10 ms
Field of View	180 (and 45) deg	60 deg	180 deg

current measurements and the need for further extensive measurements. Lastly, based on this literature review, measurement requirements for the microburst detector were defined. The next chapter describes the design process to develop a detector that can satisfy these requirements.

Chapter 3

Microburst Detector Design

3.1 Microburst Detector Measurement Requirements

Based on the literature survey of previous measurements described in the previous chapter, the following measurement requirements were defined for the Microburst detector.

- Time resolution: 10 ms
- Energy Range: 200 keV to 3 MeV
- Energy Resolution: 50% $\Delta E/E$
- Maximum Flux: 10^5 counts/cm²/str/sec
- Field of View: $2\pi sr$ (Hemispherical)

3.2 Detector Conceptual Overview

The proposed detector is a multi-pixel photon counter (MPPC) or silicon photomultiplier (SiPM) based scintillator detector. Such detectors have been previously used in CubeSat missions for Gamma-ray spectroscopy (for example: [30, 31]), since they have very low power consumption, high gain, and fast responsivity. In this thesis, we aim to extend this detection methodology to the in-situ measurement of energetic

electrons in space. Figure 3.1 shows a conceptual schematic of the detector. The detector consists of two main elements: a scintillator crystal and the MPPC.

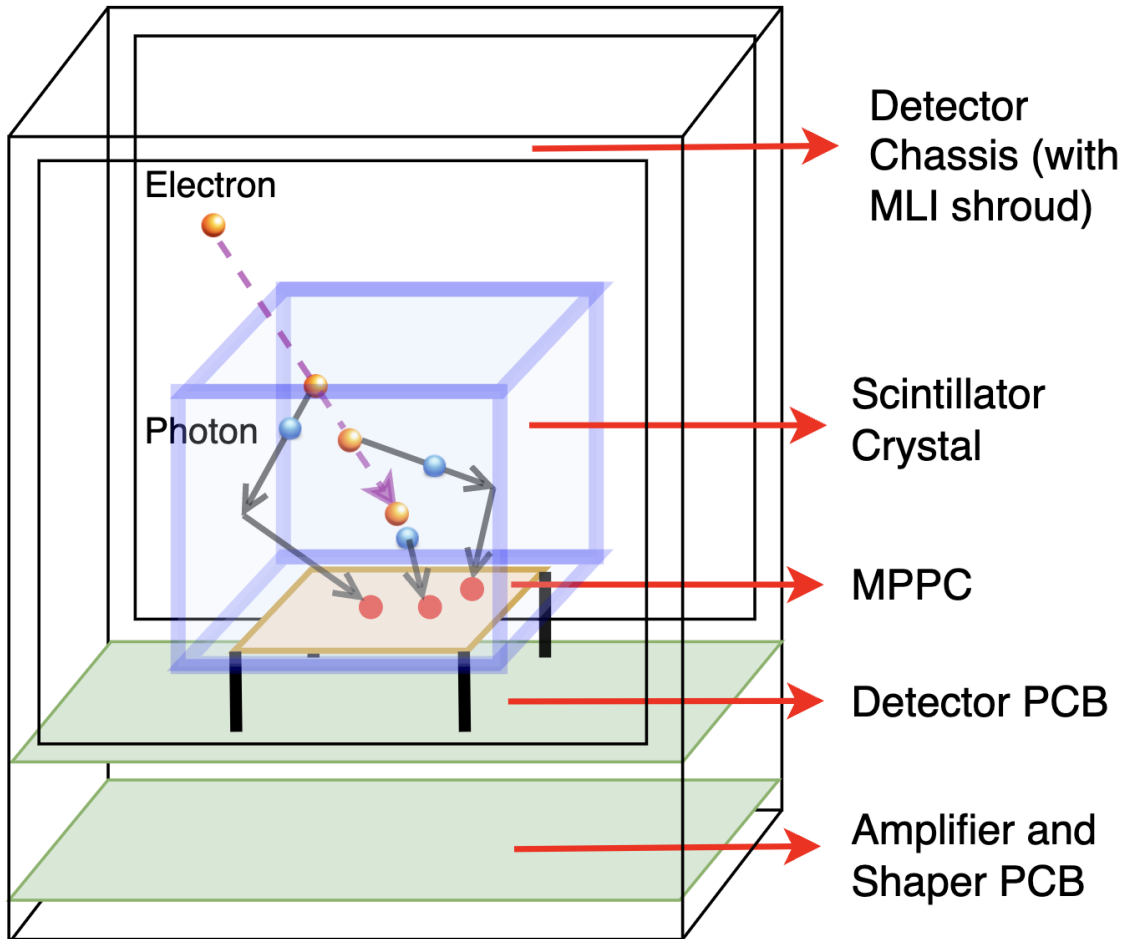


Figure 3.1: Microburst Detector Concept: The diagram shows a schematic of the detector, that consists of scintillator crystal mounted on a multi-pixel photon counter, an incoming electron generates multiple photons in the scintillator, that are then counted by the MPPC. The scintillator crystal is coated with Aluminium to reflect photons into the MPPC detector.

An incoming electron interacts with the scintillator crystal and generates photons. The number of photons generated is proportional to the energy of the incoming electron. These photons are then detected by the multi-pixel photon counter, that generates an output pulse with total charge proportional to the number of photons (i.e., the energy of the electron). Thus, by measuring the pulse charge, the energy of the incoming electron can be determined. The output pulse is amplified in a

preamplifier-shaper circuit giving an output voltage proportional to the pulse charge.

The crystal is coated with Aluminium to reflect photons towards the MPPC detector. Additionally the crystal is also coated with Parylene, which is a polymer that protects the crystal from moisture and corrosion. Lastly, the entire Aluminium and Parylene coated crystal is covered in an Aluminium and Mylar shroud, which acts as an additional light tight cover. A cubic crystal was chosen to obtain an approximately isotropic geometric factor from all directions. Initially, a spherical (and also a hemispherical) crystal was considered to ensure a isotropic geometric factor, but a cube was preferred due to practical factors such as ease of assembly, lower price, and lead time. The subsequent subsections of this chapter describe the various detector design elements and trade-offs. The electronics design is described in the next chapter.

3.3 Detector Design Elements

3.3.1 Silicon Photomultiplier

The silicon-photomultiplier (SiPM) or multi-pixel photon counter (MPPC), is a photon counting device with that consists of Geiger mode avalanche photodiode (APD) pixels. These devices are compact and have a low operating voltage ($\approx 50\text{V}$) as compared to traditional photo-multiplier tubes (PMTs). They have high gain on the order of 10^5 to 10^6 compared to other solid state detectors which have unity gain. The various parameters of the MPPC are described below:

1. **Photosensitive Area:** The effective area of the MPPC is the total area where an incoming photon will be detected. For the Hamamatsu MPPCs used here (part number S13360-6075CS [32]), this ranges from 0.0169 cm^2 (1.3 mm X 1.3 mm) to 0.36 cm^2 (6 mm X 6 mm).
2. **Pixel Pitch:** This is the vertical and horizontal distance between adjacent pixels, a finer pixel pitch implies that a larger number of pixels can be fit in to the same area. A finer pitch thus allows for counting many more photons in

one pulse. Once triggered a single pixel requires several hundred nanoseconds to recover (dead time) before it can respond to another photon.

3. **Spectral Response Range:** This is the range of wavelengths of light that the MPPC is sensitive to. For the Hamamatsu MPPC (part number S13360-6075CS [32]), two ranges are available: 320 to 900 nm and 270 to 900 nm. The wavelength at which the MPPC is most sensitive is known as the peak sensitivity wavelength.
4. **Photon Detection Efficiency:** This is the number of photons detected divided by the number of incident photons. It is computed by taking the product of fill factor, quantum efficiency and avalanche probability.
5. **Gain:** The gain is defined as the ratio of charge produced when one pixel hits one electron divided by the charge of the electron ($M = Q/(1.6 * 10^{-19})$). The charge Q depends on the reverse voltage applied to the MPPC.

Figure 3.2 shows typical characteristics of the MPPCs from Hamamatsu used in this study. The left panel shows the photon detection efficiency as a function of wavelength. The right panel shows gain, crosstalk probability, and photon detection efficiency as a function of over-voltage applied to the MPPC, which is defined as the reverse bias voltage applied minus the avalanche breakdown voltage.

3.3.2 Scintillator

The scintillator crystal generates photons when struck by an incoming electron. The number of photons is proportional to the energy of the incoming electron. The various characteristics of scintillators are described below.

1. **Light Output:** Light output (LO) is the coefficient of conversion of ionizing radiation into light energy. NaI(Tl) crystal has the one of the highest light output, and thus LO of NaI(Tl) is taken to be 100%. Light output of other

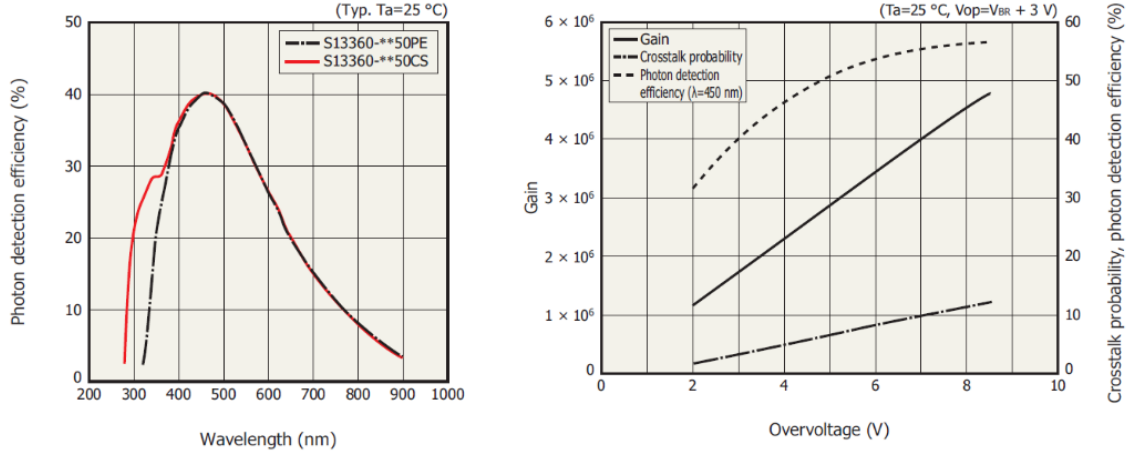


Figure 3.2: MPPC Characteristics (taken from reference [32])

scintillators is determined relative to that of NaI(Tl)(%). Alternatively, LO (Photon/MeV) can also be defined as the number of visible photons produced in the bulk of the scintillator per MeV of deposited energy.

2. **Decay Time:** The time required for scintillation emission to decrease to $(1/e)$ of its maximum.
3. **Emission Spectrum:** Is the relative number of photons emitted by the scintillator as a function of wavelength. For efficient detection of photons, the maximum emission wavelength of the scintillator should be close to the peak sensitivity wavelength of the MPPC.

Table 3.1 shows a comparison of different properties of 6 crystals: NaI(Tl), CsI(Tl), CsI(Na), LaBr, BGO, and LYSO.

3.3.3 Reflector & Optical Glue

In the proposed design the scintillator material is coated with Aluminium, to reflect back the outward emitted photons towards the MPPC. The crystal is also coated with a layer of Parylene to provide protection against moisture, corrosion and micro-meteorites.

Table 3.1: Comparison of Scintillator Material Properties [33, 34].

Material	NaI(Tl)	CsI(Tl)	CsI(Na)	BGO	LYSO	LaBr
Density [g/cm^3]	3.67	4.51	4.51	7.13	7.1	5.29
Emmision Max. [nm]	415	560	420	480	420	358
Decay Constant [μs]	0.23	1	0.63	0.3	0.03	0.035
Refractive Index	1.85	1.79	1.84	2.15	1.81	1.9
Light Yield (Ph./MeV)	43000	51800	38500	8200	33200	61000
Hygroscopic	Yes	Slightly	Slightly	No	No	Very

3.3.4 Mechanical & Thermal Design

A chassis is also designed to hold the detector (scintillator and MPPC) as well as the pre-amplifier printed circuit board. The chassis has the provision to wrap the detector using a protective shroud (made of Aluminized Mylar) for thermal stability as well as to protect the scintillator from small orbital debris.

3.4 Detector Design and Trade-Offs

In order to design a detector which satisfies the scientific measurement requirements, a number of design parameters need to be optimized. The main performance metrics of the detector are measurable energy range (low energy and high energy limits), measurable maximum flux, and signal to noise ration. To maximize these metrics, The main parameters to be selected for the detector are MPPC type, dimensions of crystal, material of the crystal, type of optical glue and reflector. This section describes the different design trade-offs that are considered while designing the detector.

3.4.1 Geometric Factor and Field of View

The geometric factor (G) of a particle detector can be defined as factor of proportionality relating the number of particles the detector count rate (C) to the number of particles incident on the detector (the incoming flux, J in units of particles per cm^2

per steradian),

$$C = GJ \tag{3.1}$$

Due to the the scintillator crystal being a cube, the geometric factor of the detector varies with the angle of incidence of the incoming electrons. The geometric factor at a particular angle of incidence can be calculated based on A_{eff} , which is the 2D projected area of the cube when looking at it from a particular angle. Figure 3.3 shows a 3D plot of the effective geometric factor for different angles of incidence. From this plot the average geometric factor of the detector can be computed, which is $2.26 \text{ cm}^2 \text{ str}$ for a 0.5 cm size cubic scintillator crystal.

3.4.2 Geometric Factor versus Maximum Measurable Flux

As shown in equation 3.1, the signal in the detector is related to the incoming flux, with the geometric factor as the proportionality constant. Additionally, the maximum count rate depends on the capability of the signal processing electronics system. Figure 3.4 shows this relation of the maximum measurable flux with the size of the crystal, for four different maximum count rate capabilities of the electronics (which are $100,000 \text{ cts/sec}$ (blue), $200,000 \text{ cts/sec}$ (red), $500,000 \text{ cts/sec}$ (yellow) and $1,000,000 \text{ cts/sec}$ (green)). The detector geometric factor for different sized crystal is also plotted on the right hand scale. Based on microburst flux levels observed from previous missions, the maximum integral flux above the minimum energy threshold (200 keV) of the detector is observed to be of the order of $10^5 \text{ counts/cm}^2/\text{str}/\text{sec}$ [26]. Thus, from the plot a possible solution for this is a 0.5 cm sided cubic crystal with maximum of $200,000 \text{ counts/sec}$ (denoted by the intersection of red plot and black dotted line). This is calculated by dividing the maximum count rate ($200,000 \text{ counts/sec}$) by the geometric factor of a 0.5 cm size cubic scintillator crystal ($2.26 \text{ cm}^2 \text{ str}$), which leads to a maximum flux of $0.88 \cdot 10^5 \text{ counts/cm}^2/\text{str}/\text{sec}$.

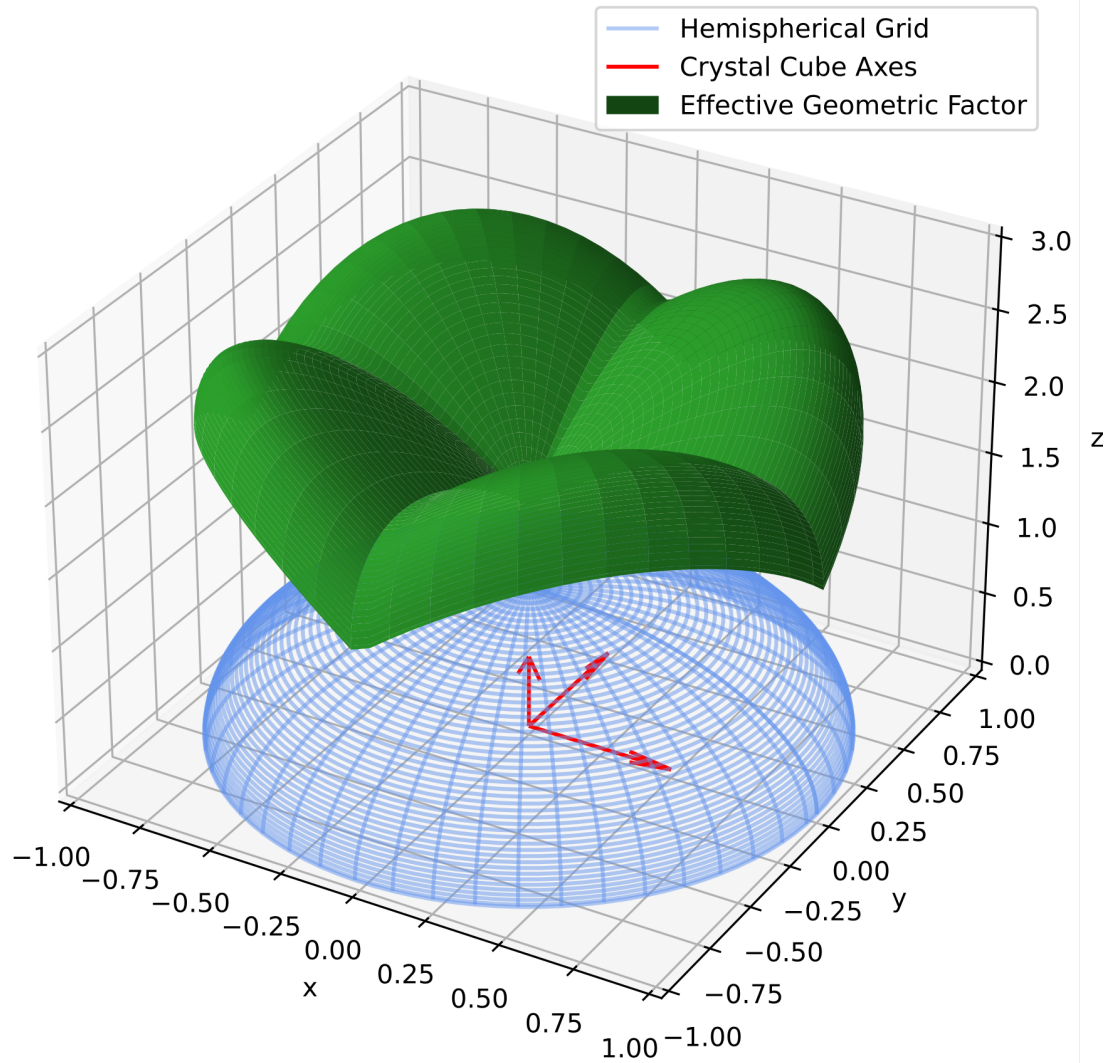


Figure 3.3: Approximate geometric factor (cm^2str) of a 0.5 cm cubic crystal for different angles of incidence of electrons.

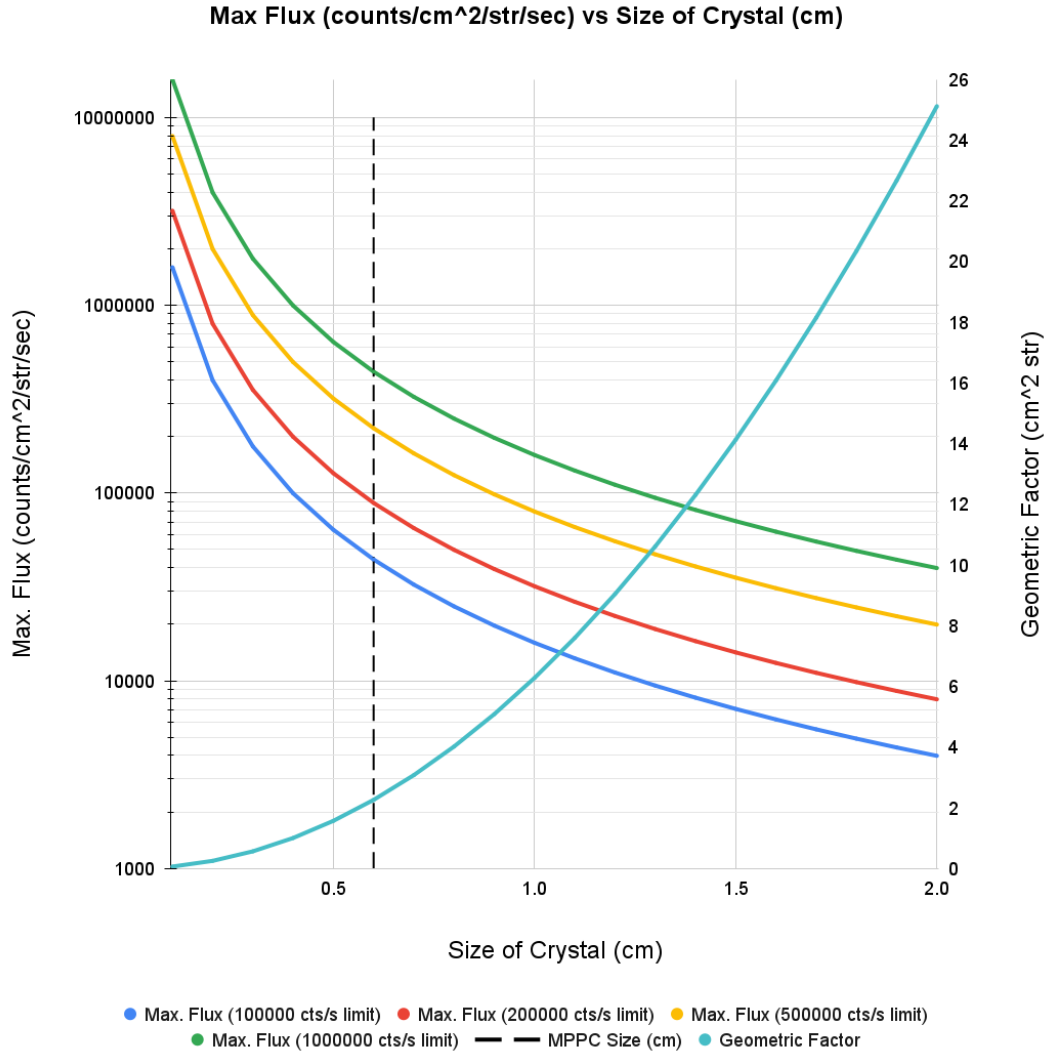


Figure 3.4: Maximum measurable flux versus size of crystal (cm) for different maximum count rate capabilities of the signal processing electronics.

3.4.3 Geometric Factor versus Maximum Energy Range

The maximum measurable energy of an incoming electron depends on the the electron stopping within the length of the crystal, thus depending on the scintillator material properties and the size of the scintillator crystal. The following equation gives the relation between the mean distance travelled by an electron in a material (denoted by Δx or the continuous slowing down approximation (CSDA) range), the initial kinetic

energy of the electron E_0 , and the linear stopping power of a material $S(E)$,

$$\Delta x = \int_0^{E_0} \frac{1}{S(E)} dE \quad (3.2)$$

Fig 3.5 shows the variation of maximum measurable energy with respect to the size of the crystal, for a CsI crystal. This has been computed using National Institute of Standards and Technology (NIST) ESTAR program[35], that contains stopping power of different materials, which can be used to calculate the CSDA range. The plot shows that a 5 mm sized crystal can measure maximum electron energy of approximately 3.5 MeV.

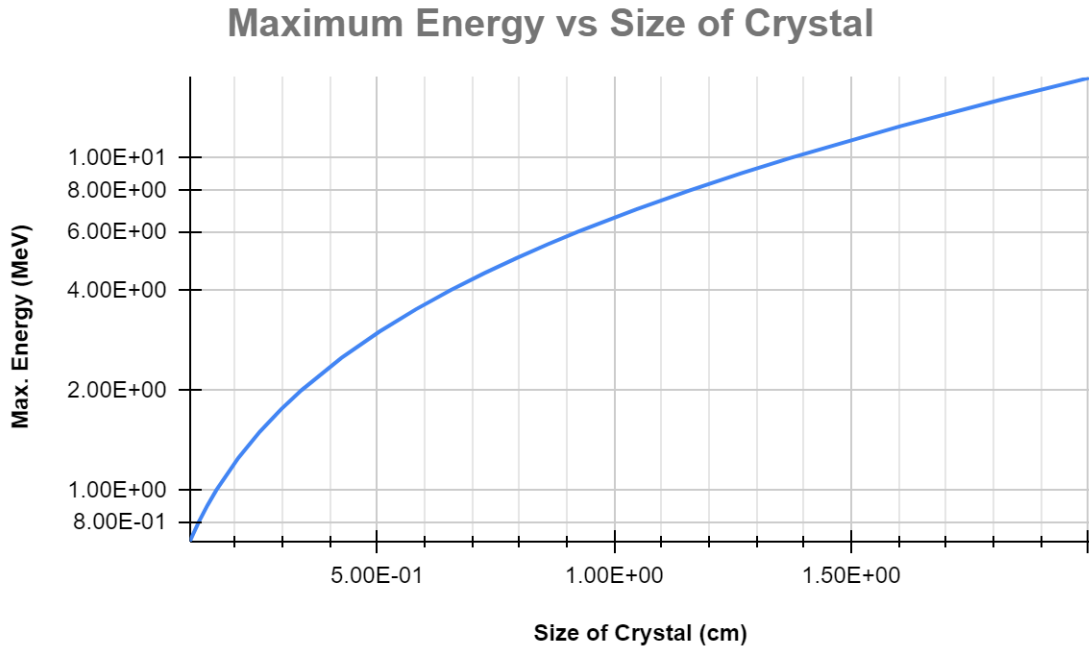


Figure 3.5: Maximum Energy measurable with respect to the size of the crystal.

Based on the analysis described to determine the maximum measurable flux and maximum measurable energy, it can be seen that a 5 mm sized crystal satisfies the scientific measurement requirements for the both the energy range and incoming flux. The higher energy limit for scintillator materials such as Cesium Iodide (Sodium

Doped) (CsI(Na)), Bismuth germanate (BGO), and Lutetium–yttrium oxyorthosilicate (LYSO), is approximately 3.5 MeV. The lower energy threshold depends on the noise of the detector and electronics system which can be determined after testing and discussed in Chapter 5. Additionally, the geometric factor of these crystals allows to measure a maximum integral flux of 10^5 counts/cm²/str/sec using a FPGA that can handle a maximum of 200,000 counts/second. A higher maximum flux can be obtained by increasing the maximum count rate capability of the FPGA or by reducing the geometric factor of the detector. Based on this analysis and trade-offs described in this section, a 5 mm CsI(Na) and a 5mm LYSO crystal was chosen for the sounding rocket test flight detector.

Amongst the scintillator crystal options described in Table 3.1, LaBr and NaI(Tl) were ruled out because of their hygroscopic properties. The LaBr crystal was observed to expand and become unusable when exposed to ambient humidity. For the rocket flight, the LYSO crystal was chosen to act as a validity check of the instrument performance by measuring its self-scintillation pulses. In order to detect incoming electrons, the CsI(Na) detector was chosen instead of the BGO, due to higher light yield of the the CsI(Na) as compared to the BGO. This would result in a stronger signal being produced from lower energy electrons, that are expected to be observed during the sounding rocket flight (For example, figure 7.2 of reference [5] shows that altitude of peak electron energy deposition as a function of the electron energy).

3.4.4 Microburst Detector Design and Realization for Sounding Rocket Test flight

Figure 3.6 shows a exploded view of the CAD model of the detector developed for the PEPPER-X sounding rocket mission. The detector consists of two detector boards, one with a CsI(Na) crystal and the other with the LYSO crystal. The CsI(Na) crystal is on the top, so as to detect incoming electrons during the sounding rocket flight. The LYSO crystal is in between the stack that generates self-scintillating crystal

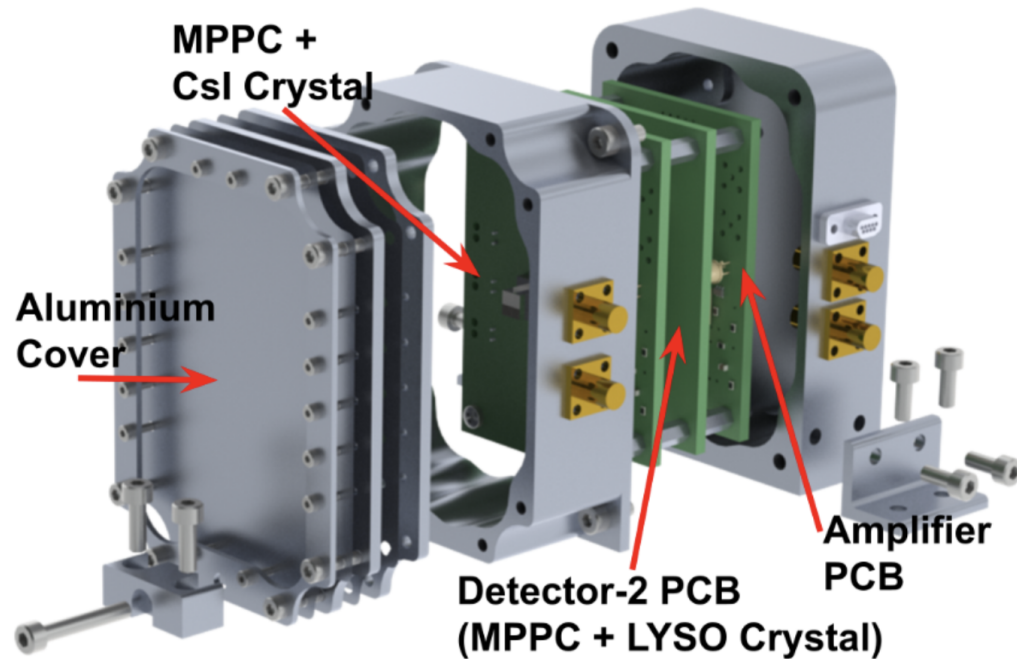


Figure 3.6: Exploded view of the detector design for the PEPPER-X sounding rocket mission. CAD Model Credit: Carl Berresheim, Dept. of Mechanical Engineering, University of Alberta

(LYSO) ‘artificial’ signals to validate instrument performance in case no Microburst event occurs during flight. A protective cover made from one layer of Aluminium foil and one layer of Mylar is also added to the top the detector to make the detector light tight and also protect the crystals from dust and moisture. Figure 3.7 shows a few pictures of the Microburst detector developed for the sounding rocket test flight. Figure 3.7(a) shows one of the crystals that has been coated with aluminium to reflect the scintillation photons inwards. Image (b) shows the two crystals (LYSO and CsI(Na)) during assembly. Image (c) shows the flight model of the detector, that has been covered with the protective aluminium cover. The flight model of the detector head developed for the sounding rocket test flight has a mass of 617 g, and a volume less than 1U (10 cm x 10 cm x 10 cm).

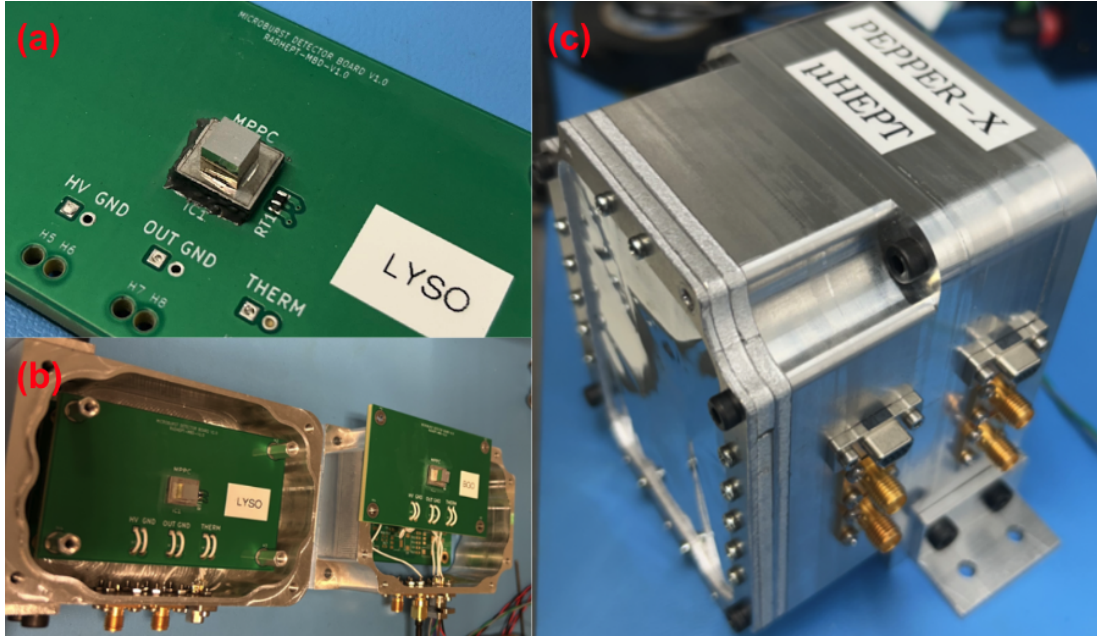


Figure 3.7: (a) Zoomed-in picture of the LYSO crystal and MPPC in the prototype (after aluminium and parylene protective coating is added), the crystal and MPPC are to the left of the pasted LYSO text label; (b) The detector prototype during assembly with two scintillator crystals (CsI(Na) and LYSO); (c) The flight model of the detector with the aluminium protective cover added

3.5 Summary and Discussion

This chapter described the detector design with emphasis on the various detector elements and design trade-offs. Details of the design and realization of the detector developed for the sounding rocket test flight were discussed. The next chapter describes the read-out electronics design for data product generation. The details of the calibration and testing of the detector are described in Chapter 5.

Chapter 4

RADHEPT Electronics Design

This chapter describes the design of the RADHEPT electronics unit. The electronics unit interfaces with the various detector heads (RADHEPT-HE, RADHEPT-LE, and RADHEPT-MB), generates the data products and transfers the data to the spacecraft bus. The electronics chain is shown in Figure 4.1 depicting the various components required to generate the science data product from the raw detector output.

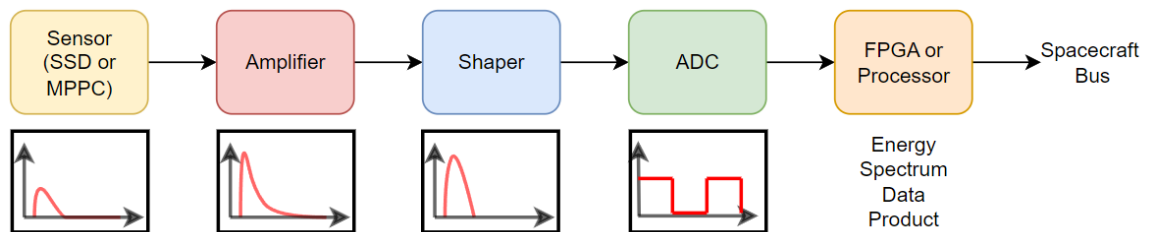


Figure 4.1: Schematic showing elements in the RADHEPT electronics readout chain.

This chapter first lists the key functional requirements of the electronics unit. This is followed by a discussion of the electronics architecture design. A description of each subsystem (board) within the electronics unit is given, together with details of circuit design. The chapter concludes with details about the electronics unit realization and board layout. The detailed schematics are provided in Appendix A.

4.1 RADHEPT Electronics Design Requirements

Table 4.1 lists the requirements of the electronics unit, including Spacecraft interface requirements (power and telemetry) and detector-head interface requirements. In the table below *shall* denotes a requirement and *should* denotes a recommendation.

No.	Functional Requirement	Details
1	The electronics unit shall operate using a 28V power supply from the spacecraft bus	Input Range: 24-32V (28V)
2	The electronics unit shall implement an RS-485 interface to transfer data to the spacecraft bus	Max. Data Rate: 25 Mbps 4 Wire differential interface
3	The electronics unit shall sample analog signals from the RADHEPT-HE,LE, and MB detector heads.	Total number of signals: 12 Duration of pulse: $1\mu\text{s}$ (approx.) Amplitude of Pulse: 2.5V Max. Count Rate: 200,000 cts/sec
4	The electronics unit shall provide bias High Voltage to the RADHEPT-HE,LE, and MB detector heads.	HE Bias: 60V and 200V LE Bias: 60V and 200V MB Bias: 60V
5	The electronics unit shall provide bipolar supply voltage to the amplifiers in the detector heads	Voltage: +12V and -12V
6	The electronics unit shall provide a trigger signal to the Search Coil Mag. on detecting a microburst	A 3.3V active high signal.
7	The electronics should collect housekeeping data (temperature, voltage, and current)	Monitoring performance, and generating diagnostics.

8	The electronics should implement redundancy between the three detector heads	Independent electronics should be used for the RADHEPT-HE, LE and MB heads
11	Part selection requirements (TID, LET)	TID: >20 krad LET: >37 MeV cm ² /mg

Table 4.1: RADHEPT Electronics Unit Design Requirements

4.2 RADHEPT Electronics System Architecture

The electronics unit architecture is shown in Figure 4.2. The electronics unit is designed with a modular design philosophy, and consists of two independent chains (as depicted in the figure). The top chain is for the RADHEPT-HE1, LE1, and MB1 detector heads and the bottom chain is the RADHEPT-HE2, LE2 and MB2 detector heads. This maintains redundancy between the two sets of detector heads. Each chain consists of three printed circuit boards (PCBs), which are named Power Management Board, Digital Processing Board and the Detector Interface Board. As the names suggest, the Power Management Board receives the 28V supply from the spacecraft and converts it to different voltages required by the instrument. The detector interface board consists of analog to digital converters (ADCs) that sample the analog signals from the detectors. The digital processing board consists of a System-on-Module FPGA that interfaces with the ADCs, and transfers data to the spacecraft bus over the RS-485 interface. The boards are stacked on each other and are interconnected using the PC-104 header (CubeSat standard interface). The modular design reduces the complexity of each board and also allows for easier debugging/testing since each of the boards can be replaced. The subsequent sections describe the detailed design of each of these boards.

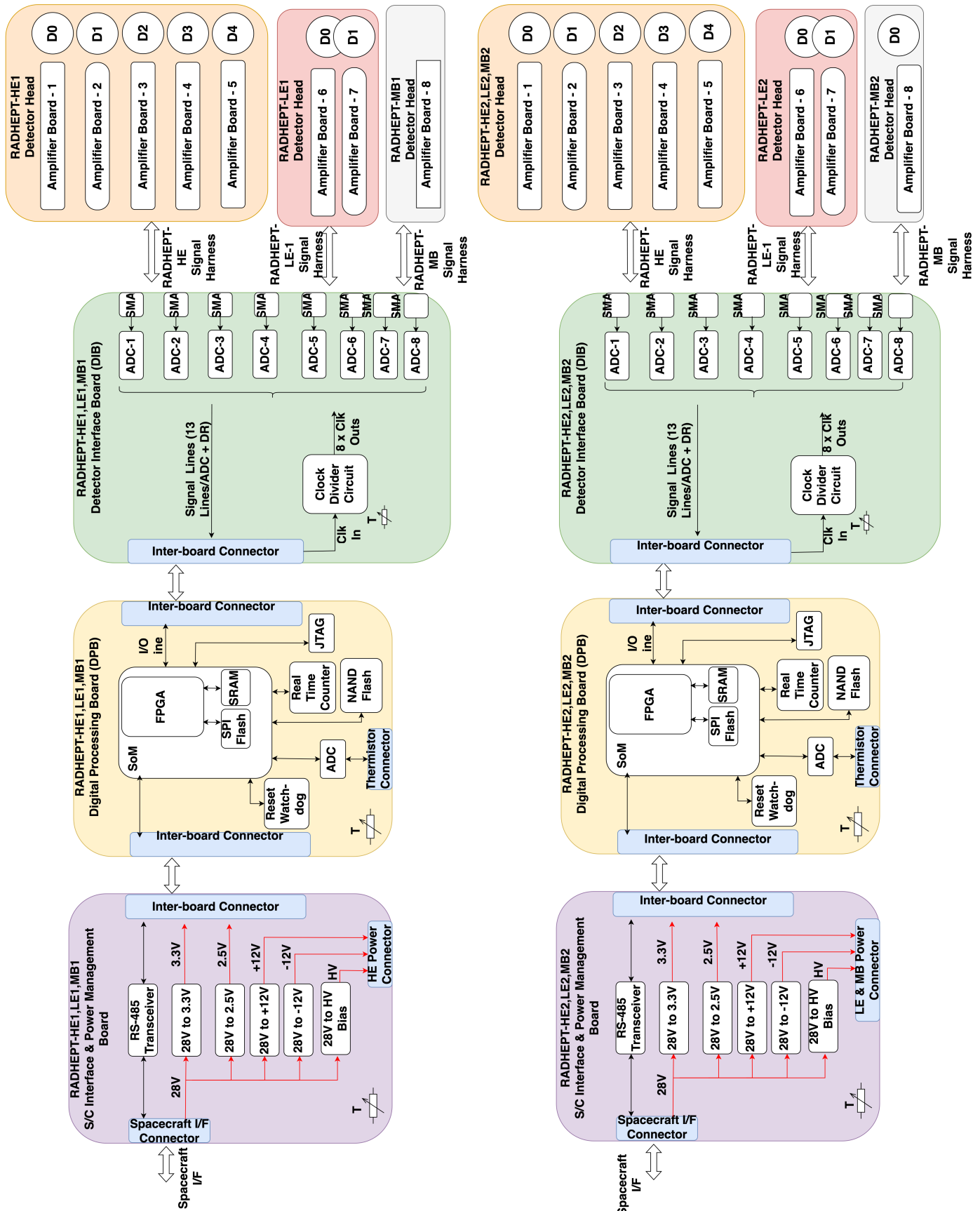


Figure 4.2: RADHEPT Electronics Architecture.

4.2.1 Component Selection Strategy

The goal while designing the electronics unit was that it could have a modular design suitable for multiple applications such as balloons, sounding cubeSats and micro-satellites. Thus, the component selection strategy followed was to select two sets of components, according to their radiation tolerance levels. Table 4.2 lists the chosen Commercial-Off-The-Shelf (COTS) and Space-Grade part for each component of the RADHEPT electronics unit. The first set is primarily based on (COTS) components. The COTS components chosen include a mix of industrial, automotive and military grade components. Additionally, most of the COTS components chosen have heritage from previous low Earth orbit missions. The second set of components were chosen to be Space-grade parts with a Total Ionization Dose (TID) and a Linear Energy Transfer (LET) specification as required by the RADICALS mission requirements (TID >20 krad and LET >37 MeV cm²/mg). This thesis describes the implementation of the COTS version of the electronics unit, as most of the Space-grade components are long-lead items such that their procurement and realization was beyond the scope of this thesis.

4.3 Power Management Board Design

The power management board consists of switching regulators and linear regulators to convert the 28V supply input to the different voltage levels required by the instrument. The powering scheme of the instrument is shown in Figure 4.3. Galvanically isolated switching regulators are used that keep the instrument electronics isolated from the spacecraft bus. Then, to generate lower voltage levels (such as 2.5V) linear Low Drop-Out (LDO) regulators are used. The board also consists of voltage-current (VC) sensors to monitor the voltage and current drawn by the different lines, and downlink them as diagnostic housekeeping data. A high voltage output (250V) converter is also added to generate bias voltage for the detector (solid state detector or multi-

S. No.	Component	COTS Part	S-Grade Part
1	FPGA	SmartFusion2	ProAsic3
2	ADC (Detectors)	LTC2226H	RHF1201
3	Regulators (Switching)	Traco-Power (THD-12)	VPT DC-DC
4	Regulators (Linear)	TPS73801	TPS73801-SEP
5	ADC (Housekeeping)	AD7998	STM LEOAD128
6	VC Sensor	INA3221, INA226	TBD
7	HV Bias Regulator	AH15P-5	Honeywell Design
8	DAC for HV	DAC121S	Honeywell Design
9	Buffer Opamp	LT1013	RH1013
10	NAND Flash	Micron MT29F	3D Plus
11	SD Card	San Disk	TBD
12	RS-485 Transceiver	MAX14786	MAX14786
14	Reset Watchdog	DS1388Z-33+	Renesas ISL706
15	Clock Divider	CDCLVC1310	ADH987S

Table 4.2: Component Selection

pixel photon counter). The details of operation of the high-voltage converter are provided in the next section. The grounding scheme of the instrument is depicted in Figure 4.4. The instrument follows the Single Ground Reference Point (SGRP) methodology [36]. The analog, digital and detector head grounds are shorted hence together at one point. This point is shorted to the instrument (spacecraft) chassis directly or through a 10 kOhm fault isolation resistor. The chassis of the RADHEPT electronics as well as the various detector heads are electrically bonded/grounded to the spacecraft chassis.

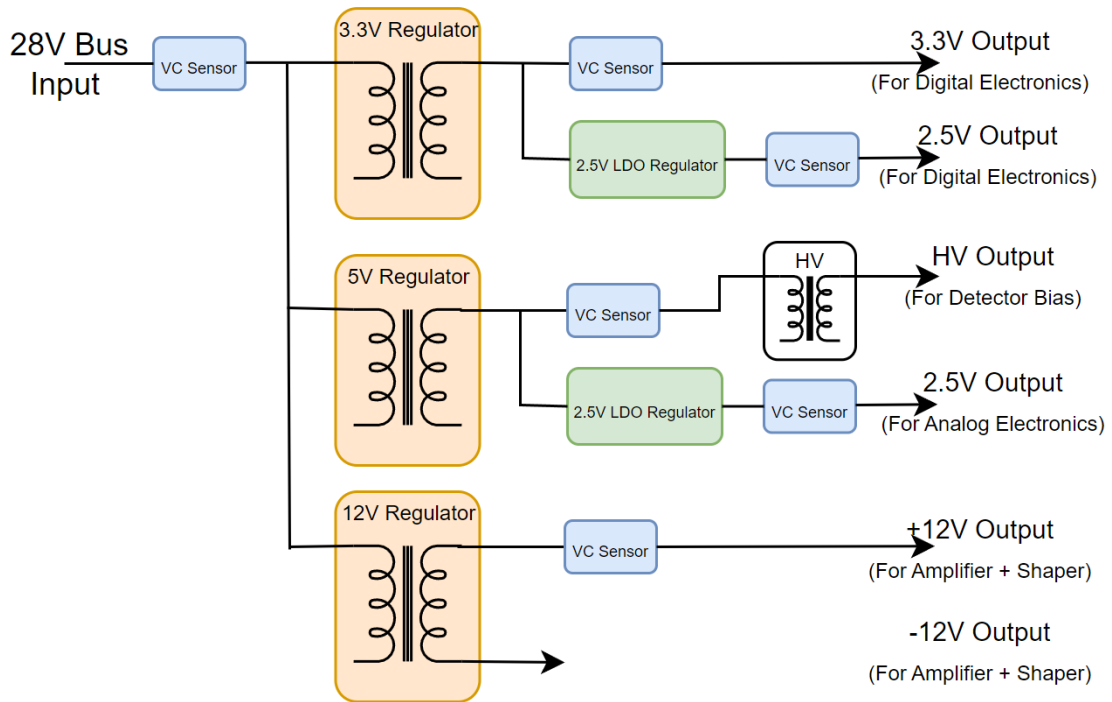


Figure 4.3: RADHEPT Electronics Powering Scheme.

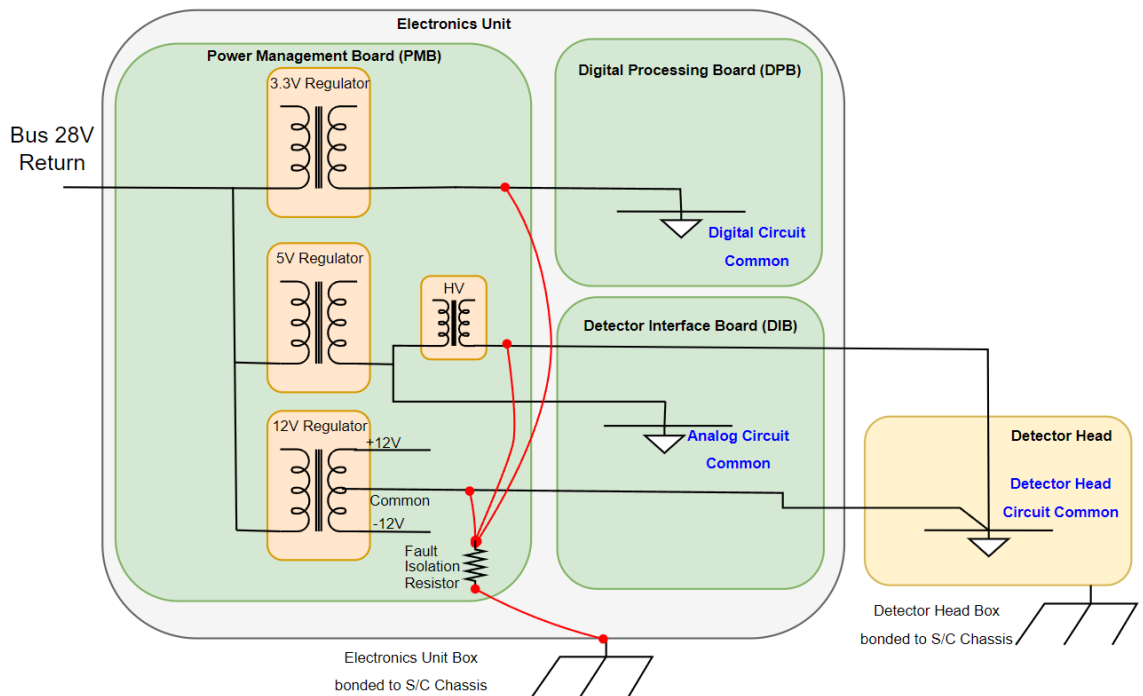


Figure 4.4: RADHEPT Electronics Grounding Scheme.

4.4 Digital Processing Board Design

The Digital Processing Board handles all the interfaces, including the detector ADCs, housekeeping sensors, and spacecraft telemetry interface. Table 4.3 lists the different interfaces of the board and the total number of I/O lines required.

	Number of ICs	No. of I/Os per IC	Total
ADC Interface	8	13 (12 data bits + 1 Data Ready)	104
Spacecraft Telemetry	1	3 (RO, DI, EN)	3
Watchdog IC	1	1 (Pet signal)	1
NAND Flash	1	17	17
SD Card	1	7	7
Debug UART	NA	NA	2
Housekeeping (Temperature, Voltage, Current, IMU)	2 x INA3221, 1 x INA226, 2 x ADCs (16 ch.) 1 x IMU	2 (Same I2C bus)	2
HV_DAC	1 x DAC	3	3
Regulator Enables	2 (1 per regulator)	2	2
SCM Trigger	NA	1 (GPIO)	1
FGM Interface	NA	2 (UART)	2
PPS Clock	NA	NA	1
		Total	145

Table 4.3: Digital Processing Board Interfaces.

Due to the high number of I/O lines required, the board design is based on a System-on-Module (SoM) Field Programmable Gate Array (FPGA). This consists of a FPGA and a micro-processor that provide re-configurable interfaces as well as computation capability. This board was designed to include RS-485 and RS-232

transceivers to interface with the spacecraft bus. The board was also implemented to include multiple levels of on-board memory to store the instrument data. The details of each of these components are described in the subsequent subsections.

4.4.1 System-on-Module (SoM)

The board uses the SmartFusion2 SoM, also referred to as the M2S-FG484I SOM, which is a Commercial-of-the-shelf (COTS) compact (30 mm x 57 mm) mezzanine module developed by Emcraft Systems [37]. The SoM includes the SmartFusion2 SoC FPGA[38] from Microsemi Corporation in an FG484 package, on-module clocks, a 64 MB LPDDR SDRAM (MT46H32M16) and a 16 MB SPI Flash (S25FL128SDPBHICO) on a single module (Fig. 4.5). The SoM is mounted on the board using two high density 80-pin (0.4 mm-pitch) connectors. These provide a total of 160 I/O pins which include 82 configurable GPIO interfaces in addition to the dedicated pins for UART (Universal Asynchronous Receiver-Transmitter), I²C (Inter-Integrated Circuit) and SPI (Serial Peripheral Bus) interfaces.

4.4.2 Peripherals

1. **Memory:** The board design includes of three levels of non-volatile storage, which are a 16 MB SPI Flash, a 16 GB NAND Flash and a 128 GB SD Card. The three memories can be used for different purposes: the 16 MB SPI flash is used for storing table parameters and instrument thresholds; The NAND flash is used to store the science data product and is the primary memory for downlinking data; and the SD card is used as a backup long-term storage and maintains a backup of all the instrument measurements.
2. **Housekeeping Bus:** The board has a serial (I²C) housekeeping bus which consists of multiple slave ICs on a single bus. Figure 4.6 depicts the housekeeping bus and the various sensors. This includes, voltage-current (VC) sensors used to monitor the voltage and current output of the different DC-DC converters

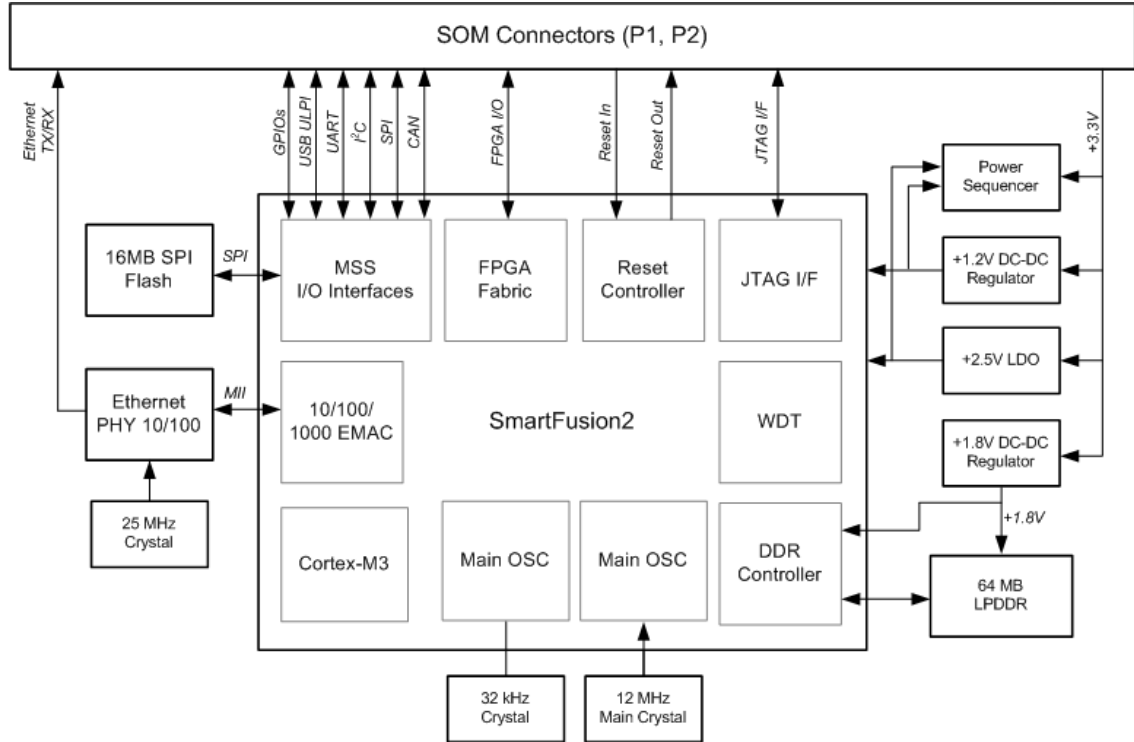


Figure 4.5: SmartFusion2 SoM Block Diagram [37].

on the power board. Additionally, two low sampling rate ADCs are added for temperature monitoring using upto 14 different thermistors. The chain also contains a Watchdog Reset IC with an integrated Real Time Counter. This IC serves two purposes: first it monitors the voltage of the board and triggers a reset if the voltage falls below a certain threshold (brown-out reset); second the IC also contains a real time counter the generates a timestamp which can be used to add temporal information to the data products.

3. **Closed Loop Bias High Voltage Supply:** The HV supply on the power board is operated can be operated in a closed loop feedback system. This is important because the gain of the detector depends on the high-voltage bias as well on temperature of the detector. Thus, the having a closed-loop feedback system allows tuning the bias supply value, based on temperature or other factors like on-orbit degradation of the detectors. Figure 4.7 depicts the feedback system. The output of the High Voltage converter is set using a 0-5V signal

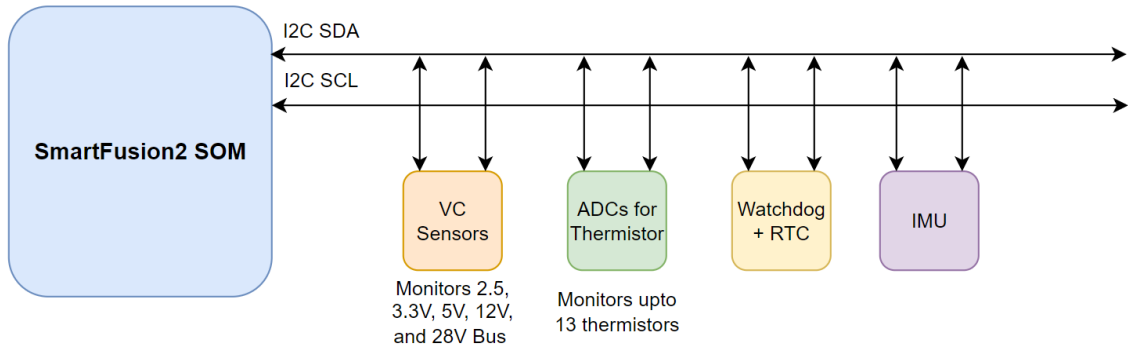


Figure 4.6: Serial (I2C) Bus for Housekeeping Data Collection.

that is set using a Digital to Analog Converter (DAC). The DAC is controlled by the processor in the SmartFusion2 SOM. The output of the HV converter is passed through a resistor divider and buffer and sensed using an Analog to Digital Converter. In this way the FPGA can monitor the output of the converter and change the value if necessary.

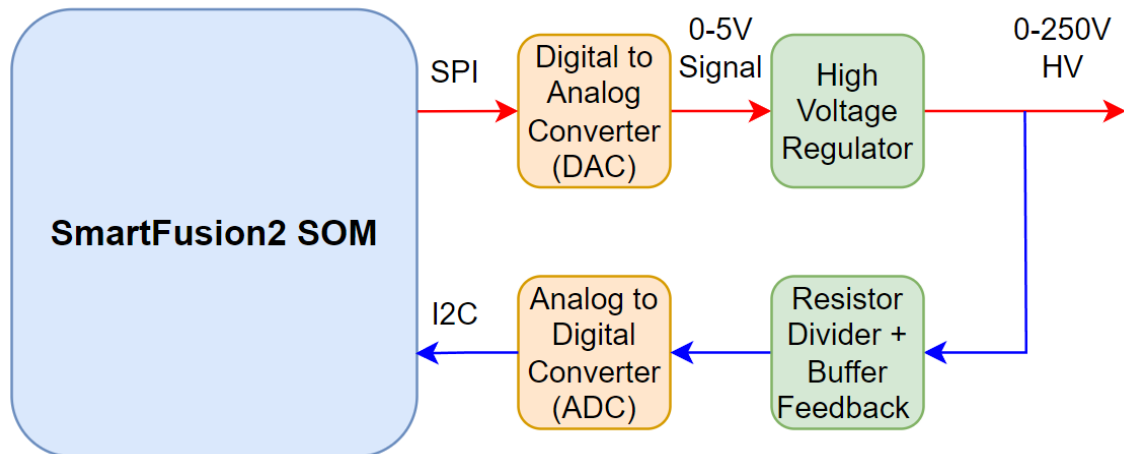


Figure 4.7: High Voltage Bias Feedback System.

4.5 Detector Interface Board Design

A version of the detector interface board was designed for the sounding rocket test flight instrument, that consists of two COTS ADCs. The COTS ADC consists of a transformer at the input of the ADC to convert the single ended detector output to

a differential analog signal. In order to extend this design for RADICALS HEPT, additional ADCs can be added to incorporate 6 or more detectors according to the RADICALS HEPT detector requirements. A clock divider circuit can also be added that splits the input clock from the FPGA to 6 identical clock outputs.

4.6 Electronics Unit Realization for the Sounding Rocket Test flight

The designs for the electronics boards were implemented through a build and integration of each board. Component level tests were performed on the boards, and appropriate modifications/corrections were made based on the tests performed. Finally, the integrated system was then tested, including calibration, as described in the next chapter. The detailed schematics and layout of the final flight boards designed for the sounding rocket test flight are provided in Appendix A. Although for the sounding rocket test flight commercial-of-the-shelf components are used, each schematic is designed in a modular fashion, using hierarchical schematic-sheets for different components. This allows a part to be changed in the design without having to edit the whole schematic, and consequently the COTS components can be swapped with Radiation tolerant components in the future.

Figures 4.8 and 4.9 show the 3D rendering of the Power Management Board and the Digital Processing Board, respectively, designed for the sounding rocket test flight. The layout of the boards are done with four layers, which are Signal (Top), Power Plane, Ground Plane, and Signal (Bottom).

Figure 4.10 shows an exploded view of the electronics unit and its three boards. The boards contain six M3 holes that can be used for mechanical interfacing with the electronics unit chassis using threaded rods with spacers. The boards are interconnected electrically using the PC-104 stack headers which can be used to transfer 104 electrical signals between the boards. For interfacing the boards with external subsystems, board mount gecko connectors are used which are connected to chassis-

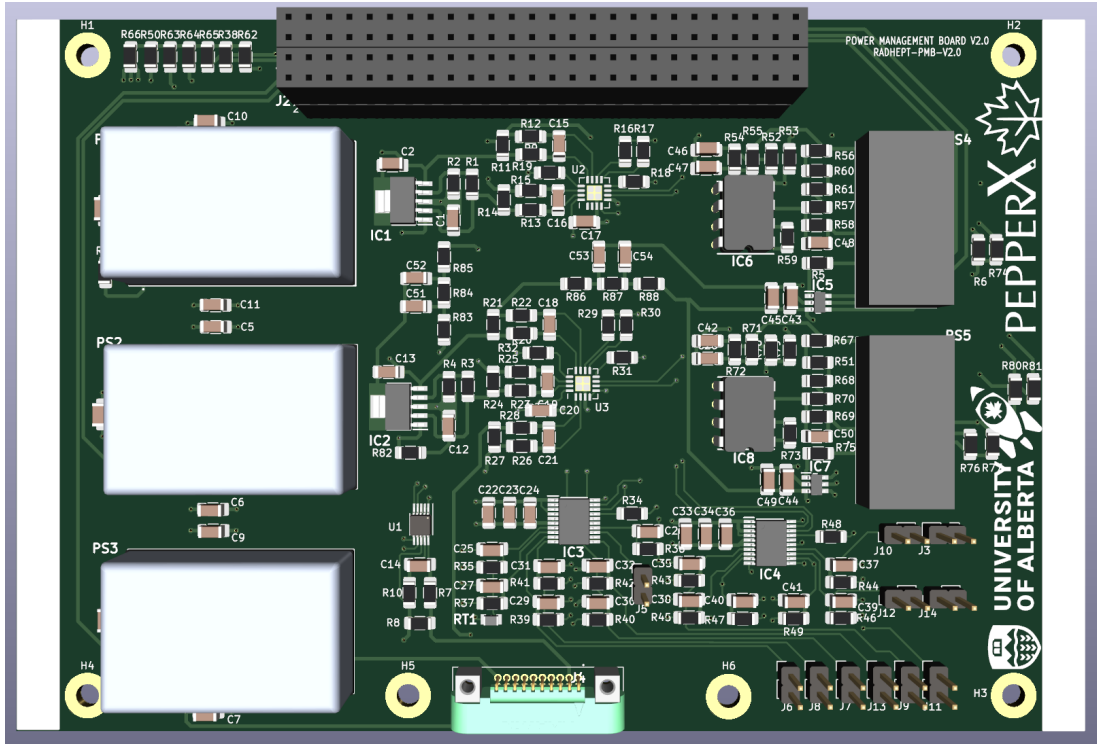


Figure 4.8: 3D Render of the Power Management Board.

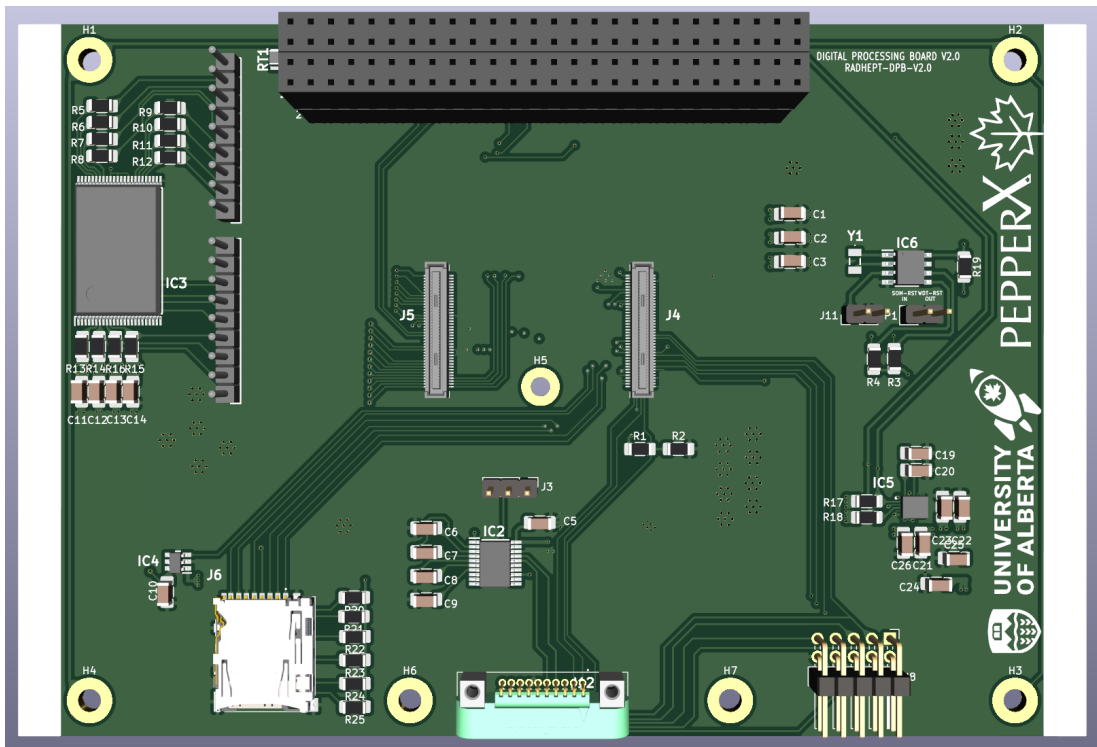


Figure 4.9: 3D Render of the Digital Processing Board.

mount D-Sub connectors on the electronics unit. Figure ?? shows pictures of the Power Management Board and the Digital processing taken during the assembly of the flight model of the electronics unit.

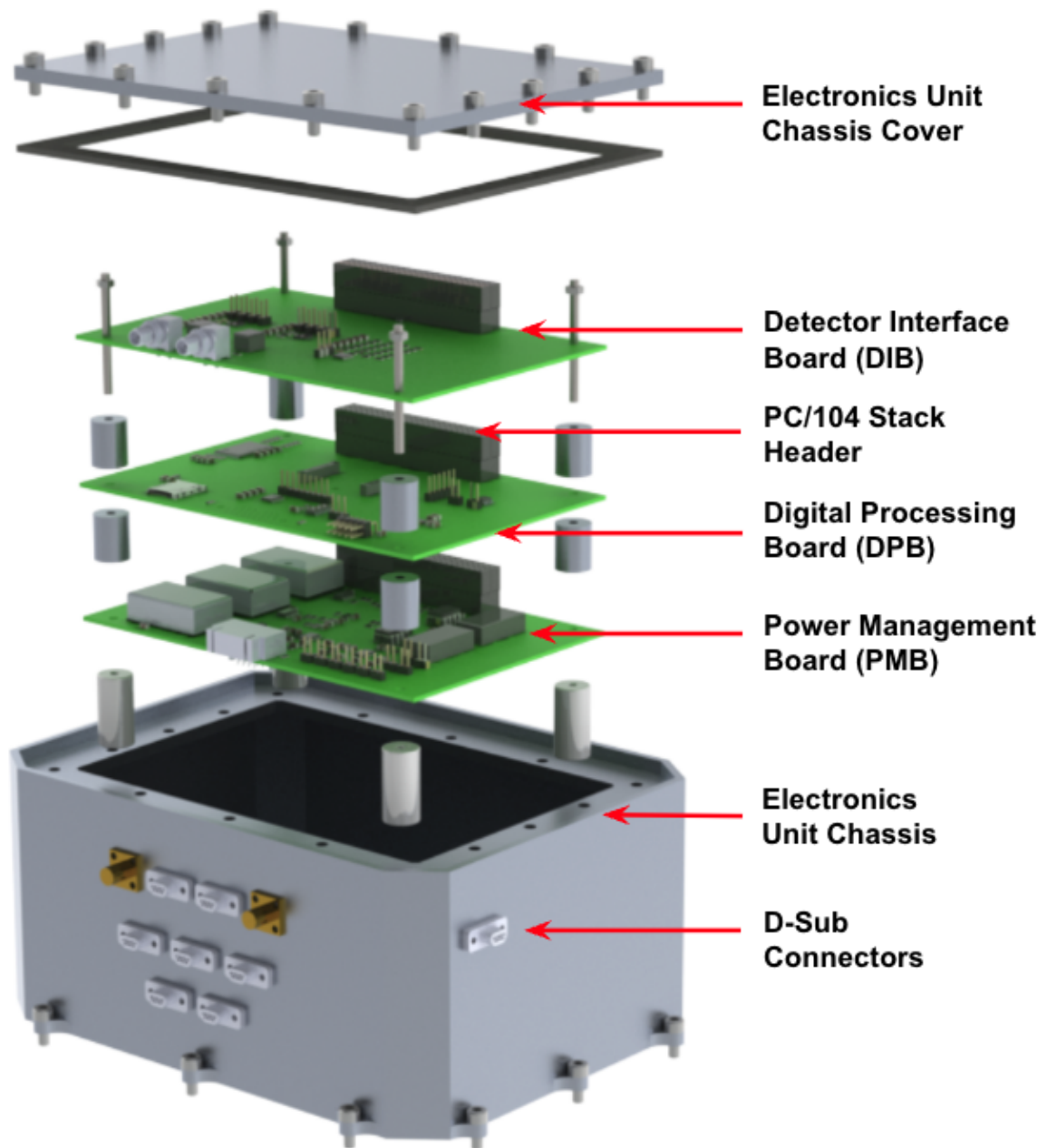


Figure 4.10: Electronics Board Stack design for the sounding rocket test flight. CAD Model Credit: Carl Berresheim, Dept. of Mechanical Engineering, University of Alberta.

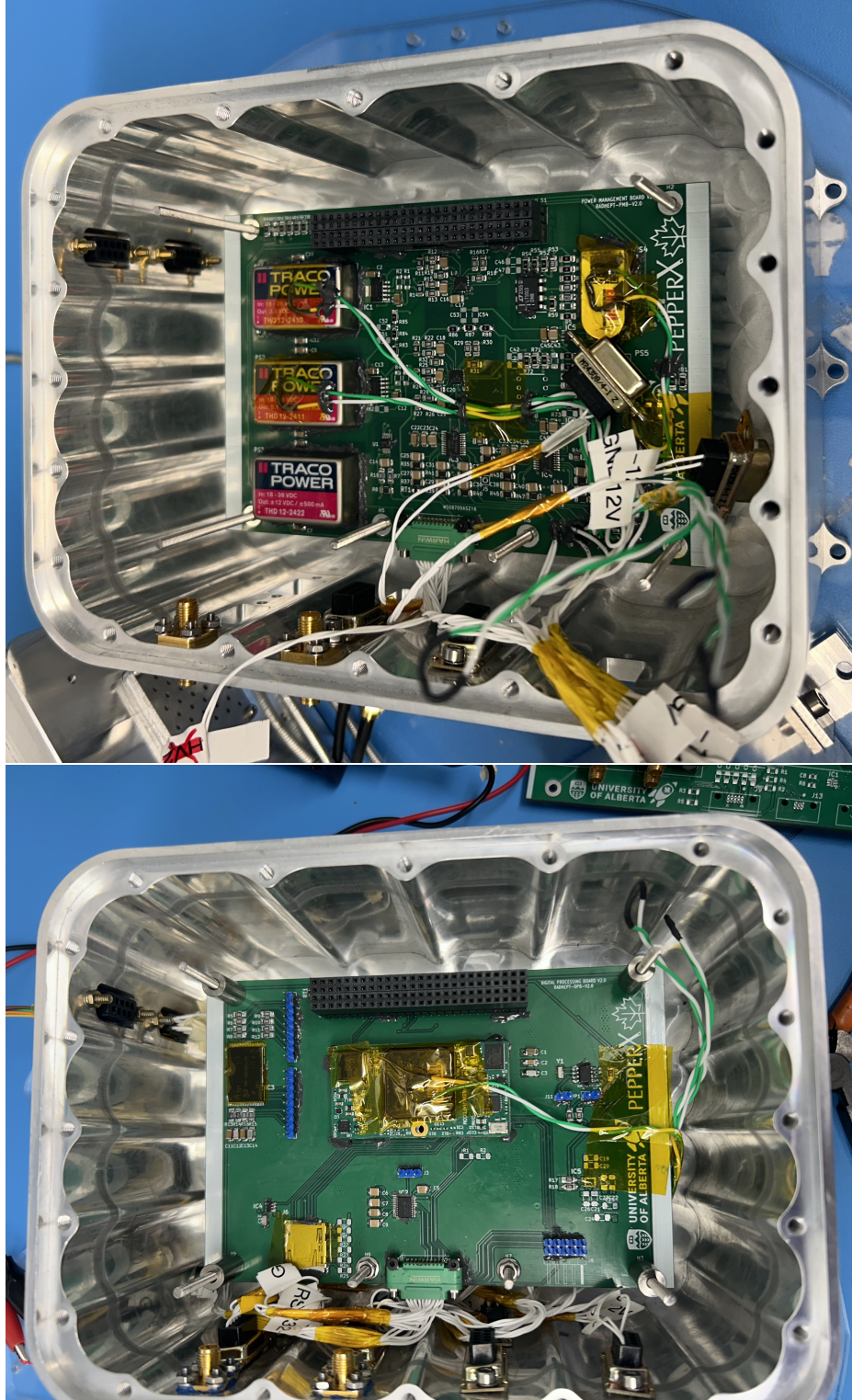


Figure 4.11: Top: Power Management Board and Bottom: Digital processing board pictures taken during Flight Model Assembly.

4.7 RADHEPT Electronics Design Summary

This chapter provided an overview of the designs developed and implemented for the RADHEPT electronics unit. A system level architecture for the electronics was developed based on a modular design philosophy. This modular approach enables the use of the instrument for a flight on a variety of platforms including balloons, sounding rockets, cubesats, and micro-satellites. Specifically, a component selection strategy was implemented, that supports the implementation of two versions: one based on commercial-off-the-shelf (COTS) parts; and the other based on rad-hard space-grade parts. Details of board circuit design, layout, and realization for the sounding rocket test flight electronics unit were described. Chapter-5 provides details of the testing and calibration of the electronics unit and detector system.

Chapter 5

Testing and Calibration

This chapter presents the calibration and testing performed to characterize the performance of the detector and electronics whose design development and implementation was described in chapters 3 and 4. The overall objective for the instrument is to produce a scientifically useful data product comprising a histogram of electron counts as a function of energy over the energy range of scientific interest. This can then be converted into units of flux or differential flux with appropriate calibration and processing. The instrument functionality can be summarized as follows. The detector (combination of the scintillator with the multi-pixel photon counter (MPPC)) generates a charge output that depends on the energy of the incoming electron and produced as a result of the electron generating photons in the scintillator which are then incident upon the MPPC. The signal conditioning electronics are responsible for converting this charge into a voltage, digitizing the voltage signal, finding the peak, and binning the voltage into different energy bins. In order to generate an accurate energy spectrum, each of these steps needs to be tested and calibrated. This chapter presents the various tests performed to achieve this goal and is divided into three sections: detector testing; electronics testing; and end-to-end instrument testing.

5.1 Detector Testing

This section describes the tests performed to calibrate the detector and is divided into two subsections. The first subsection describes the tests used to characterize dark noise, and the second subsection describes calibration using Radio-isotope sources.

5.1.1 Dark Noise Characterization

The multi-pixel photon counter generates an output charge when an incoming photon that is produced as a result of the interaction between the incident electron and the scintillator crystal, hits the detector. However, charge pulses are also generated from intrinsic thermally generated carriers in the MPPC, which are called dark pulses. Dark pulses can be generated when one thermally generated Photo-electron (p.e.) triggers one pixel, which are called 1 p.e. pulses. Additionally it is possible that secondary photons are generated in the avalanche process that triggers adjacent pixels. This can lead to two photo-electron (2 p.e.) or three photo-electron (3 p.e.) pulses contributing to the dark pulses. These all lead to a dark current, I_D , which can be computed as follows:

$$I_D = qMN_{fired} \quad (5.1)$$

$$I_D = qMN_{0.5p.e.} \frac{1}{1 - P_{crosstalk}} \quad (5.2)$$

where, q denotes the charge of an electron, M is the gain of the MPPC, N_{fired} denotes the number of pixels in which avalanche multiplication occurs per unit time, $N_{0.5p.e.}$ is the dark count rate which is defined as the number of pulses generated in a dark state that cross the threshold of 0.5 p.e., and $P_{crosstalk}$ denotes the probability of crosstalk happening (See e.g., [39] for more details). $N_{0.5p.e.}$ and $P_{crosstalk}$ can be computed as follows:

$$N_{0.5p.e.} = AT^{\frac{3}{2}} e^{\frac{-E_g}{2kT}} \quad (5.3)$$

$$P_{crosstalk} = \frac{N_{1.5p.e.}}{N_{0.5p.e.}} \quad (5.4)$$

Here T is the absolute temperature (in Kelvin), A is a arbitrary constant, E_g is the band gap energy (1.12 eV for the silicon detectors used in this study), k is the Boltzamn constant (eV/K), and $N_{1.5p.e.}$ is the number of pulses generated in a dark state that cross the threshold of 1.5 p.e. (See e.g., [39] for more details). Figure 5.1 shows the expected dark count rate variation with temperature in the left plot and the variation in the crosstalk probability with the applied overvoltage, for an MPPC with pixel pitch of 50 micrometers [39]. From Figure 5.1 it can be seen that at 25 Celsius and with an over voltage of 3V, the dark count rate is expected to be 4.5×10^5 counts per second.

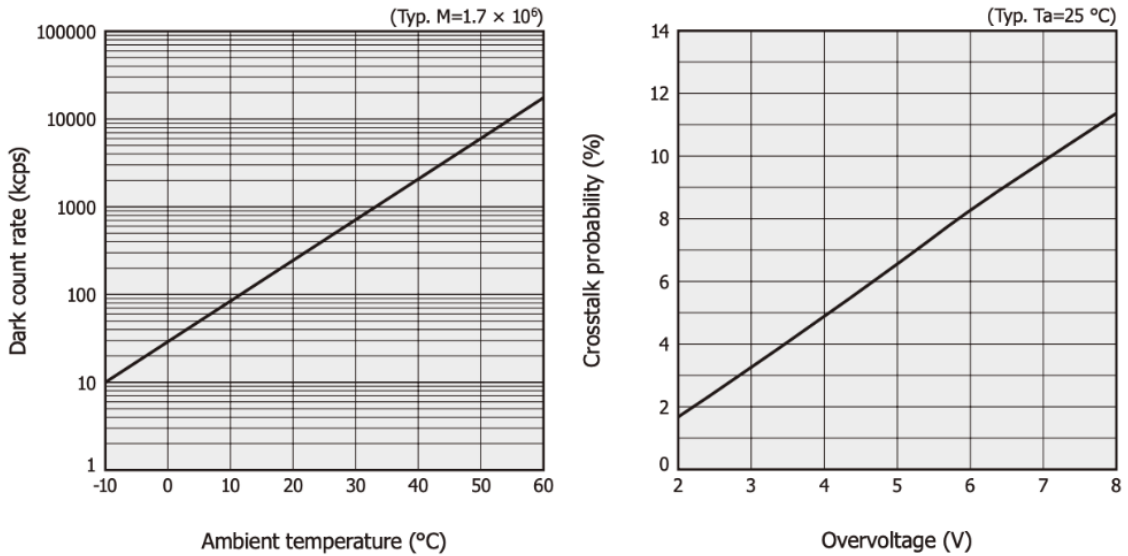


Figure 5.1: Left: Dark count rate (kcps) variation with temperature, Right: Crosstalk probability variation with overvoltage for an MPPC with 50 micrometer pixel pitch. Reproduced from reference [32], for typical MPPC parameters of M (Gain) = 1.7×10^6 and Temperature of 25 Celsius

Thus by measuring the dark current at a given temperature, and with a knowledge of the self-breakdown rate, the gain of the MPPC can be determined as a function of voltage. Figure 5.2 (left) shows the test setup schematic. Figure 5.2(right) shows the implementation in the laboratory. Specifically, the left panel shows the circuit where the detector is connected to a oscilloscope with a $1 \text{ M}\Omega$ input resistance. A bias voltage is applied to the detector that is 3V above the breakdown voltage (as

recommended by the manufacturer [32]). The MPPCs chosen for use in this detector have a pixel pitch of 75 micrometers, and correspondingly the dark count rate given by the manufacturer is approximately 2000 kcps at 25 Celsius and the crosstalk probability is 7 percent [32].

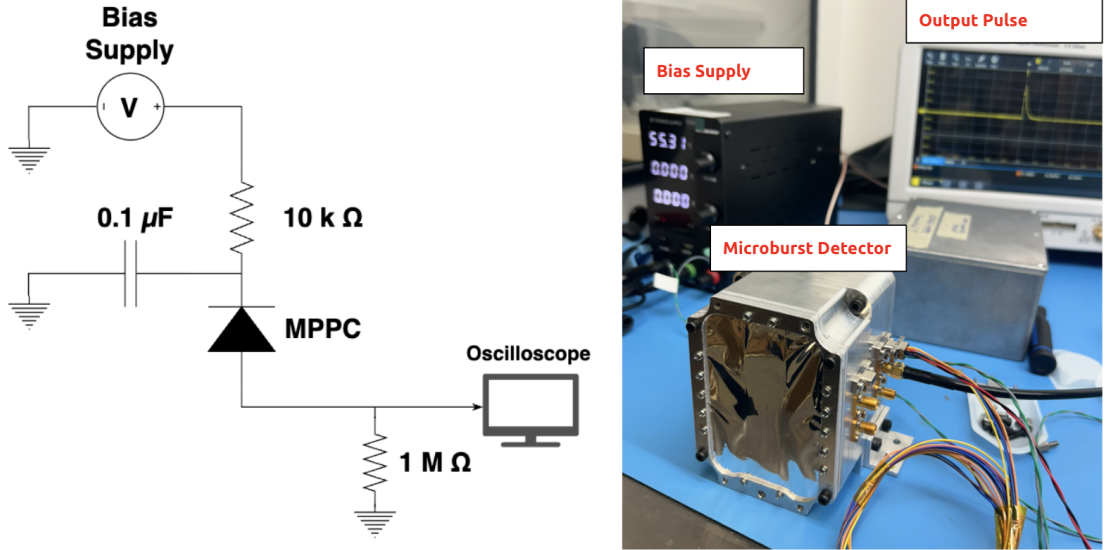


Figure 5.2: Microburst detector Dark noise characterization test setup. (left) Schematic of electrical connections; (right) the test set up as implemented in the laboratory.

Three scintillator crystals were examined for their potential use on the instrument, which are BGO, LYSO and CsI(Na). The oscilloscope outputs for the LYSO crystal are shown as an example, and similar results from other crystals are omitted here for brevity. Figure 5.3 (top) shows the 1 Photo-electron (PE), 2-PE, 3-PE Pulses, measured using a 50 Ohm termination with the scope. Figure 5.3 (bottom) shows the leakage current of the LYSO crystal (right). The baseline voltage in the 5.3 (bottom) oscilloscope trace for LYSO crystals across the 1 MΩ input resistance is 580 mV, which implies that the leakage current is

$$I_D = \frac{V_{scope}}{1M\Omega} \approx \frac{580mV}{1M\Omega} \approx 0.58\mu A \quad (5.5)$$

Then, the gain of the MPPC can be calculated by combining equations Equation (5.1)

and Equation (5.5),

$$M = \frac{I_D}{qN_{0.5p.e.} \frac{1}{1-P_{crosstalk}}} \approx \frac{0.58 \cdot 10^{-6}}{1.602 \cdot 10^{-19} \cdot 2000 \cdot 10^3 \cdot \frac{1}{1-0.07}} \approx 1.68 \cdot 10^6 \quad (5.6)$$

This value is reasonably close to the expected value provided by the manufacturer, which is typically stated as 4.0×10^6 [32]. The difference in the measurement could be attributed to the approximations made in the dark count rate, as well as differences in the breakdown voltage in different MPPC detectors. For the LYSO crystal scintillation spikes are seen to occur (Figure 5.3 (bottom)) randomly in time due to the self scintillation within the crystal.

The self-scintillating lutetium yttrium oxyorthosilicate (LYSO) crystal consists of about 2.6% of ^{176}Lu , which is a natural isotope of Lutetium. ^{176}Lu decays by beta-emission followed by one or more gamma-ray emissions to ^{176}Hf , with a half-life of $3.76 \cdot 10^{10}$ years [40]. These ionizing radiation emissions (beta or gamma emissions) lead to the scintillation process within the crystal. During this process, the electrons within the scintillator crystal are excited from the valence band to the conduction band creating electron-hole pairs. The excited electrons are then trapped in activator sites in the crystal (for example a deliberately introduced dopant such as Cerium), and subsequently decay back by emitting a photon [41]. These photons can then be measured using the Silicon Photomultiplier, and the energy spectrum can be compared to the previously computed theoretical spectrum (for example reference [40]). Figure 5.3 (bottom) shows that there are 8 self-scintillation pulses in a duration of 200 milliseconds, which is approximately 40 counts/second. This is close to the to the expected decay rate for ^{176}Lu , with a half-life of $3.76 \cdot 10^{10}$ years [40].

5.1.2 Radio-isotope Calibration

In this calibration test the detector was tested with different radioisotope sources. Since the energy spectrum of the sources are known, the detector output response can be compared to the source spectrum to obtain calibration results for the detector.

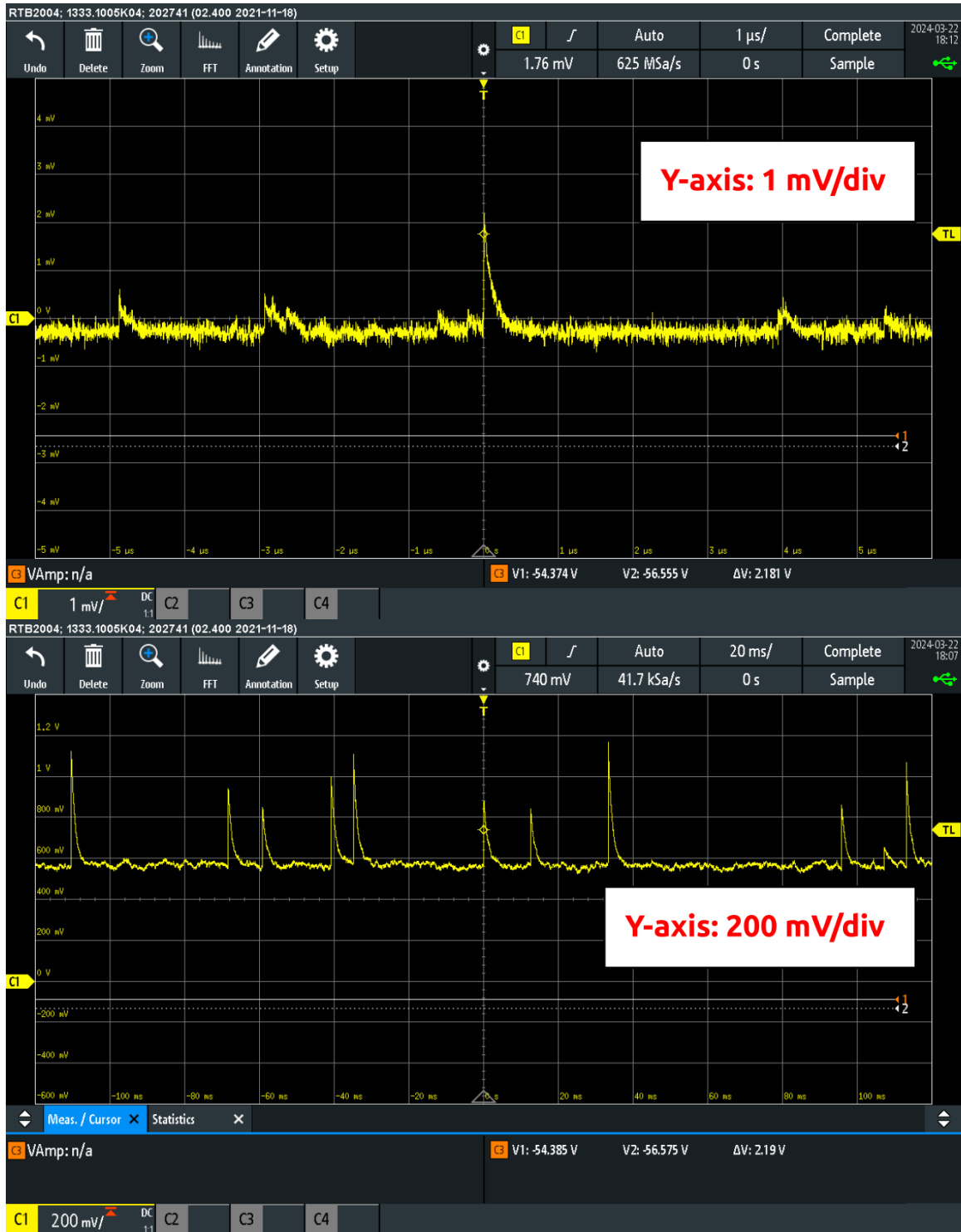


Figure 5.3: Top: LYSO Crystal 1 Photo-electron (PE), 2-PE, 3-PE Pulses (measured using a 50 Ohm termination with the scope); Bottom: Leakage current and self scintillation pulses of the LYSO crystal in the detector, measured using a 1 MOhm termination with the oscilloscope

Figure 5.4 (top) shows a schematic of the test setup for the radioisotope calibrations. The detector is connected to a bias supply, and the radiation source is placed near the detector (as shown in Figure 5.4 bottom-left). The source is placed on a 3D printed cover with a hole aligned over the scintillator crystal (with the diameter of the hole larger than the crystal size), such that the source simulates a point-source of radiation. Figure 5.4 bottom-right shows a zoomed-in picture of the radioisotope source. The output of the detector is connected to an oscilloscope to monitor and store the output pulses. The output pulses are then binned and a histogram plot is created of the emission spectrum. The subsequent subsections show the calibration results obtained from using different radioisotope sources.

LYSO self-scintillation spectrum

Figure 5.5 shows the measured energy spectrum with respect to peak voltage in the top panel and the theoretical spectrum in the bottom panel, for the self scintillation of the LYSO crystal. In the top panel of figure 5.5, the energy spectrum measured using the detector is shown and includes the histogram, as well as a smoothed curve generated using kernel density estimation. The kernel density estimate is calculated as follows:

$$f_h(x) = \frac{1}{nh} \sum_{i=1}^n \frac{K(x - x_i)}{h} \quad (5.7)$$

where, $x_1 \dots x_n$ are the n histogram data sample points, K is the Gaussian kernel function, and h is the smoothing parameter.

The horizontal axis of the top panel of figure 5.5 is the peak voltage (in V) and the horizontal axis of the bottom panel is electron energy (in keV). Thus, by comparing the two, a rough estimate of the sensitivity (in keV/V or keV/mV) can be obtained. For this study, the crystal is cubic with sides of length 0.5 cm, and the self-scintillation spectrum is similar to the plot on the bottom panel of Figure 5.5, which shows results for self-scintillation of 1 cm³ cube of LYSO (reproduced from reference [40]). Previous

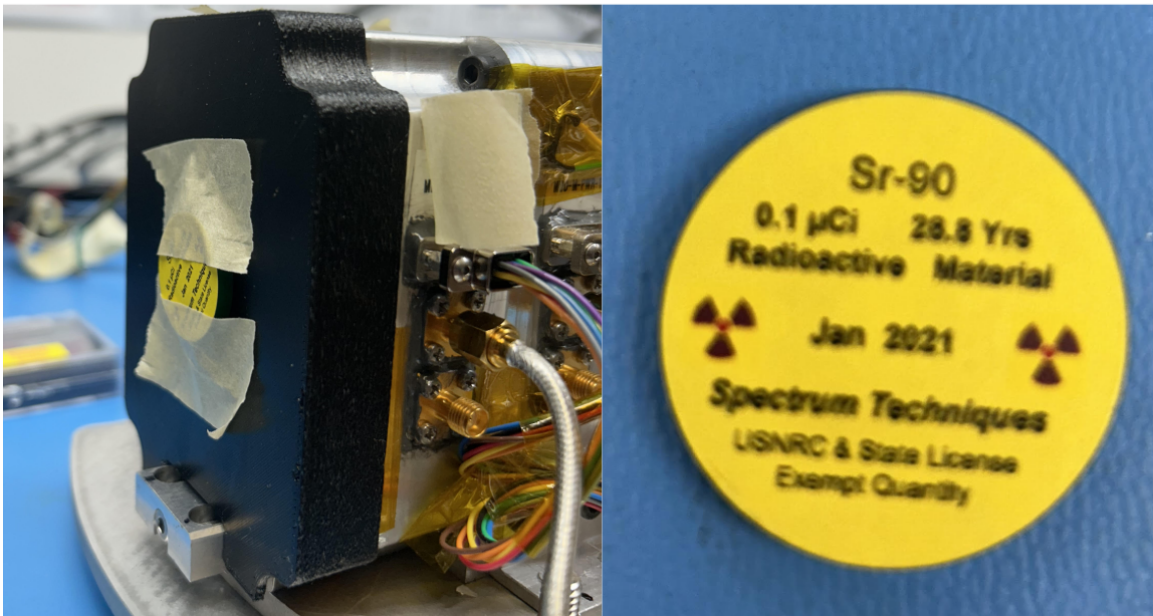
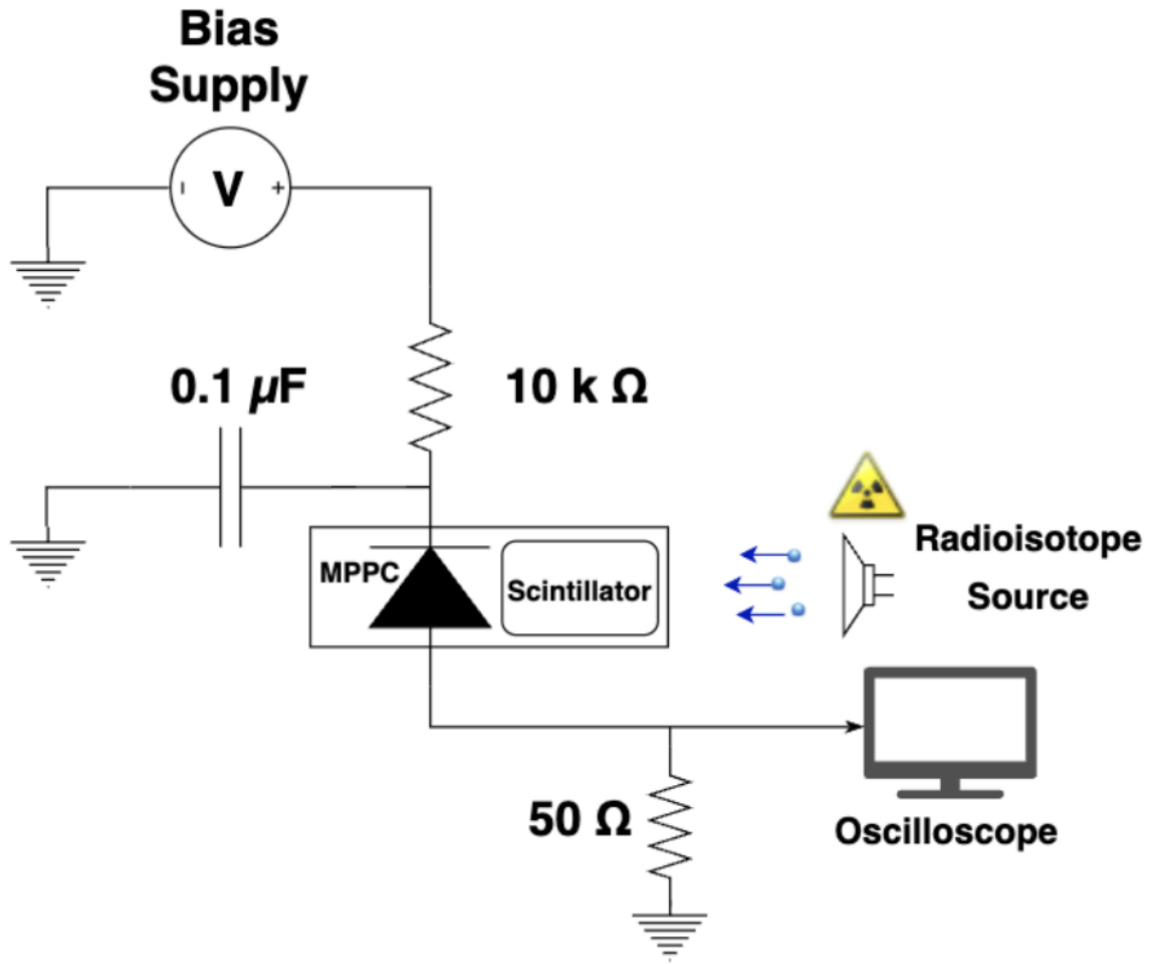


Figure 5.4: Top: Schematic of the microburst detector Radioisotope Calibration test setup; Bottom-Left: Implementation of test-setup in the laboratory; Bottom-Right: Zoomed-in picture of the source

work (for example see reference [40]), shows that the self-emission spectrum measured in a LYSO crystal depends on the size of the crystal. This can be attributed to the increase in probability of self-detection of higher energy peaks, which results in an increase in the relative intensity of higher energy peaks for larger crystals. Additional details of the sensitivity estimation are described in Section 5.5 (integrated instrument calibration).

BGO Barium Spectrum

Figure 5.6 shows the Barium source X-ray energy spectrum plot measured by the BGO crystal detector (left plot) and the Barium reference spectrum.

BGO Strontium-90 Spectrum

Figure 5.7 shows the Strontium source electron energy spectrum measured by the BGO crystal detector (left plot) and the reference spectrum (right plot).

Based on these measurements a rough estimate of the sensitivities of the BGO detector and the LYSO detector were obtained as 20 mV/keV and 2 mV/KeV by visual comparison with the reference spectra (at a bias voltage of 3V over the breakdown voltage). These measurement were taken without the inclusion of the electronics unit, and thus to determine the the calibration of the integrated instrument, additional measurements were taken after the detector and electronics unit were assembled. These account for the electronics noise (ADC noise, regulator switching noise etc.) as well as the peak-finding and binning procedure of the FPGA. Additionally, after integrating with the electronics a drift in Bias Voltage (MPPC gain) with temperature was observed (more details in subsequent subsections), and thus it was decided to operate the MPPC at a higher bias voltage of 57V (which is an overvoltage of approximately 5V, leading to twice the gain). The estimates of the sensitivities at this bias voltage and comparisons with theoretically obtained sensitivities of the integrated instrument are described later in this chapter.

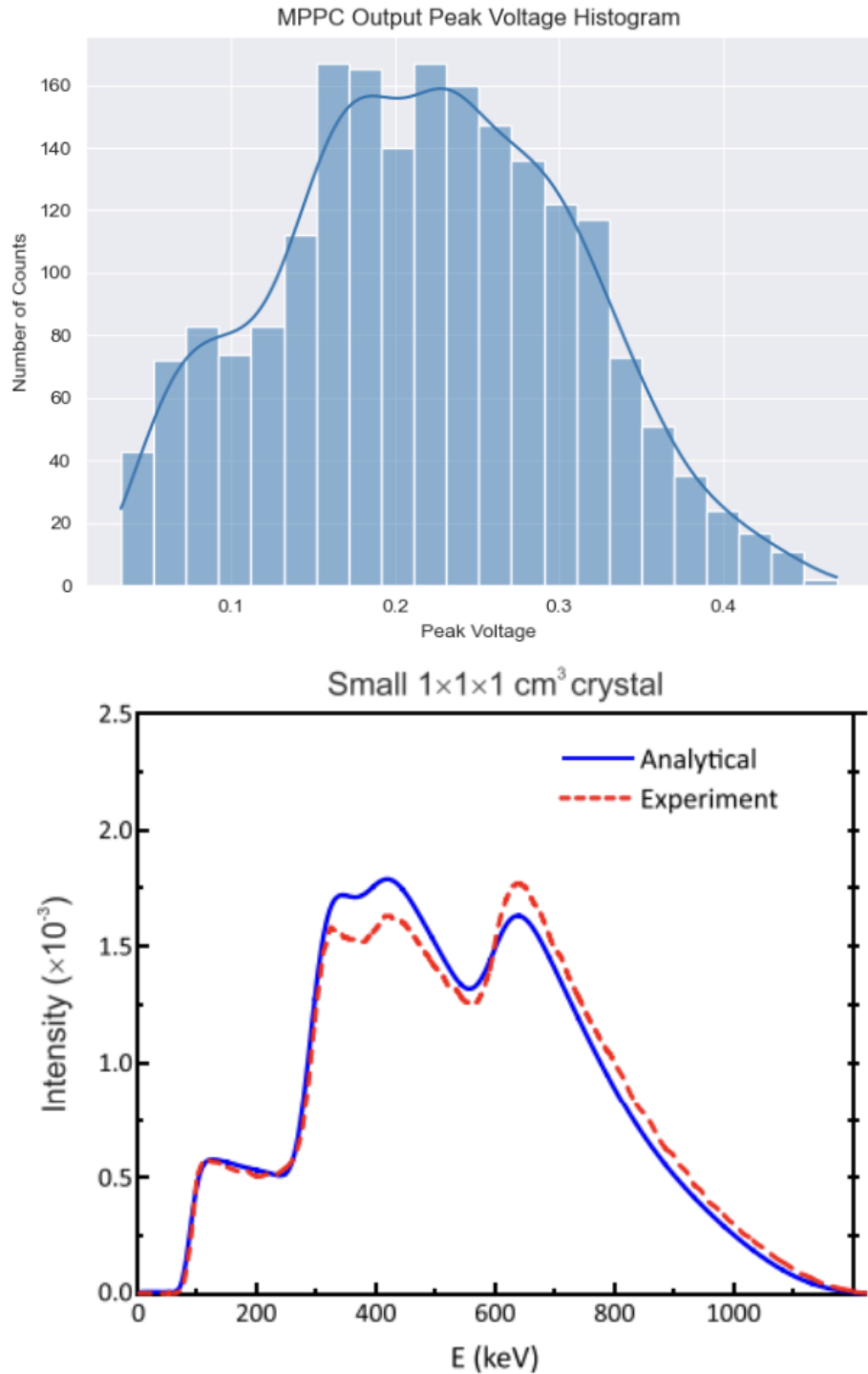


Figure 5.5: Top: Measured LYSO self-scintillation spectrum; Bottom: LYSO self-scintillation spectra for a 1x1x1 cm³ crystal (reproduced from reference [40]).

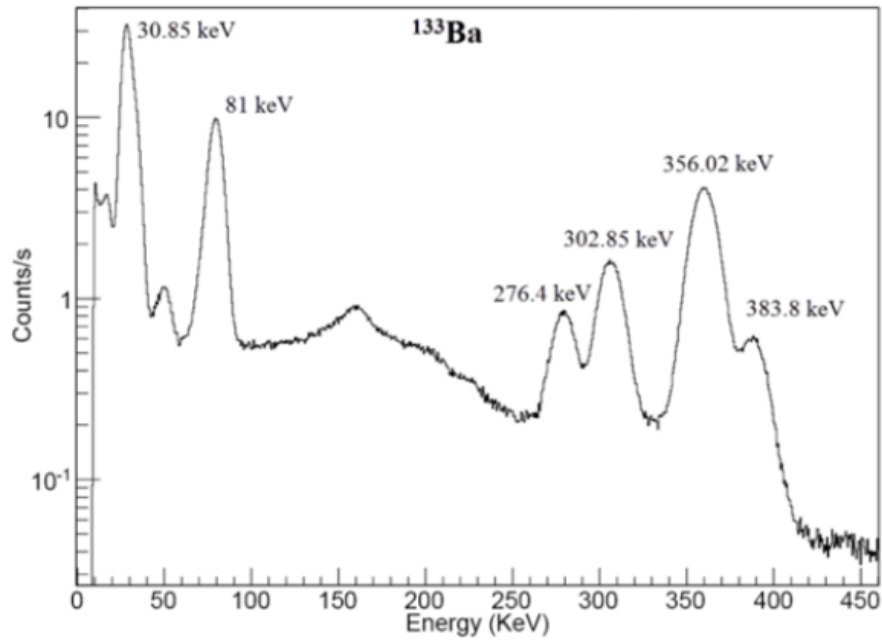
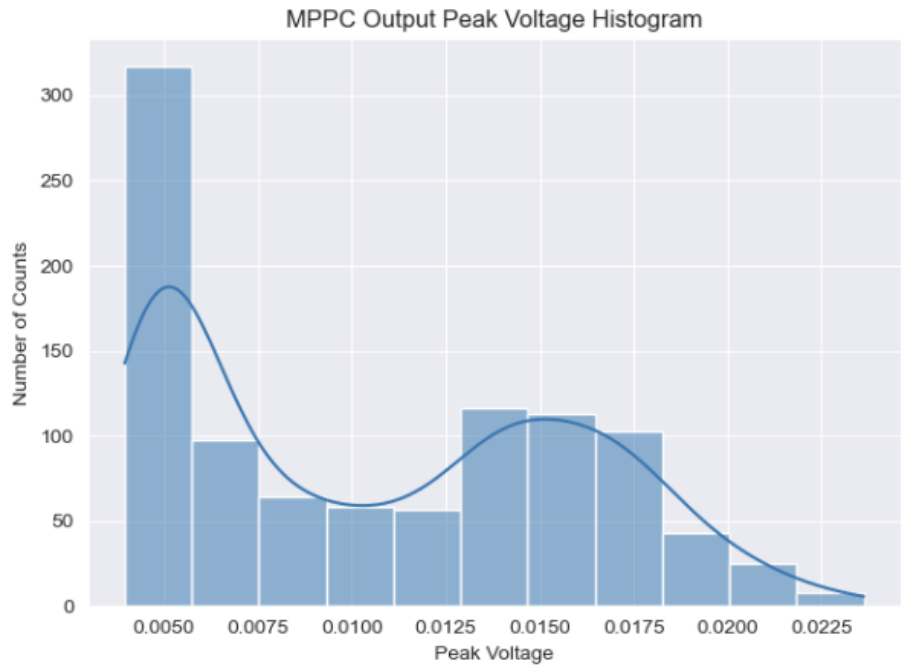


Figure 5.6: Top: Barium source spectrum observed with the BGO detector; Bottom: Barium reference spectra (reproduced from reference [42]).

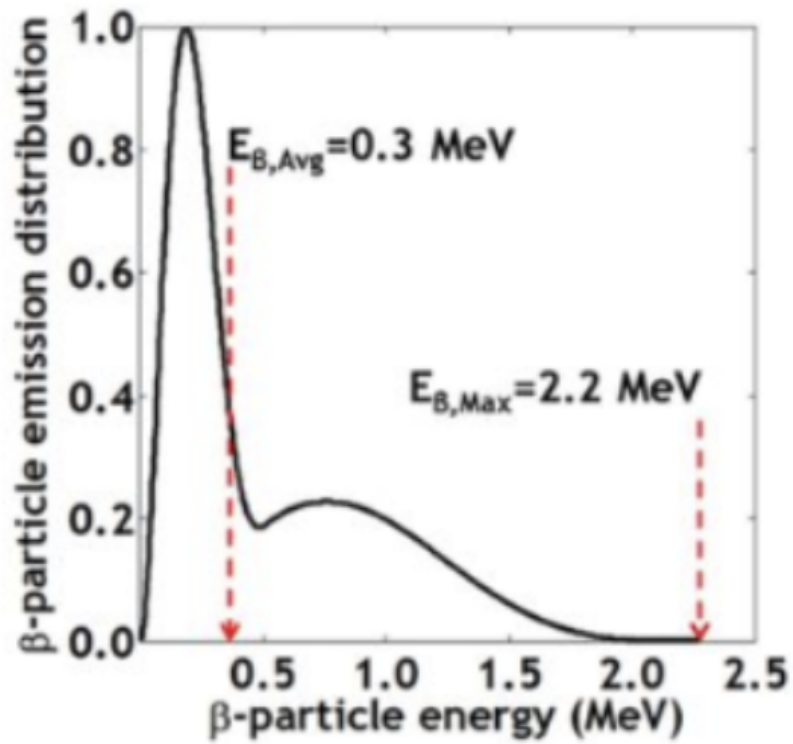
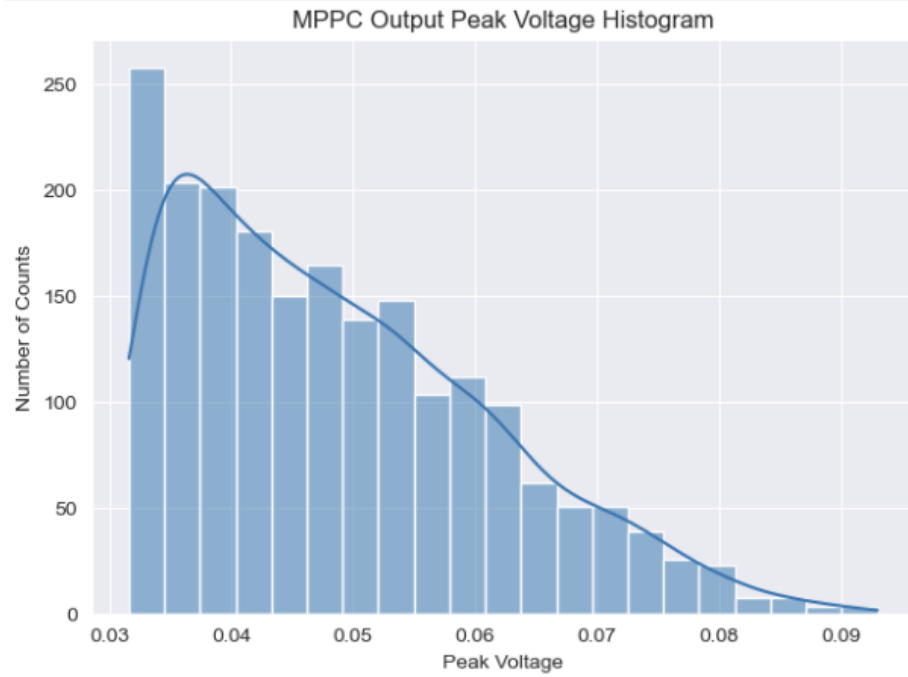


Figure 5.7: Top: Strontium source spectrum with BGO detector; Bottom: Strontium reference spectrum (reproduced from reference [43]).

5.2 Electronics Testing

In order to validate the functionality and performance of the overall electronics unit, a “bottom-up” testing philosophy was followed, which consists of incrementally building the system. Thus, first a component level testing of different electronics components was conducted. This was followed by subsystem level tests of the different printed circuit boards (PCBs). Once the functionality of the individual boards was verified, the boards were integrated and connected together on a bench-top similar to a “flat-sat” test setup. After the functionality of all three boards was verified together, they were then stacked together, and tests were performed on the integrated system. In this section, a digitization test conducted on integrated electronics unit is described below; and other component-level and subsystem-level tests are omitted here for brevity but which were completed successfully prior to integration.

An integrated bench test of digitization electronics was performed with an artificially generated sinusoidal input signal. Figure 5.8 shows the electronics test setup. The three boards of the electronics unit (namely the power management board, the digital processing board, and the detector interface board) are stacked together. A sinusoidal input is connected to the analog to digital converter of the detector interface board using a signal generator. This test was repeated for sinusoidal input signals of different frequencies from 100 kHz to 1 MHz as well as different amplitudes from 10 mV to 2V peak-to-peak (p-p) signal delivered to the instrument from an external signal generator. As an example, the input signal (1 p-p and 1 MHz) and digitized output from the electronics unit are shown in figure 5.9.

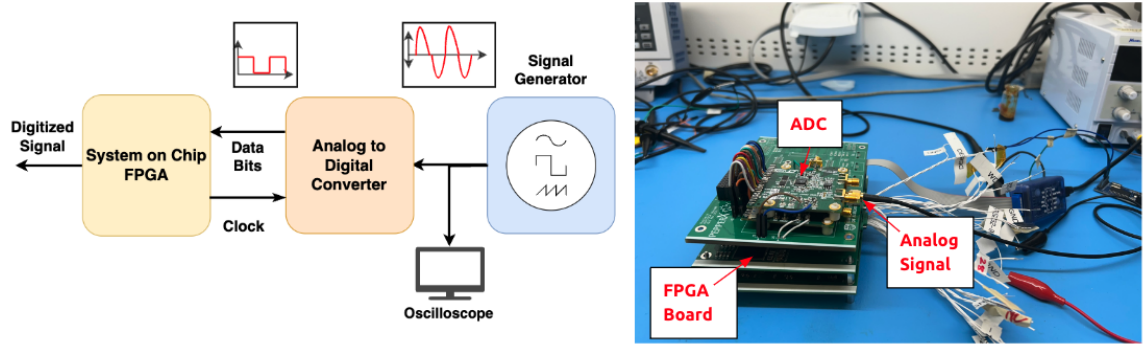


Figure 5.8: Electronics testing setup for validating the performance of the electronics digitisation using an analog source signal.



Figure 5.9: Analog sine wave input signal and digitized sine wave output signal.

5.3 Detector and Electronics Integrated Testing

Once the detector and electronics were independently tested, an end-to-end integrated test of the instrument was performed. In this test, the detector and electronics unit

were assembled on a replica of the sounding rocket deck as shown in Figure 5.10. The housekeeping data from the electronics unit was logged every one second, to a simulated RS-232 telemetry interface of the rocket. The subsequent subsections describes the housekeeping telemetry plots obtained during the integrated testing.

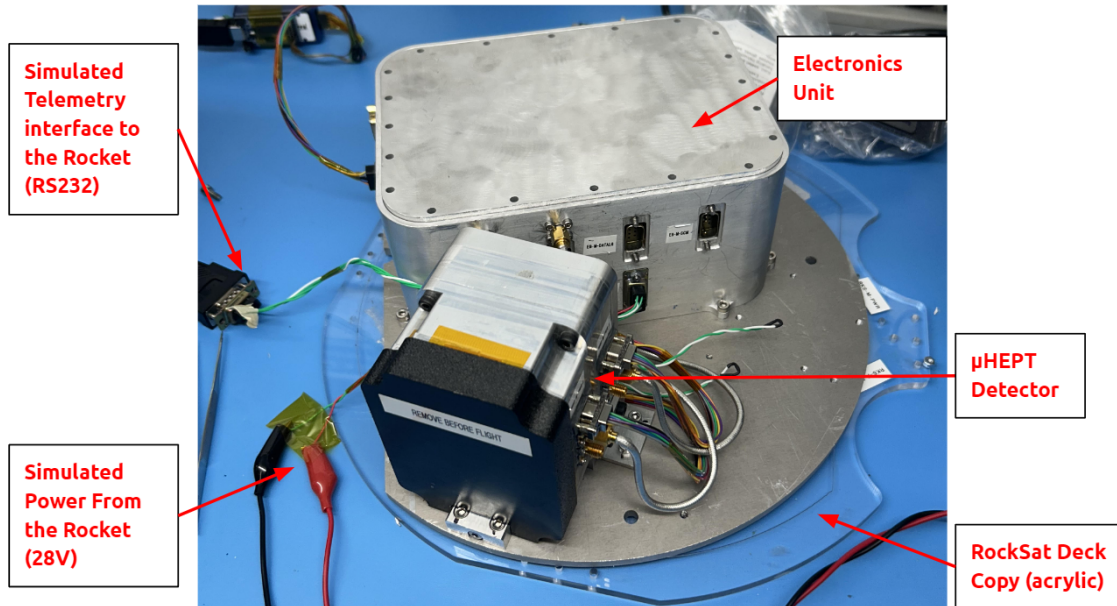


Figure 5.10: Detector and electronics integrated test setup.

5.3.1 Electronics Unit Telemetry Plots

Plots of the temperatures of the three boards (Power Management Board (PMB), Digital Processing Board (DPB), and Detector Interface Board (DIB)) are shown in Figure 5.11. These temperatures are monitored by the instrument, using thermistors that are read-out by an ADC and FPGA, as described in chapter 4. This test was run for a duration of approximately 45 minutes, and it can be seen that the board temperature increases for approximately the first 20 minutes. The temperatures settle to a value of approximately 32 degrees Celsius for the PMB and DPB, and to approximately 26 degrees Celsius for the DIB. Figure 5.12 shows the temperature of the two boards inside the Microburst Detector. These boards show a smaller rise in temperature during the test duration, which can be attributed to thicker copper layers

(2 Oz instead of 1 Oz) as well as the low power dissipation of the MPCC detectors.

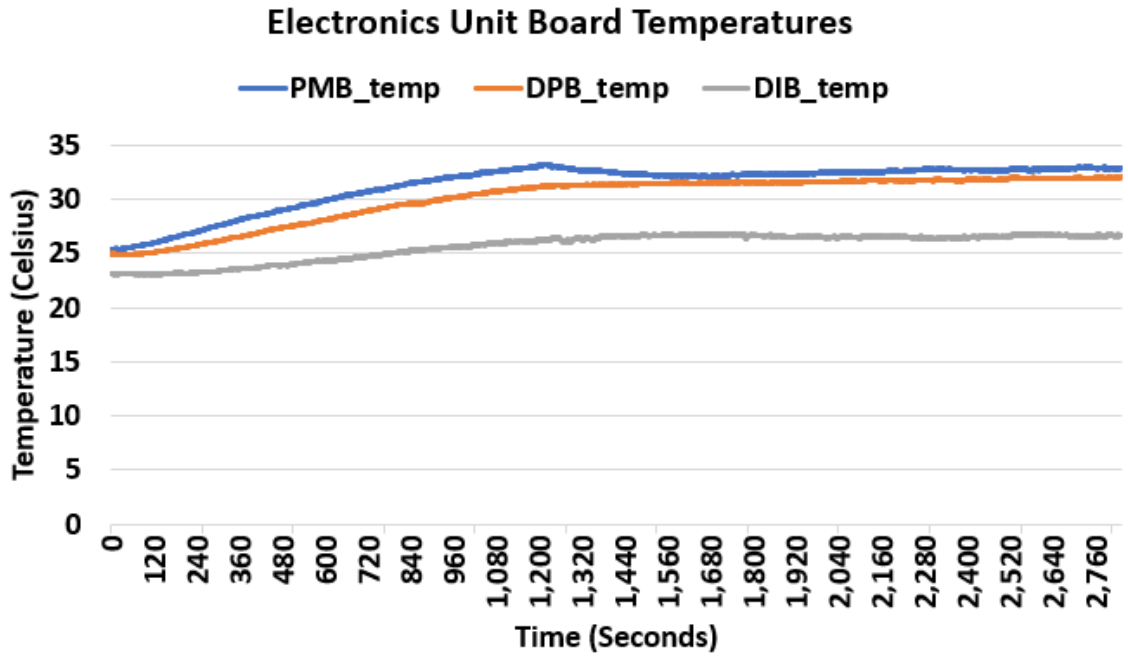


Figure 5.11: Electronics Board Temperatures.

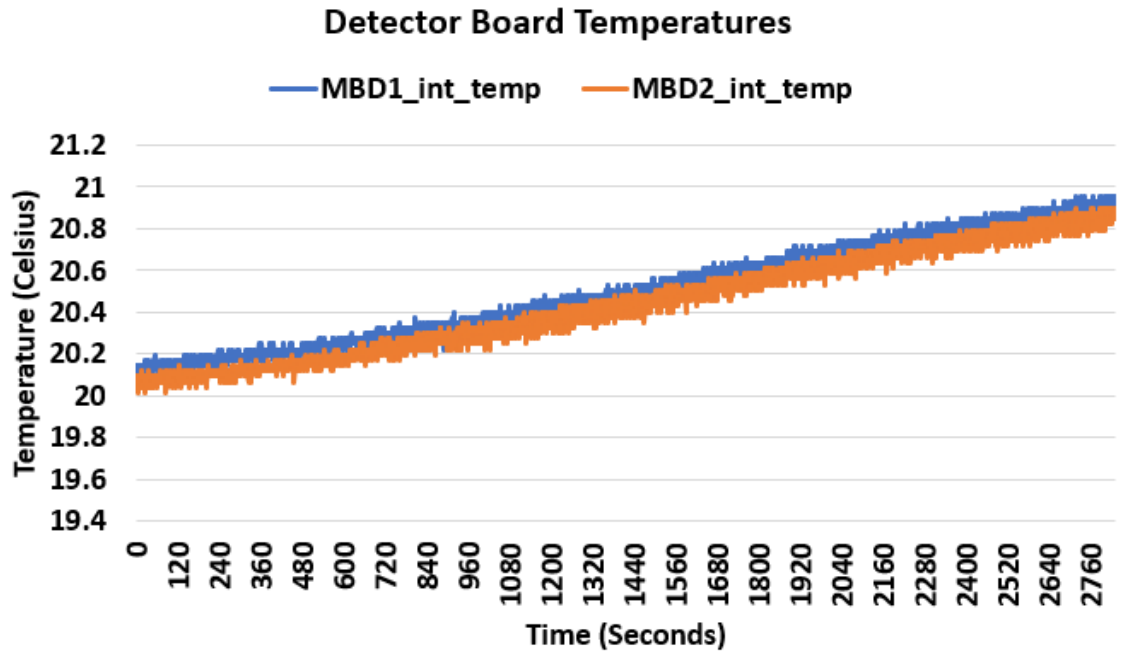


Figure 5.12: Detector Board Temperatures.

Figure 5.13 shows the temperatures of a few electronic components including the

3.3V and 5V DC-DC regulators (labeled Traco3 and Traco5, respectively), the High Voltage regulator (labelled HV_Temp), as well as the SmartFusion2 FPGA (labelled SF2_temp). The plot shows that the DC-DC regulator's temperature rises rapidly and settles to a value of approx. 45 degree Celsius. The high voltage regulators value also rises and settles to a value of approx. 37 degree Celsius. This can be attributed to the efficiency of the regulators, which depends on the output load. Since, the instruments load requirements are low, this leads to higher dissipation. The SmartFusion2 FPGA temperature increases slightly, but remains relatively stable during the test duration.

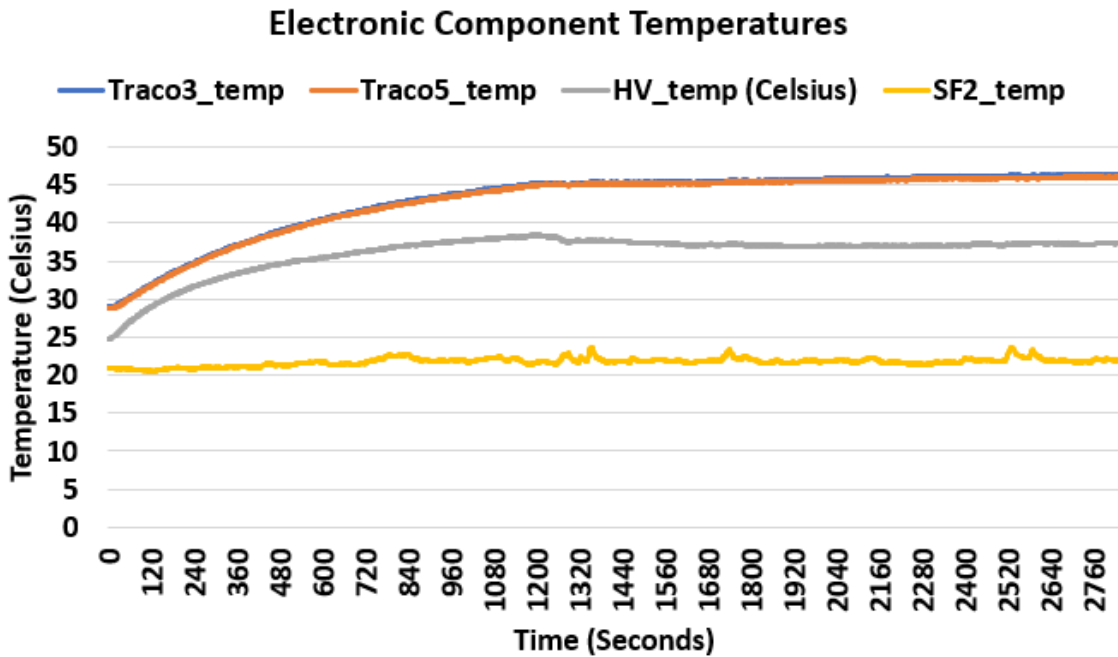


Figure 5.13: Electronics Component Temperatures.

Figure 5.14 shows the high voltage bias applied to the MPPC detectors (labeled hv1_control_v). The value of the regulator is set by the FPGA using a DAC. For monitoring the value set, the FPGA measures it using a resistor divider feedback network (including a Op-Amp and ADC), details of which are described in chapter 4. It was observed that even though the FPGA sets a constant DAC value, the voltage value initially increases. This was attributed to the increase in temperature of the regulator. The High Voltage Regulator temperature (labelled HV_temp) in the same

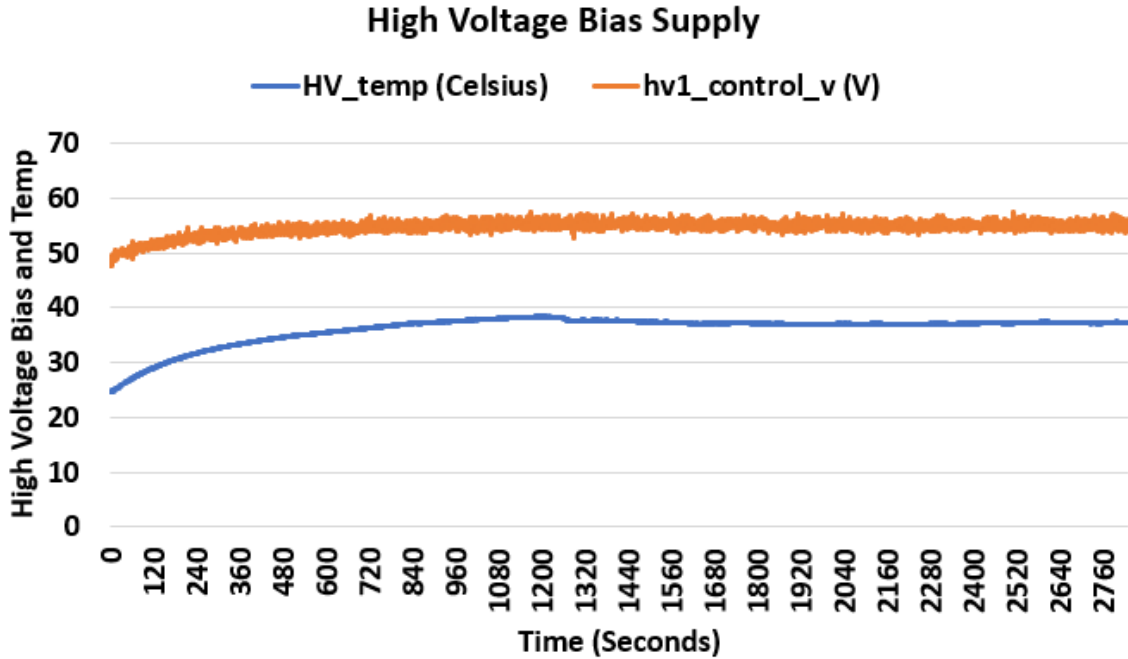


Figure 5.14: High Voltage Bias Supply and high voltage regulator temperature.

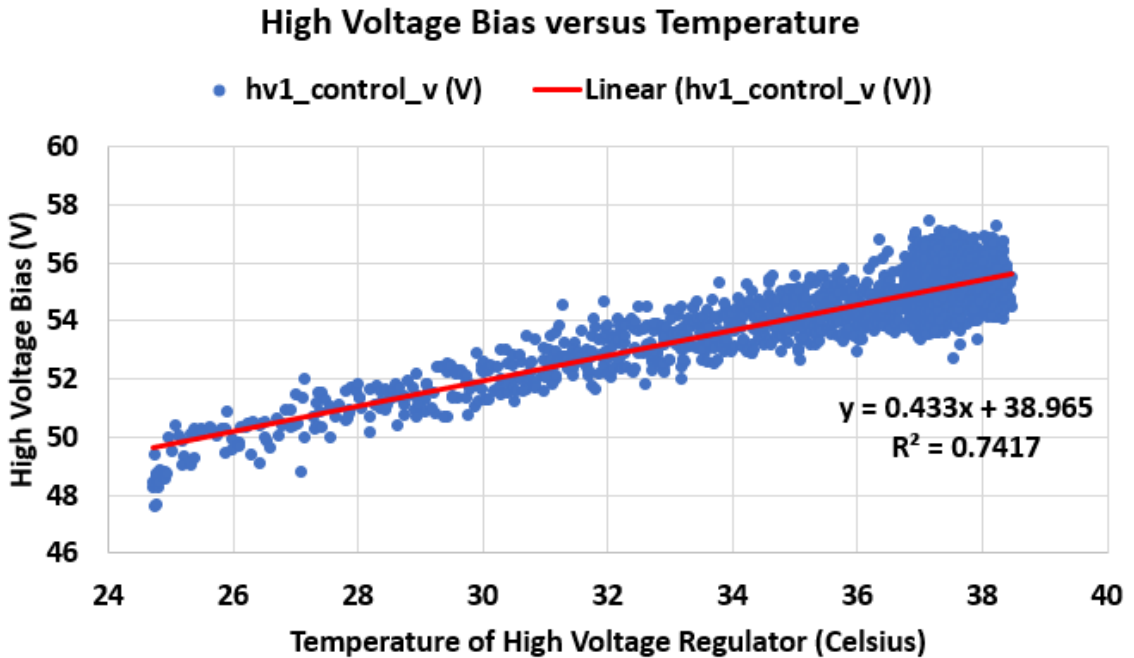


Figure 5.15: Correlation between high voltage bias and regulator temperature.

plot shows this correlation. Additionally, a scatter plot of the High Voltage Bias voltage versus the temperature of the high voltage regulator is shown in figure 5.15.

This plot shows a approximately linear (red line shown in figure) dependence of the high voltage bias to the regulator temperature.

Figures 5.16 and 5.17 show the voltages and currents of the three DC-DC regulators on the power management board. These are measured using the Voltage-Current sensors that are read out by the FPGA as described in Chapter 4. The three voltages are observed to be stable (3.3V, 5V, and 12V) during the test duration. The current drawn in the 3.3V line is 0.212 mA. This leads to a power consumption of approx. 0.7 W, which is the total power draw of the SmartFusion2 FPGA, SD Card, NAND Flash, RS232 converter, Voltage-Current Sensors and housekeeping ADCs. The current draw of the 5V line is 0.112 A, which leads to a power draw of 0.56 W, which is the power consumption of two high-sampling frequency ADC modules used for the detector read-out.

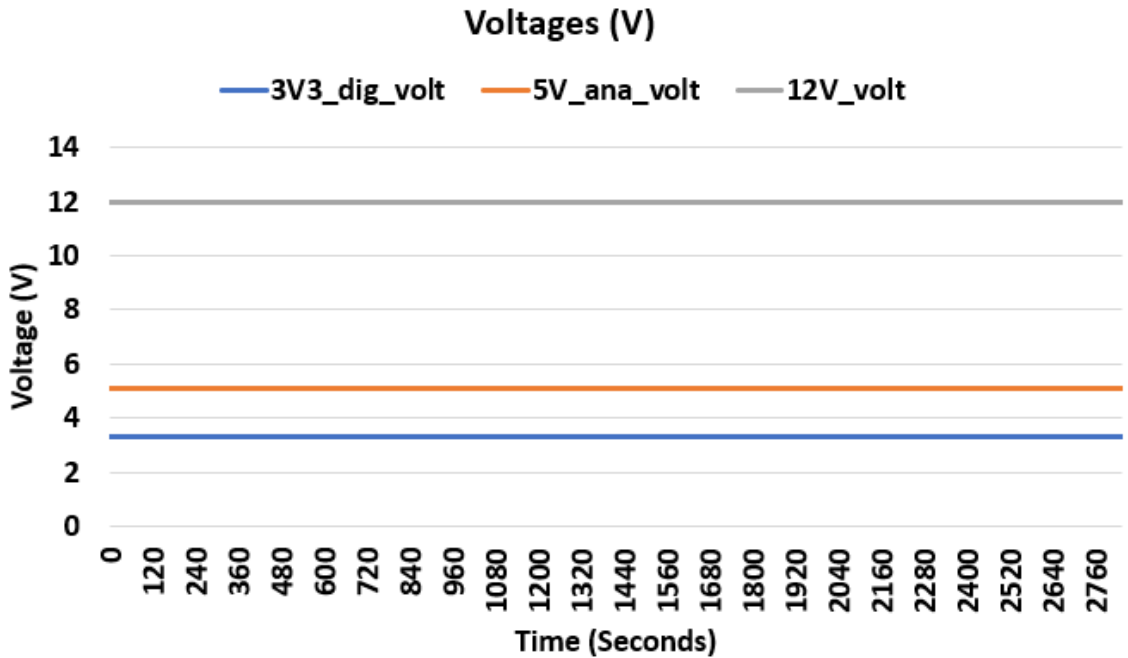


Figure 5.16: DC-DC Regulator Output Voltages.

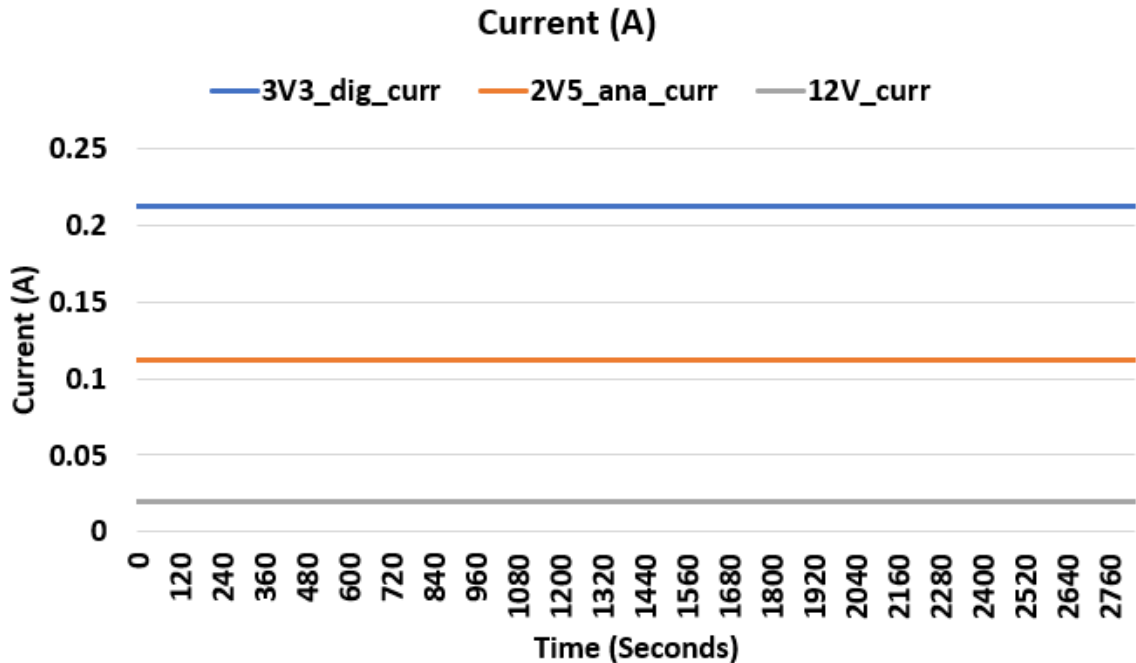


Figure 5.17: DC-DC regulator output currents.

5.4 Environmental Tests

In order to validate the functionality of the instrument in the space environment, vacuum tests and vibration tests were performed on the microburst detector and electronics unit which are summarized below.

5.4.1 Vacuum Tests

Vacuum test of both the detector and electronics was performed in a vacuum chamber. Figure 5.18 (left) shows the detector setup inside the vacuum chamber. The instrument was powered with a 28V supply using a feed-through connectors on the chamber. The RS-232 output of the electronics unit was also taken out of the chamber using the feed through connector. The RS-232 output was connected to a telemetry monitoring console as shown in Figure 5.18 (right). The housekeeping telemetry (voltages, currents and temperatures) as well as the detector output histograms were monitored in during the test. The chamber was de-pressurized to a pressure of 10^{-2} millibar. The instrument showed nominal performance in the vacuum environment.

Additionally, the Aluminium cover of the microburst detector was visually inspected after the test and no damage was observed.

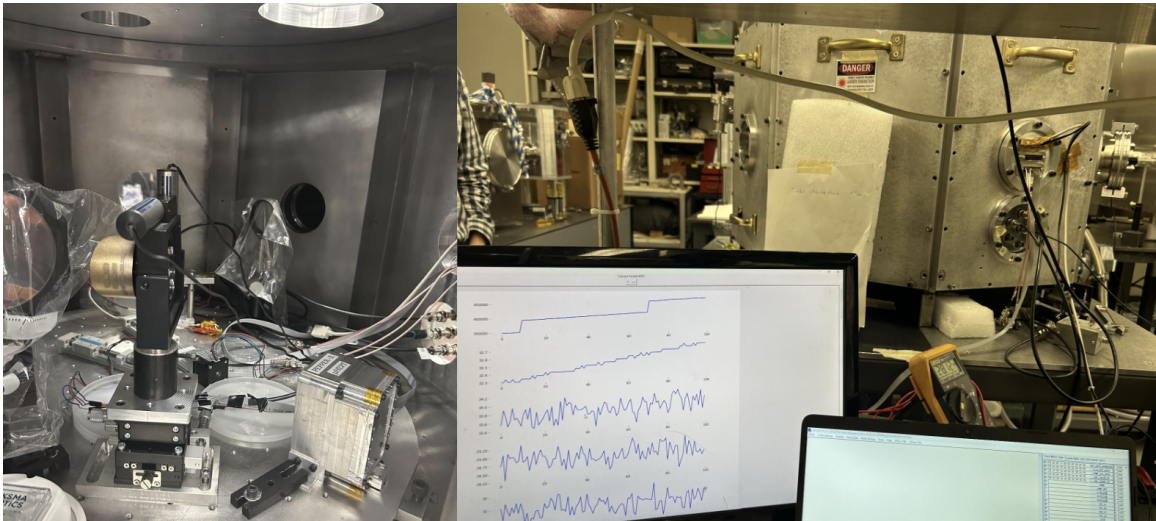


Figure 5.18: Vacuum Tests; Left: Image showing the interior of the chamber with the detector mounted on the bottom plate. Right: Image showing the exterior of the chamber, and telemetry monitoring consoles.

5.4.2 Vibration Tests

In order to validate the mechanical design of the detector and electronics, against the various vibrational loads faced during the launch, two vibration tests were performed. The first test was performed only on the microburst detector and is shown in Figure 5.19 (left). The main objective of the test was to ensure that the mechanical integrity of the MPPC detector and scintillation crystal interface. In this test the detector was subjected to sinusoidal and random vibration in the longitudinal axis (thrust axis of the rocket). Functional checks of the detector were performed after each test, by measuring the leakage current of both the CsI(Na) crystal and the LYSO crystal. The self-scintillation pulses of the LYSO crystal were also recorded after each test. Consistent performance of the detector was observed (no significant change in leakage current) indicating robustness against the vibrational loads. The second vibration test performed was of the integrated detector and electronics unit and is shown in Figure

5.19 (right). This test was performed using the shaker table at the Electronics Test Centre in Airdrie, Alberta. In this test the integrated detector and electronics unit was tested in all three axes. Both sinusoidal sweep and random vibration tests were performed following the levels described in the NASA RockSat-X user guide [44]. The level specified for the sinusoidal test is 7G (rms) from 144 Hz to 2000 Hz. The level for the random vibration test in the thrust axis is 10 G (rms) at 0.051 G_2 /Hz from 20-2000 Hz. The vibration level specified in the lateral axes is 7.6 G (rms) at 0.029 G_2 /Hz from 20-2000 Hz. Functional tests of the integrated detector and electronics were performed after each vibration test, by powering on the instrument using a 28V power supply and monitoring the housekeeping telemetry packets as well as the self-scintillation packets using the RS-232 data interface. Nominal performance of the detector and electronics unit was observed after each vibration test, validating the instrument performance with exposed to simulated launch loads.

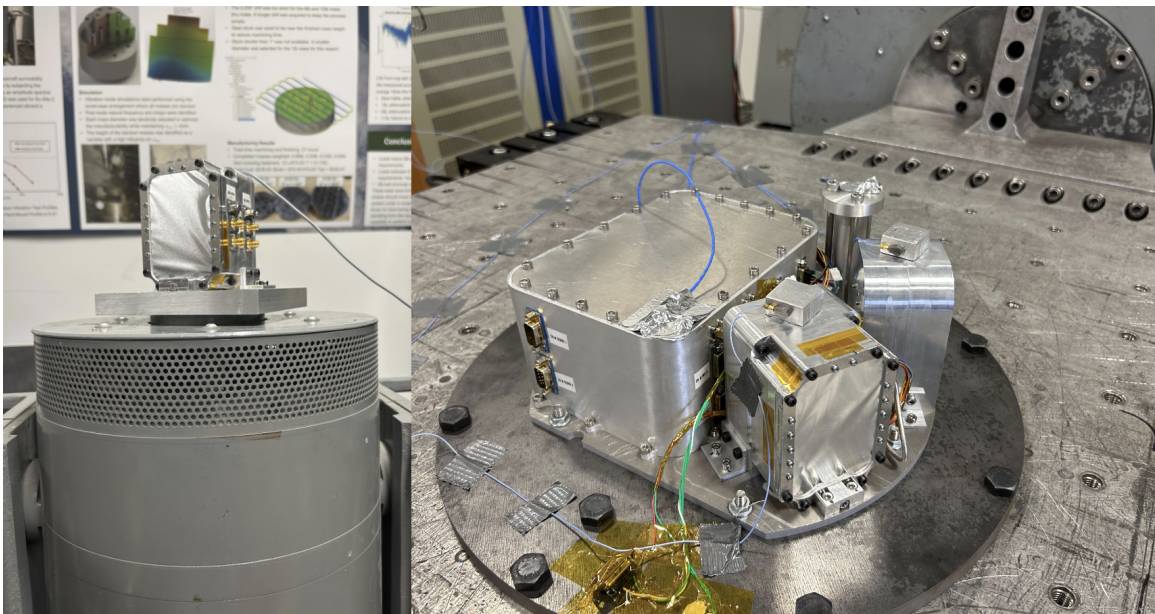


Figure 5.19: Vibration Tests; Left: vibration test of the microburst detector in the longitudinal axis. Right: vibration test of the integrated detector and electronics unit.

5.5 Integrated Instrument Calibration

After assembling the detector and electronics unit, measurements were conducted to find the approximate overall calibration of the instrument using radioisotope sources. First, the lower energy threshold of the instrument was determined. This was done by setting the lower energy cut-off of the binning program and increasing it until no noise pulses were observed. Using this method a lower energy cut-off of 2150 (raw value of the ADC) was set, which corresponds to a voltage of 49.8 mV (Note: the ADC zero voltage value is 2048 counts). With this as the lower threshold, no noise counts were observed in a 10 second measurement interval, which indicates that this threshold of 49.8 mV is several sigma above the baseline RMS noise. Next, the gain of the detector was set to a nominal value of 57 V, as described in the previous section, it was observed that the gain drifts with temperature of the regulator, so the detector was left idle for a duration of approximately 15 minutes for the regulator to reach a relatively steady temperature. At this temperature, two measurements were taken for each source: the first using a peak finding program that stores the value of 2000 peaks which are binned to form a histogram in post-processing; and the second using a histogramming program in which the FPGA bins the pulses into 16 bins. The upper and lower bin threshold (in mV's) are listed in Table 5.2. These are then transferred to the RS232 link (which would be the final link with the rocket telemetry system) every 100 ms. The subsequent sections show the experiment results from the various calibration tests.

5.5.1 LYSO Self-scintillation

Figure 5.20 shows the self scintillation spectrum obtained by measuring and storing 2000 voltage peaks in the FPGA. These are then binned using a finer bin width in post processing. Figure 5.21 shows the histogram of the LYSO self-scintillation spectrum with 16 bins, that are binned and processed in the FPGA. This measurement was

taken over a duration of 192 seconds and a MPPC gain of 57.0 V (average). The expected pulse height distribution is shown in Fig. 5.5 (bottom).

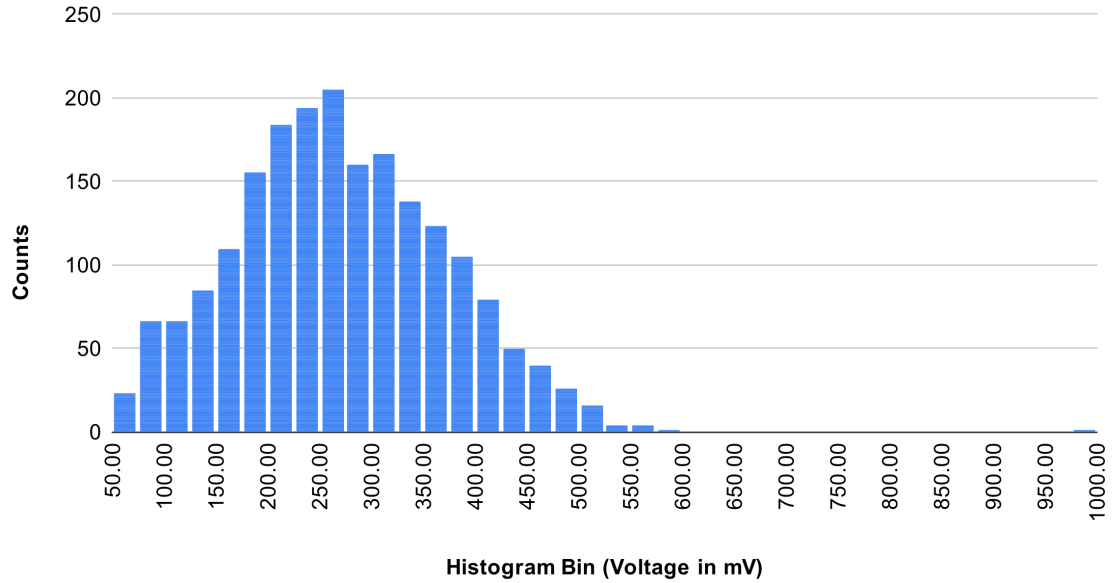


Figure 5.20: LYSO self scintillation spectrum obtained by measuring 2000 peaks

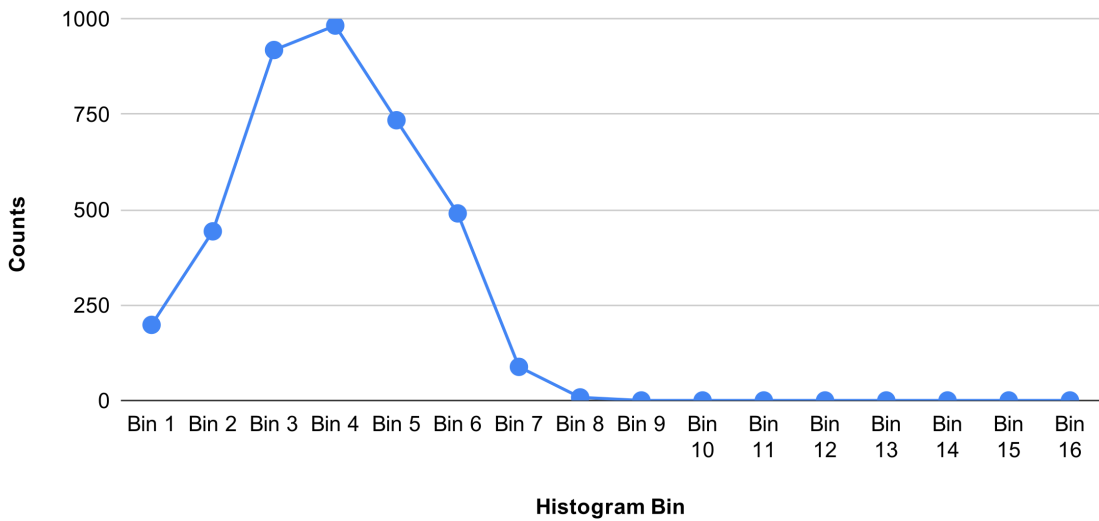


Figure 5.21: LYSO self scintillation spectrum processed and binned into 16 bins by the FPGA

5.5.2 Sr-90 Spectrum

Figure 5.22 shows the Strontium-90 spectrum obtained in the CsI(Na) detector by measuring and storing 2000 voltage peaks in the FPGA. These are then binned using a finer bin width in post processing. Figure 5.23 shows the histogram of the Sr-90 spectrum detected by the CsI(Na) detector with 16 bins, that are binned and processed in the FPGA. This measurement was taken over a duration of 122 seconds and a MPPC gain of 57.7 V (average). The expected pulse height distribution is shown in Fig. 5.7 (bottom).

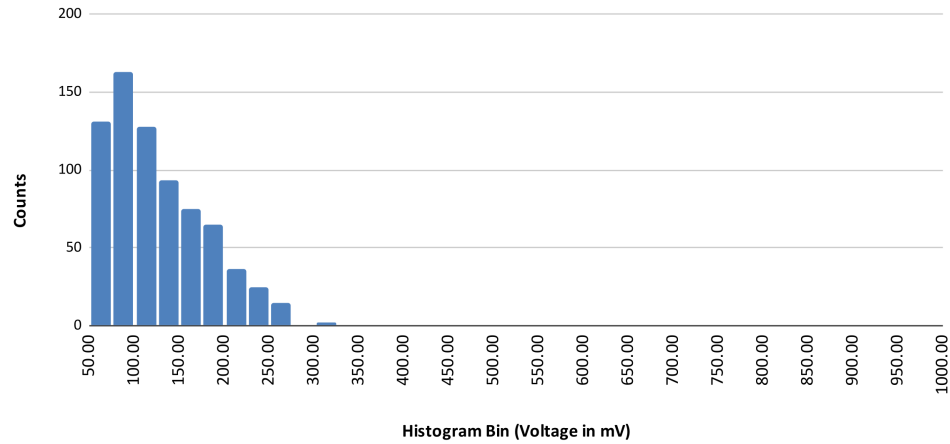


Figure 5.22: Strontium-90 spectrum obtained by measuring 2000 peaks

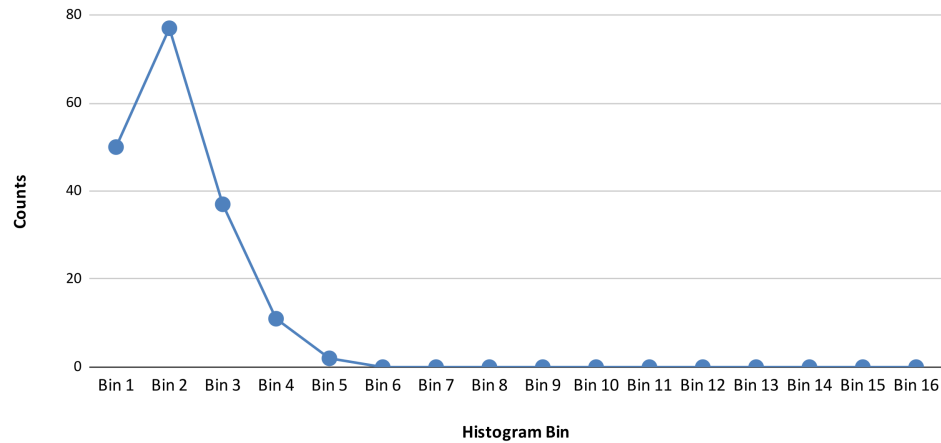


Figure 5.23: Strontium-90 spectrum processed and binned into 16 bins by the FPGA

5.5.3 Ba-133 Spectrum

Figure 5.24 shows the Ba-133 spectrum obtained in the CsI(Na) detector by measuring and storing 2000 voltage peaks in the FPGA. These are then binned using a finer bin width in post processing. Figure 5.25 shows the histogram of the Ba-133 spectrum with 16 bins, that are binned and processed in the FPGA. This measurement was taken over a duration of 144 seconds and a MPPC gain of 57.68 V (average). The expected pulse height distribution for Ba-133 is shown in Fig. 5.6 (bottom).

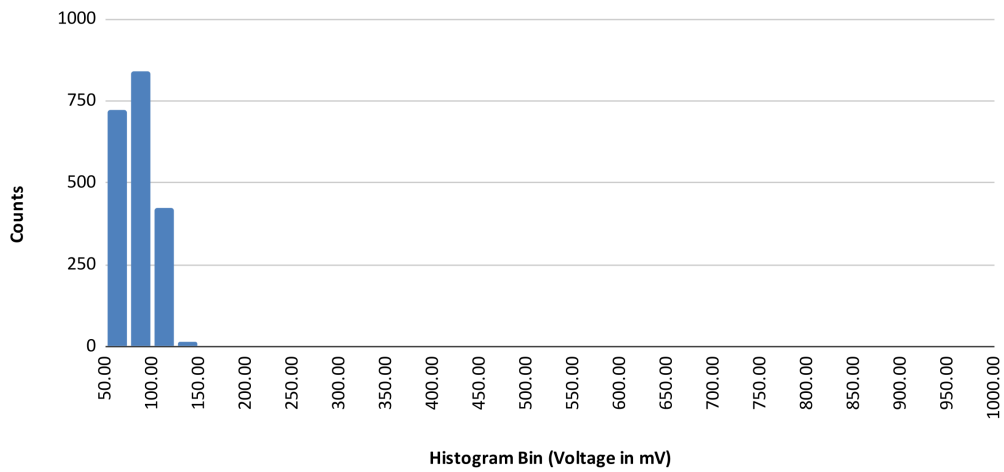


Figure 5.24: Ba-133 spectrum obtained by measuring 2000 peaks

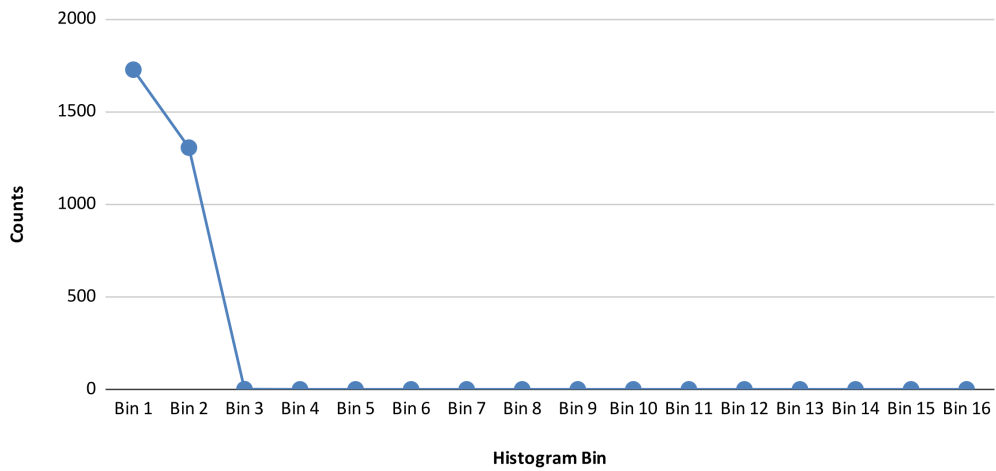


Figure 5.25: Ba-133 spectrum processed and binned into 16 bins by the FPGA

5.6 Discussion and Conclusions

An estimate can be made of the expected detector sensitivities based on the crystal scintillation efficiency, detector quantum efficiency at the scintillation wavelength, light collection efficiency, the output pulsewidth, and the MPPC gain. The estimated parameters and responses for the three crystals used in this study are shown in Table 5.1. The main uncertainty is the efficiency of light collection, which is estimated to be approximately 50 % at present. Based on these estimates, the energy range corresponding to different histograms bins for the CsI(Na) and the LYSO detectors used in the rocket project are shown in Tables 5.2 and 5.3.

	LYSO	BGO	CsI(Na)
ph/MeV	33200	8200	38500
λ_o (nm)	420	480	420
η_Q	0.38	0.4	0.38
F_{coll}	0.5	0.5	0.5
G	4.31×10^6	4.31×10^6	4.31×10^6
$T_{pulse}(ns)$	250	500	100
R (keV/mv)	1.15	8.83	3.96

Table 5.1: Estimated responsivity of the three scintillator crystals. These results are calculated using a approximate gain value corresponding to 57V Bias voltage.

The results of the calibration measurements performed using different radio-isotope sources as described in the previous subsection, are summarized in Table 5.4. Comparison of the different features of the various emission spectra with the theoretically obtained sensitivities, shows relative sensitivities in qualitative agreement with the measurements. However, it is to be noted that these calibration comparisons include a number of assumptions/simplifications. In particular, more detailed comparisons with the expected response would require numerical modelling for an ensemble of electrons, arriving from different angles of incidence and arriving at different posi-

	Lower Threshold		Upper Threshold	
	Voltage (mV)	Energy (keV)	Voltage (mV)	Energy (keV)
Bin 1	49.80	197.23	86.43	342.25
Bin 2	86.43	342.25	147.46	583.95
Bin 3	147.46	583.95	208.50	825.64
Bin 4	208.50	825.64	269.53	1067.34
Bin 5	269.53	1067.34	330.57	1309.04
Bin 6	330.57	1309.04	391.60	1550.74
Bin 7	391.60	1550.74	452.64	1792.44
Bin 8	452.64	1792.44	513.67	2034.14
Bin 9	513.67	2034.14	574.71	2275.84
Bin 10	574.71	2275.84	635.74	2517.54
Bin 11	635.74	2517.54	696.78	2759.24
Bin 12	696.78	2759.24	757.81	3000.94
Bin 13	757.81	3000.94	818.85	3242.64
Bin 14	818.85	3242.64	879.88	3484.34
Bin 15	879.88	3484.34	940.92	3726.04
Bin 16	940.92	3726.04	999.51	3958.07

Table 5.2: Estimated energy ranges of histogram bins of the CsI(Na) crystal

tions in the crystal. These simulations should also account for photon absorption and reflection within the crystal housing. Such simulations are underway using the energetic particle physics code GEANT4, but are beyond the scope of this thesis. Additionally, more detailed measurements can be performed using different sources (such as beamlines) that can be used to provide a known range of electron energies. This would eliminate the error due to the intrinsic spread in the radio-isotope source spectra. Additionally, it is also to be noted that the detector developed for the rocket mission does not have a pre-amplifier and shaper circuit, due to the short development timeline of the mission. An amplifier and shaper circuit will be used in

	Lower Threshold		Upper Threshold	
	Voltage (mV)	Energy (keV)	Voltage (mV)	Energy (keV)
Bin 1	49.80	57.28	86.43	99.39
Bin 2	86.43	99.39	147.46	169.58
Bin 3	147.46	169.58	208.50	239.77
Bin 4	208.50	239.77	269.53	309.96
Bin 5	269.53	309.96	330.57	380.15
Bin 6	330.57	380.15	391.60	450.34
Bin 7	391.60	450.34	452.64	520.53
Bin 8	452.64	520.53	513.67	590.72
Bin 9	513.67	590.72	574.71	660.91
Bin 10	574.71	660.91	635.74	731.10
Bin 11	635.74	731.10	696.78	801.29
Bin 12	696.78	801.29	757.81	871.48
Bin 13	757.81	871.48	818.85	941.67
Bin 14	818.85	941.67	879.88	1011.87
Bin 15	879.88	1011.87	940.92	1082.06
Bin 16	940.92	1082.06	999.51	1149.44

Table 5.3: Estimated energy ranges of histogram bins of the LYSO crystal

Table 5.4: Radioisotope Source Calibration results

Source (Feature)	Energy (keV)	CsI(Na) Output	Bin No.	LYSO Output
Sr-90 (max)	2200	350 mV	7	NA
Barium (peak)	330	75 mV	1	NA
LYSO Self (peak)	300	NA	3	200 mV

the RADICALS mission, which will further increase the signal to noise ratio of the instrument.

In conclusion, in this chapter the various tests performed on the detector and

electronics unit developed for the sounding rocket test flight were described. The calibration of the detector was performed using different radioisotope sources. The electronics unit was tested using different artificially generated analog signals and the digitization functionality verified. Tests were performed on the integrated system comprising both the detector and electronics, which included radioisotope calibration tests. Environmental tests were also performed on the instrument, which included vacuum tests and vibration tests.

The flight models of the detector and electronics unit for the microburst detector to be used on the sounding rocket test flight were developed and tested to ensure that all functional requirements were satisfied. The front CsI (Na) detector will be able to detect electrons in the approximate energy range of 200 keV to 3.5 MeV with a count rate of up to 200,000 kcps. The inner LYSO detector would be able to detect electrons in the energy range of 50 keV to 1.2 MeV. However, as described in chapter 3, for the sounding rocket application, the LYSO crystal is shielded behind the first detector and will not see electrons. Instead, the LYSO crystal will observe its own self-emissions (as well as background Xrays that can penetrate the inner board) and will act as a validity check that the overall detector system is working.

Detectors having a combination of a silicon photomultiplier (or multi-pixel photon counter (MPPC)) with a scintillator crystal, have previously been used in CubeSat missions for Gamma-ray spectroscopy [30, 31]. For example, the performance of one such detector is described in reference [45], which used two large CsI(Tl) crystals ($150 \times 75 \times 5 \text{ mm}^3$ and $100 \times 75 \times 5 \text{ mm}^3$) using a single MPPC as well as two-MPPC readout. For this detector geometry the authors report an lower energy threshold of 10 keV (which satisfies their science requirement of measuring Gamma-ray bursts from 10keV to 300 keV). In comparison, the CsI(Na) detector designed in this thesis, has an energy range of 200 keV to 3.5 MeV, which satisfies the scientific energy range requirement for measuring electron microbursts. Also, in previous studies (for example references [30, 45]) the detectors were calibrated with X-ray radio-isotope

sources such as Am-241 and Cd-109. In this thesis, we have validated the design using an X-ray radio-isotope source (Ba-133) as well as a electron (beta decay) radio-isotope source (Sr-90). Thus, in this thesis we have extended this detection methodology (consisting of a MPPC coupled to a scintillator crystal) for in-situ measurement of energetic electrons in space and demonstrated this functionality using an electron (beta decay) radio-isotope source.

Chapter 6

Summary, Conclusions, and Future Work

6.1 Summary and Conclusions

Over the course of this thesis the design of two components of the RADHEPT Instrument have been significantly advanced: (a) the microburst detector and (b) the instrument electronics. A prototype of the microburst detector was developed and calibration of the detector using radio-isotope sources was performed to verify the performance. For the electronics development, a system-level architecture was developed and a prototype electronics unit was realized. An alternative list of rad-hard components were also identified that can be used for the RADICALS mission. A version of the microburst detector and electronics was designed, built and tested for an upcoming flight on a NASA RockSat-X sounding rocket mission[44] in August 2024.

Figure 6.1 shows the evolution of the instrument development as presented at periodic NASA design reviews conducted for the sounding rocket mission. The first row shows the detector and electronics unit prototypes as presented in the Conceptual Design Review (CoDR) in August 2023, and the last row shows the completed flight models presented at the Full Mission Simulation Review (FMSR) in May 2024. In preparation for the RockSat-X sounding rocket flight, extensive testing was performed on the microburst detector and instrument electronics, including vacuum tests and vibration tests.



Figure 6.1: Design evolution of the Microburst Detector (right) and Electronics Unit (left) from breadboard prototypes (first row) to flight models (last row).

6.1.1 Instrument Scientific Performance

Table 6.1 shows the performance of the detector prototype developed in this thesis as compared to the current state-of-the-art microburst measurements as explained in Chapter 2. As can be seen from the table, for most performance metrics, the detector designed is superior to the current state-of-the-art microburst measurements.

Table 6.1: Previous microburst measurement parameters and proposed goals for the RADICALS micoburst detector (SSD = Solid State Detector, SiPM = Silicon Photomultiplier)

Parameter	Previous Measurement Made		Proposed Goal
Mission	FIREBIRDII [23]	SAMPEX-HILT [26]	RADICALS
Detection Technique	SSD	SSD+Photodiodes	Scintillator+SiPM
Energy Range	0.2 to 1 MeV, > 1 MeV	> 1 MeV	0.2 to 3.5 MeV
Energy Res.	5 channels	N/A	16 channels
Time Res.	18.75 ms	20 ms	10 ms
Field of View	180 (and 45) deg	60 deg	180 deg

To verify that the designed detector for the RADICALS mission will be suitable for resolving microbursts, estimates of maximum flux over different energy ranges are being studied as a part of the RADICALS RADHEPT Instrument Performance Requirements document (Credit: Louis Ozeke, Department of Physics). Based on analysis of previous mission data completed so far, the maximum >0.2 MeV integral flux was estimated as 3×10^6 cm²/s/sr (top 0.001 % trapped flux from the POES satellite mission). Additionally, the maximum >1 MeV integral flux was estimated as 1×10^4 cm²/s/sr (based on measurement from the SAMPEX HILT mission data). Figure 6.2 shows the estimated integral flux above different energy thresholds as estimated from previous mission data.

Based on the current estimates of the detector designed for the sounding rocket test flight, the CsI(Na) crystal will be able to measure microbursts with an energy range of

200 keV to 3.5 MeV, having maximum integral flux of 10^5 counts/cm²/str/sec using a FPGA that can handle a maximum of 200,000 counts/second. This is greater than the 75 percentile for trapped and 99.9 percentile for the expected precipitating flux as shown in figure 6.2. It is to be noted that further design improvements are possible in the detector performance, including the maximum measurable flux as well as a smaller lower energy threshold. A few possible ideas to achieve these are described as a part of the future work in the next section.

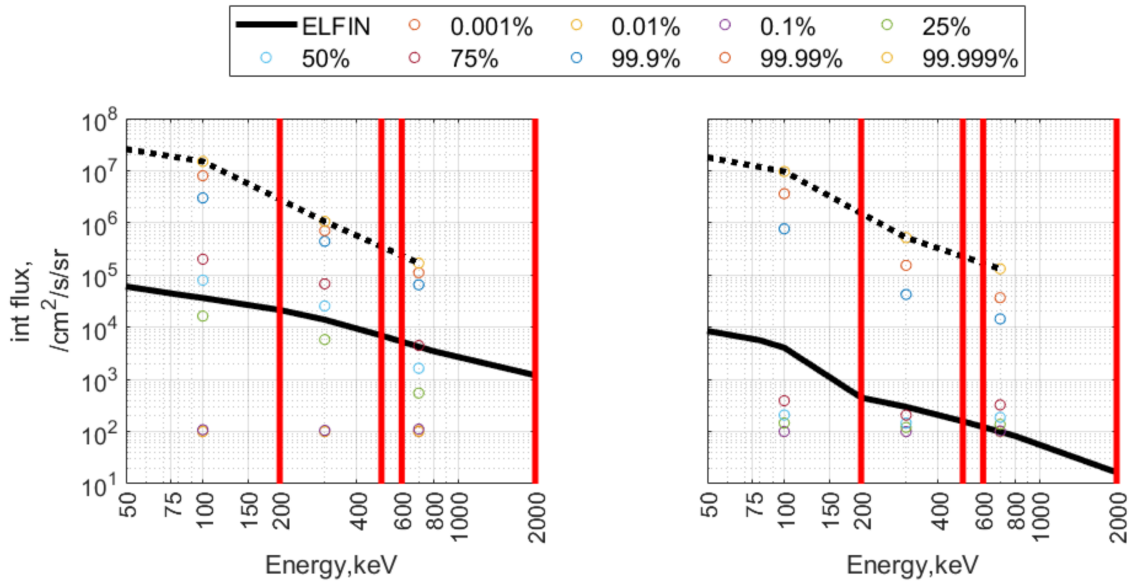


Figure 6.2: Maximum integral flux above a given energy from previous mission data. The figure shows comparison between the ELFIN flux between L=4.5 and 5 with the trapped (left) and precipitating flux (right) percentiles detected by POES over the same L-shell range. The circles indicate the percentiles derived from the POES 90 degree and 0 degree detectors between L=4.5 and 5. The vertical red lines indicate different energy thresholds (>0.2 MeV, >0.5 MeV, >0.6 MeV and >2 MeV). Figure Credit: RADHEPT Measurement requirements document, Louis Ozeke, Department of Physics

6.2 Future Work

Listed below are a number of areas of future work for the microburst detector, as well as the overall instrument electronics that are to be completed in advance of the RADICALS microsatellite mission.

- **Microburst Detector Future Work**

1. **GEANT-4 Simulation and Validation:** Experimental calibration of the detector was completed in this thesis to validate its performance. In order to get a more accurate estimate of the detector geometric factor and its performance for electrons arriving at different angles of incidence, detailed Monte-Carlo GEANT4 simulations of the detector performance must be completed.
2. **Detector Geometry Optimization:** In order to control the geometric factor of the detector, a design development could be considered that uses an enclosure with holes on the surface, within which the crystal is housed. Such a design would reduce the overall flux reaching the microburst detector and could prevent the instrument from saturating as a result of the high count rates of low energy electrons by reducing the geometric factor. Additionally, a rectangular light guide could be added between the MPPC and crystal to protect the MPPC from incoming radiation and give more thermal shielding. It is known that MPPC's are sensitive to degradation when exposed to krads of radiation (for example, reference [46]), and thus shielding should be considered for longer lifetime missions. It is also known that the MPPC gain is a function of temperature and thus more thermal insulation from the glass light guide would help reduce the temperature fluctuations seen by the MPPC detector. More calculations, experiments, and simulations would be required to validate this design.
3. **Using a Combination of Two Crystals:** To achieve a wider energy range a combination of two crystal scintillators could be used. The first crystal would be larger (approximate geometric factor of $10 \text{ cm}^2 \text{ str}$) and shielded against low energy electrons, in order to measure high energy (0.8 to 4 MeV) electrons. The second crystal would be smaller (approximate

geometric factor of $1 \text{ cm}^2 \text{ str}$), in order to measure lower energy electrons (200 keV to 0.8 MeV). The output from these two crystals could also be added together using summing amplifiers, with one crystal generating positive pulses and the other generating negative signals, such that it could be possible to resolve and to read out each crystal response simultaneously with the same electronics. For example, by using the bidirectional ADCs as employed here, and which are proposed for RADHEPT, the positive and negative pulses can be counted and binned separately. Figure 6.3 shows a conceptual block diagram showing the signal flow of such a detector using two crystals.

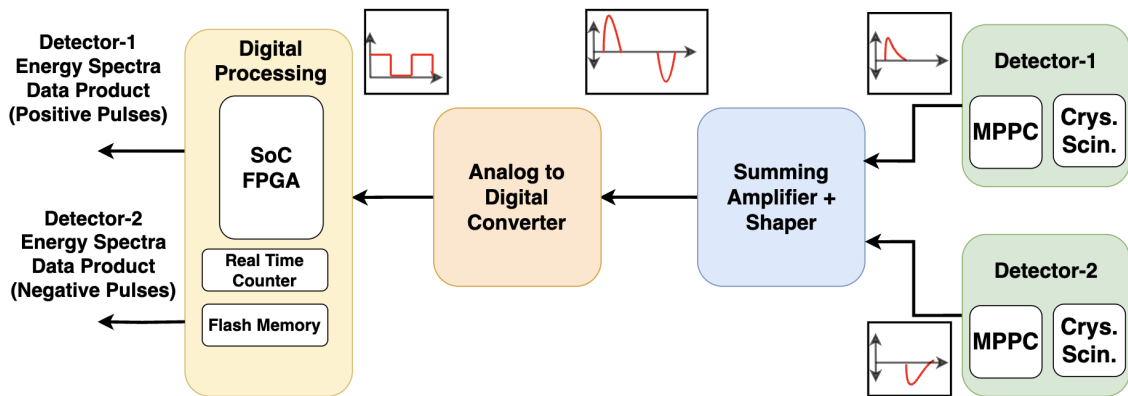


Figure 6.3: Block diagram showing the conceptual design of an instrument using two crystals and adopting a bi-directional pulse approach for simultaneous readout of both crystals using the same electronics.

• RADHEPT Electronics Future Work

1. **Realization of rad-tolerant version of the instrument:** In Chapter 4, two sets of components for the detector electron were identified, one using commercial-of-the-shelf components and other with rad-hard components. In this thesis, a prototype of the electronics using commercial-of-the-shelf components was developed to test the overall design for the mission. A prototype using the rad-tolerant version must be tested and realized as a

next step for the RADICALS mission.

2. **Environmental Testing of the Instrument:** During this thesis, vacuum tests and vibration tests were performed on both the detector and the electronics developed for the sounding rocket test flight. In order to qualify the instrument for flight on the RADICALS mission, additional thermal-vacuum testing, electromagnetic interference (EMI), and electromagnetic compatibility (EMC) testing of the electronics must all be completed.

In conclusion, a novel approach to measuring electron microbursts on a satellite mission using scintillators coupled to Silicon photomultiplier detectors was proposed and demonstrated. A complete detector system with FPGA electronics signal processing was developed and characterized. It was demonstrated that this new approach had adequate sensitivity to cover the required electron energy detection range and was also capable of operating at the required high count rates upto 200 Kcps. Overall, the work described in this thesis thus paves the way for flying such detectors on future CubeSat and small satellite missions.

The instrumentation developed during this thesis will enable high-fidelity in-situ energetic electron measurements to be made from a variety of space-based platforms, that in-turn will lead to improvements in our understanding of energetic electron precipitation and radiation belt dynamics in the near-Earth space.

Bibliography

- [1] N. Y. Ganushkina, I. Dandouras, Y. Y. Shprits, and J. Cao, “Locations of boundaries of outer and inner radiation belts as observed by cluster and double star,” *Journal of Geophysical Research: Space Physics*, vol. 116, A9 2011, eprint: <https://onlinelibrary.wiley.com/doi/pdf/10.1029/2010JA016376>, ISSN: 2156-2202. DOI: 10.1029/2010JA016376. [Online]. Available: <https://onlinelibrary.wiley.com/doi/abs/10.1029/2010JA016376> (visited on 11/29/2023).
- [2] S. Kanekal, D. Baker, and D. Sibeck, “Recent advances in our understanding of the earth’s radiation belts,” in *2019 International Conference on Electromagnetics in Advanced Applications (ICEAA)*, Granada, Spain: IEEE, Sep. 2019, pp. 1345–1348, ISBN: 978-1-72810-563-5. DOI: 10.1109/ICEAA.2019.8879310. [Online]. Available: <https://ieeexplore.ieee.org/document/8879310/> (visited on 04/15/2024).
- [3] R. Vainio *et al.*, “Dynamics of the earth’s particle radiation environment,” *Space Science Reviews*, vol. 147, no. 3, pp. 187–231, Nov. 1, 2009, ISSN: 1572-9672. DOI: 10.1007/s11214-009-9496-7. [Online]. Available: <https://doi.org/10.1007/s11214-009-9496-7> (visited on 04/15/2024).
- [4] J. A. Van Allen, G. H. Ludwig, E. C. Ray, and C. E. McILWAIN, “Observation of high intensity radiation by satellites 1958 alpha and gamma,” *Journal of Jet Propulsion*, vol. 28, no. 9, pp. 588–592, Sep. 1958, Publisher: American Institute of Aeronautics and Astronautics. DOI: 10.2514/8.7396. [Online]. Available: <https://arc.aiaa.org/doi/10.2514/8.7396> (visited on 04/18/2024).
- [5] R. A. Marshall and C. M. Cully, “Chapter 7 - Atmospheric effects and signatures of high-energy electron precipitation,” in *The Dynamic Loss of Earth’s Radiation Belts*, A. N. Jaynes and M. E. Usanova, Eds., Elsevier, Jan. 1, 2020, pp. 199–255, ISBN: 978-0-12-813371-2. DOI: 10.1016/B978-0-12-813371-2.00007-X. [Online]. Available: <https://www.sciencedirect.com/science/article/pii/B978012813371200007X> (visited on 08/23/2023).
- [6] J. C. Chancellor, G. B. I. Scott, and J. P. Sutton, “Space radiation: The number one risk to astronaut health beyond low Earth orbit,” *Life : Open Access Journal*, vol. 4, no. 3, pp. 491–510, Sep. 11, 2014, ISSN: 2075-1729. DOI: 10.3390/life4030491. [Online]. Available: <https://www.ncbi.nlm.nih.gov/pmc/articles/PMC4206856/> (visited on 11/21/2023).

- [7] T. P. O'Brien, M. D. Looper, and J. B. Blake, "Quantification of relativistic electron microburst losses during the GEM storms," *Geophysical Research Letters*, vol. 31, no. 4, 2004, eprint: <https://onlinelibrary.wiley.com/doi/pdf/10.1029/2003GL018621>, ISSN: 1944-8007. DOI: 10.1029/2003GL018621. [Online]. Available: <https://onlinelibrary.wiley.com/doi/abs/10.1029/2003GL018621> (visited on 11/21/2023).
- [8] R. M. Millan and R. M. Thorne, "Review of radiation belt relativistic electron losses," *Journal of Atmospheric and Solar-Terrestrial Physics*, Global Aspects of Magnetosphere-Ionosphere Coupling, vol. 69, no. 3, pp. 362–377, Mar. 1, 2007, ISSN: 1364-6826. DOI: 10.1016/j.jastp.2006.06.019. [Online]. Available: <https://www.sciencedirect.com/science/article/pii/S1364682606002768> (visited on 11/27/2023).
- [9] A. Seppälä, E. Douma, C. J. Rodger, P. T. Verronen, M. A. Clilverd, and J. Bortnik, "Relativistic electron microburst events: Modeling the atmospheric impact," *Geophysical Research Letters*, vol. 45, no. 2, pp. 1141–1147, 2018, eprint: <https://onlinelibrary.wiley.com/doi/pdf/10.1002/2017GL075949>, ISSN: 1944-8007. DOI: 10.1002/2017GL075949. [Online]. Available: <https://onlinelibrary.wiley.com/doi/abs/10.1002/2017GL075949> (visited on 10/09/2023).
- [10] P. Arsenovic *et al.*, "The influence of middle range energy electrons on atmospheric chemistry and regional climate," *Journal of Atmospheric and Solar-Terrestrial Physics*, vol. 149, pp. 180–190, 2016, ISSN: 1364-6826. DOI: <https://doi.org/10.1016/j.jastp.2016.04.008>. [Online]. Available: <https://www.sciencedirect.com/science/article/pii/S1364682616301080>.
- [11] M. E. Andersson, P. T. Verronen, C. J. Rodger, M. A. Clilverd, and A. Seppälä, "Missing driver in the sun–earth connection from energetic electron precipitation impacts mesospheric ozone," *Nature Communications*, vol. 5, no. 1, p. 5197, Oct. 14, 2014, Publisher: Nature Publishing Group, ISSN: 2041-1723. DOI: 10.1038/ncomms6197. [Online]. Available: <https://www.nature.com/articles/ncomms6197> (visited on 06/28/2024).
- [12] S. S. Elliott *et al.*, "Understanding the properties, wave drivers, and impacts of electron microburst precipitation: Current understanding and critical knowledge gaps," *Frontiers in Astronomy and Space Sciences*, vol. 9, 2022, ISSN: 2296-987X. [Online]. Available: <https://www.frontiersin.org/articles/10.3389/fspas.2022.1062422> (visited on 10/11/2023).
- [13] R. S. Selesnick *et al.*, "Observations of the inner radiation belt: CRAND and trapped solar protons," *Journal of Geophysical Research: Space Physics*, vol. 119, no. 8, pp. 6541–6552, 2014, eprint: <https://onlinelibrary.wiley.com/doi/pdf/10.1002/2014JA020188>, ISSN: 2169-9402. DOI: 10.1002/2014JA020188. [Online]. Available: <https://onlinelibrary.wiley.com/doi/abs/10.1002/2014JA020188> (visited on 12/12/2023).

- [14] J. F. Fennell *et al.*, “Van Allen Probes show that the inner radiation zone contains no MeV electrons: ECT/MagEIS data,” *Geophysical Research Letters*, vol. 42, no. 5, pp. 1283–1289, 2015, eprint: <https://onlinelibrary.wiley.com/doi/pdf/10.1002/2014GL062874>, ISSN: 1944-8007. DOI: 10.1002/2014GL062874. [Online]. Available: <https://onlinelibrary.wiley.com/doi/abs/10.1002/2014GL062874> (visited on 12/12/2023).
- [15] M. Walt, *Introduction to Geomagnetically Trapped Radiation* (Cambridge Atmospheric and Space Science Series). Cambridge: Cambridge University Press, 1994, ISBN: 978-0-521-61611-9. DOI: 10.1017/CBO9780511524981. [Online]. Available: <https://www.cambridge.org/core/books/introduction-to-geomagnetically-trapped-radiation/10A3D5EEB3B535BED6D1E2133DAC67B9> (visited on 12/12/2023).
- [16] W. Tu, Z. Xiang, and S. K. Morley, “Modeling the magnetopause shadowing loss during the june 2015 dropout event,” *Geophysical Research Letters*, vol. 46, no. 16, pp. 9388–9396, 2019, ISSN: 1944-8007. DOI: 10.1029/2019GL084419. [Online]. Available: <https://onlinelibrary.wiley.com/doi/abs/10.1029/2019GL084419> (visited on 12/24/2023).
- [17] L. Blum, X. Li, and M. Denton, “Rapid MeV electron precipitation as observed by SAMPEX/HILT during high-speed stream-driven storms,” *Journal of Geophysical Research: Space Physics*, vol. 120, no. 5, pp. 3783–3794, 2015, ISSN: 2169-9402. DOI: 10.1002/2014JA020633. [Online]. Available: <https://onlinelibrary.wiley.com/doi/abs/10.1002/2014JA020633> (visited on 12/24/2023).
- [18] C. F. Kennel and H. E. Petschek, “Limit on stably trapped particle fluxes,” *Journal of Geophysical Research (1896-1977)*, vol. 71, no. 1, pp. 1–28, 1966, ISSN: 2156-2202. DOI: 10.1029/JZ071i001p00001. [Online]. Available: <https://onlinelibrary.wiley.com/doi/abs/10.1029/JZ071i001p00001> (visited on 12/24/2023).
- [19] C. Colpitts *et al.*, “First direct observations of propagation of discrete chorus elements from the equatorial source to higher latitudes, using the Van Allen Probes and Arase satellites,” *Journal of Geophysical Research: Space Physics*, vol. 125, no. 10, e2020JA028315, 2020, ISSN: 2169-9402. DOI: 10.1029/2020JA028315. [Online]. Available: <https://onlinelibrary.wiley.com/doi/abs/10.1029/2020JA028315> (visited on 03/06/2024).
- [20] A. W. Breneman *et al.*, “Observations directly linking relativistic electron microbursts to whistler mode chorus: Van Allen Probes and FIREBIRD II,” *Geophysical Research Letters*, vol. 44, no. 22, pp. 11,265–11,272, 2017, eprint: <https://onlinelibrary.wiley.com/doi/pdf/10.1002/2017GL075001>, ISSN: 1944-8007. DOI: 10.1002/2017GL075001. [Online]. Available: <https://onlinelibrary.wiley.com/doi/abs/10.1002/2017GL075001> (visited on 03/06/2024).

- [21] M. Shumko *et al.*, “Proton aurora and relativistic electron microbursts scattered by electromagnetic ion cyclotron waves,” *Frontiers in Astronomy and Space Sciences*, vol. 9, 2022, ISSN: 2296-987X. [Online]. Available: <https://www.frontiersin.org/articles/10.3389/fspas.2022.975123> (visited on 12/24/2023).
- [22] H. E. Spence *et al.*, “Science goals and overview of the radiation belt storm probes (RBSP) energetic particle, composition, and thermal plasma (ECT) suite on NASA’s Van Allen Probes mission,” *Space Science Reviews*, vol. 179, no. 1, pp. 311–336, Nov. 1, 2013, ISSN: 1572-9672. DOI: 10.1007/s11214-013-0007-5. [Online]. Available: <https://doi.org/10.1007/s11214-013-0007-5> (visited on 12/25/2023).
- [23] A. B. Crew *et al.*, “First multipoint in situ observations of electron microbursts: Initial results from the NSF FIREBIRD II mission,” *Journal of Geophysical Research: Space Physics*, vol. 121, no. 6, pp. 5272–5283, 2016, ISSN: 2169-9402. DOI: 10.1002/2016JA022485. [Online]. Available: <https://onlinelibrary.wiley.com/doi/abs/10.1002/2016JA022485> (visited on 08/23/2023).
- [24] M. Shumko *et al.*, “Electron microburst size distribution derived with AeroCube-6,” *Journal of Geophysical Research: Space Physics*, vol. 125, no. 3, e2019JA027651, 2020, eprint: <https://onlinelibrary.wiley.com/doi/pdf/10.1029/2019JA027651>, ISSN: 2169-9402. DOI: 10.1029/2019JA027651. [Online]. Available: <https://onlinelibrary.wiley.com/doi/abs/10.1029/2019JA027651> (visited on 12/25/2023).
- [25] D. Mourenas, A. V. Artemyev, X. J. Zhang, V. Angelopoulos, E. Tsai, and C. Wilkins, “Electron lifetimes and diffusion rates inferred from ELFIN measurements at low altitude: First results,” *Journal of Geophysical Research: Space Physics*, vol. 126, no. 11, e2021JA029757, 2021, eprint: <https://onlinelibrary.wiley.com/doi/pdf/10.1029/2021JA029757>, ISSN: 2169-9402. DOI: 10.1029/2021JA029757. [Online]. Available: <https://onlinelibrary.wiley.com/doi/abs/10.1029/2021JA029757> (visited on 08/23/2023).
- [26] C. Meyer-Reed, L. Blum, and M. Shumko, “Pitch angle isotropy of relativistic electron microbursts as observed by SAMPEX/HILT: Statistical and storm-time properties,” *Journal of Geophysical Research: Space Physics*, vol. 128, no. 1, e2022JA030926, 2023, ISSN: 2169-9402. DOI: 10.1029/2022JA030926. [Online]. Available: <https://onlinelibrary.wiley.com/doi/abs/10.1029/2022JA030926> (visited on 08/23/2023).
- [27] K. A. Anderson and D. W. Milton, “Balloon observations of x rays in the auroral zone: 3. high time resolution studies,” *Journal of Geophysical Research (1896-1977)*, vol. 69, no. 21, pp. 4457–4479, 1964, ISSN: 2156-2202. DOI: 10.1029/JZ069i021p04457. [Online]. Available: <https://onlinelibrary.wiley.com/doi/abs/10.1029/JZ069i021p04457> (visited on 12/25/2023).

- [28] R. M. Millan *et al.*, “The balloon array for RBSP relativistic electron losses (BARREL),” *Space Science Reviews*, vol. 179, no. 1, pp. 503–530, Nov. 1, 2013, ISSN: 1572-9672. DOI: 10.1007/s11214-013-9971-z. [Online]. Available: <https://doi.org/10.1007/s11214-013-9971-z> (visited on 12/25/2023).
- [29] S. E. Harris *et al.*, “THEMIS ground based observatory system design,” *Space Science Reviews*, vol. 141, no. 1, pp. 213–233, Dec. 1, 2008, ISSN: 1572-9672. DOI: 10.1007/s11214-007-9294-z. [Online]. Available: <https://doi.org/10.1007/s11214-007-9294-z> (visited on 12/25/2023).
- [30] A. Pál *et al.*, “GRBAAlpha: A 1U CubeSat mission for validating timing-based gamma-ray burst localization,” in *Space Telescopes and Instrumentation 2020: Ultraviolet to Gamma Ray*, vol. 11444, SPIE, Dec. 13, 2020, pp. 825–833. DOI: 10.1117/12.2561351. [Online]. Available: <https://www.spiedigitallibrary.org/login.ezproxy.library.ualberta.ca/conference-proceedings-of-spie/11444/114444V/GRBAAlpha--a-1U-CubeSat-mission-for-validating-timing-based/10.1117/12.2561351.full> (visited on 08/23/2023).
- [31] N. Werner *et al.*, “CAMELOT: Cubesats Applied for MEasuring and LOcalising Transients mission overview,” in *Space Telescopes and Instrumentation 2018: Ultraviolet to Gamma Ray*, vol. 10699, SPIE, Jul. 6, 2018, pp. 672–686. DOI: 10.1117/12.2313764. [Online]. Available: <https://www.spiedigitallibrary.org/conference-proceedings-of-spie/10699/106992P/CAMELOT--Cubesats-Applied-for-MEasuring-and-LOcalising-Transients-mission/10.1117/12.2313764.full> (visited on 08/23/2023).
- [32] “MPPC (multi-pixel photon counter) s13360 series,” [Online]. Available: https://www.hamamatsu.com/content/dam/hamamatsu-photonics/sites/documents/99_SALES_LIBRARY/ssd/s13360_series_kapd1052e.pdf.
- [33] *Inorganic Scintillators for Detector Systems* (Particle Acceleration and Detection). Berlin/Heidelberg: Springer-Verlag, 2006, ISBN: 978-3-540-27766-8. DOI: 10.1007/3-540-27768-4. [Online]. Available: <http://link.springer.com/10.1007/3-540-27768-4> (visited on 12/26/2023).
- [34] P. Lecoq, “Scintillation detectors for charged particles and photons,” in *Particle Physics Reference Library: Volume 2: Detectors for Particles and Radiation*, C. W. Fabjan and H. Schopper, Eds., Springer International Publishing, 2020, pp. 45–89, ISBN: 978-3-030-35318-6. DOI: 10.1007/978-3-030-35318-6_3. [Online]. Available: https://doi.org/10.1007/978-3-030-35318-6_3 (visited on 12/27/2023).
- [35] H. Bichsel, *Stopping power of fast charged particles in heavy elements*: Jan. 1, 1991. DOI: <https://doi.org/10.6028/NIST.IR.4550>.
- [36] D. R. Mulville, “Nasa-std-4001: Electrical grounding architecture for unmanned spacecraft,” <https://standards.nasa.gov/standard/NASA/NASA-HDBK-4001>.
- [37] *Smartfusion2 system-on-module (m2s-fg484 som) hardware architecture*, Em-Craft Systems, 2019. [Online]. Available: <https://www.emcraft.com/som/m2s-fg484>.

- [38] *Igloo2 fpga and smartfusion2 soc fpga*, Microsemi, 2018. [Online]. Available: <https://www.microchip.com/en-us/products/fpgas-and-plds/system-on-chip-fpgas/smartfusion-2-fpgas>.
- [39] “Hamamatsu MPPC S13360 Series Technical Note,” [Online]. Available: https://www.hamamatsu.com/content/dam/hamamatsu-photonics/sites/documents/99_SALES_LIBRARY/ssd/mppc_kapd9008e.pdf.
- [40] H. Alva-Sánchez, A. Zepeda-Barrios, V. D. Díaz-Martínez, T. Murrieta-Rodríguez, A. Martínez-Dávalos, and M. Rodríguez-Villafuerte, “Understanding the intrinsic radioactivity energy spectrum from ^{176}Lu in LYSO/LSO scintillation crystals,” *Scientific Reports*, vol. 8, no. 1, p. 17310, Nov. 23, 2018, Publisher: Nature Publishing Group, ISSN: 2045-2322. DOI: 10.1038/s41598-018-35684-x. [Online]. Available: <https://www.nature.com/articles/s41598-018-35684-x> (visited on 04/21/2024).
- [41] G. Knoll, *Radiation Detection and Measurement*. Wiley, 2000, ISBN: 9780471073383. [Online]. Available: <https://books.google.ca/books?id=HKBVAAAAMAAJ>.
- [42] Z. Dali *et al.*, “Energy response of GECAM x and gamma-ray detector prototype,” Apr. 10, 2018.
- [43] J. Dixon *et al.*, “Evaluation of a silicon ^{90}Sr betavoltaic power source,” *Scientific Reports*, vol. 6, no. 1, p. 38182, Dec. 1, 2016, Publisher: Nature Publishing Group, ISSN: 2045-2322. DOI: 10.1038/srep38182. [Online]. Available: <https://www.nature.com/articles/srep38182> (visited on 06/08/2024).
- [44] “RockSat-x - NASA.” Section: Wallops Flight Facility. (), [Online]. Available: <https://www.nasa.gov/wallops/stem/rocksatx/> (visited on 06/07/2024).
- [45] K. Torigoe *et al.*, “Performance study of a large CsI(tl) scintillator with an MPPC readout for nanosatellites used to localize gamma-ray bursts,” *Nuclear Instruments and Methods in Physics Research Section A: Accelerators, Spectrometers, Detectors and Associated Equipment*, 11th International Hiroshima Symposium on Development and Application of Semiconductor Tracking Detectors, vol. 924, pp. 316–320, Apr. 21, 2019, ISSN: 0168-9002. DOI: 10.1016/j.nima.2018.08.039. [Online]. Available: <https://www.sciencedirect.com/science/article/pii/S0168900218309926> (visited on 08/23/2023).
- [46] Z. Li *et al.*, “Characterization of radiation damage caused by 23mev protons in multi-pixel photon counter (MPPC),” *Nuclear Instruments and Methods in Physics Research Section A: Accelerators, Spectrometers, Detectors and Associated Equipment*, vol. 822, pp. 63–70, Jun. 21, 2016, ISSN: 0168-9002. DOI: 10.1016/j.nima.2016.03.092. [Online]. Available: <https://www.sciencedirect.com/science/article/pii/S016890021630122X> (visited on 08/23/2023).

Appendix A: RADHEPT Electronics Schematics

A.1 Power Management Board

The power management board can be functionally divided into four sections which are described below.

A.1.1 Voltage Regulators - Digital Supply

The digital voltage levels required by the instrument are 3.3V (for the FPGA) and 2.5V for the ADC digital supply. The power management board first generates the 3.3V using a switching mode supply, and the 2.5 V from the 3.3V using a linear regulator. The switching regulator consists of a resistor divider, whose values are calculated appropriately to generate 2.5V from 3.3V (see Figure A.1).

A.1.2 Voltage Regulators - Analog Supply

This board element consists of two switching regulators, one for generating 5V and the other for generating +12V and -12V. The +5V is then converted to 2.5V for the ADC analog supply using a linear regulator. The switching regulator consists of a resistor divider, whose values are calculated appropriately to generate 2.5V from 3.3V. The +12V and -12V are used to power the amplifiers in the detector heads (See Figure A.2).

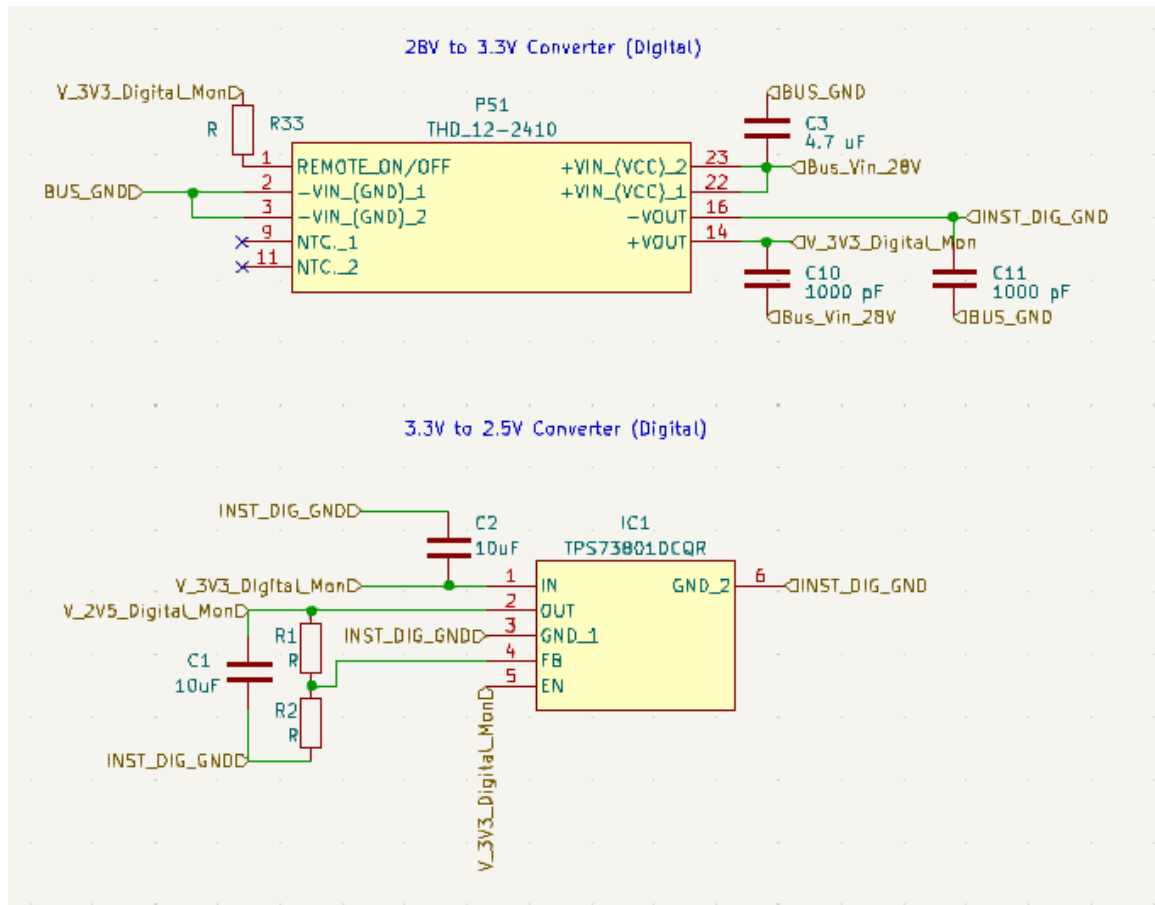


Figure A.1: Voltage Regulators - Digital.

A.1.3 Voltage Regulators - High Voltage Bias

The high-voltage bias is generated using a switching regulator from the 5V analog supply described in the previous section. The board consists of a Digital-to-Analog Converter (DAC) that generates a control voltage to set the output of the high voltage regulator. This DAC can be operated by the instrument FPGA to set the the voltage output. Further, the board also consists a resistor-divider and buffer Op-Amp to monitor the the high voltage. The output of the the Op-Amp is connected to a ADC which is read by the FPGA. This enables use of a closed-loop feedback system that can be used to set the high voltage supply (See Figure A.3).

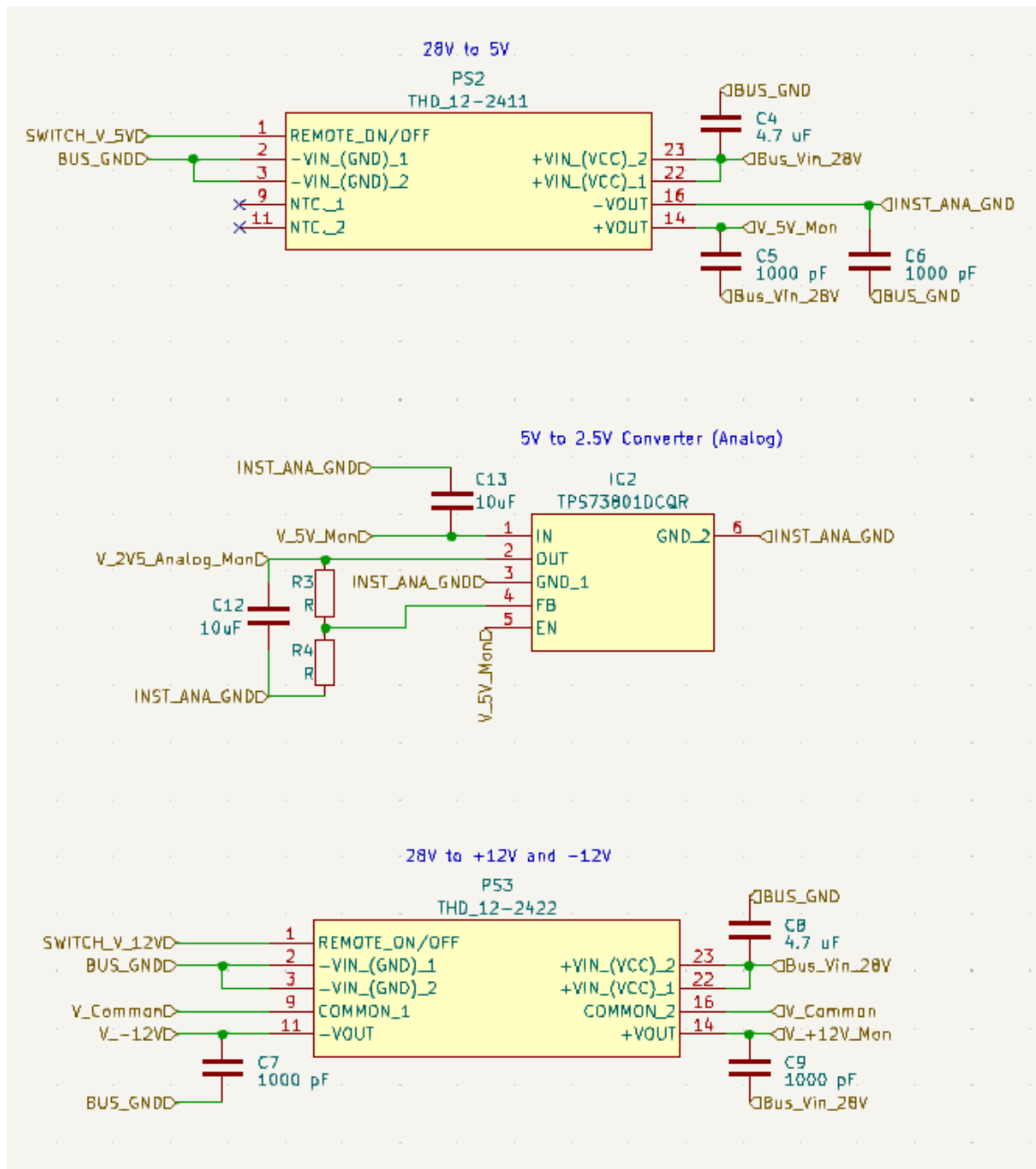


Figure A.2: Voltage Regulators - Analog.

A.1.4 Housekeeping - Voltage Current Sensors

This element of the board also consists of three voltage-current sensors that are used to monitor the voltage and current of the different internally generated levels. This data is serialized in the sensors and transferred to the instrument FPGA over a I2C interface (See Figure A.4).

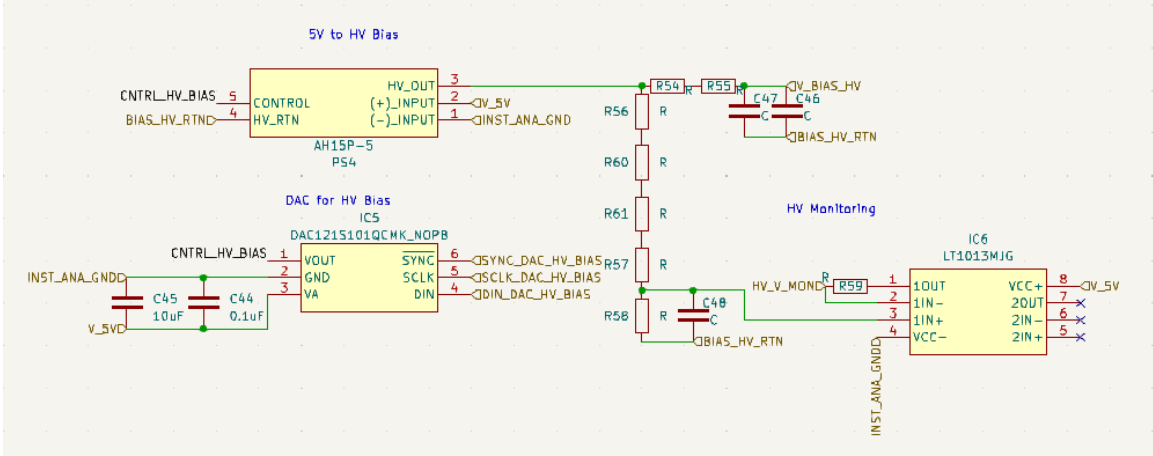


Figure A.3: Voltage Regulators - High Voltage.

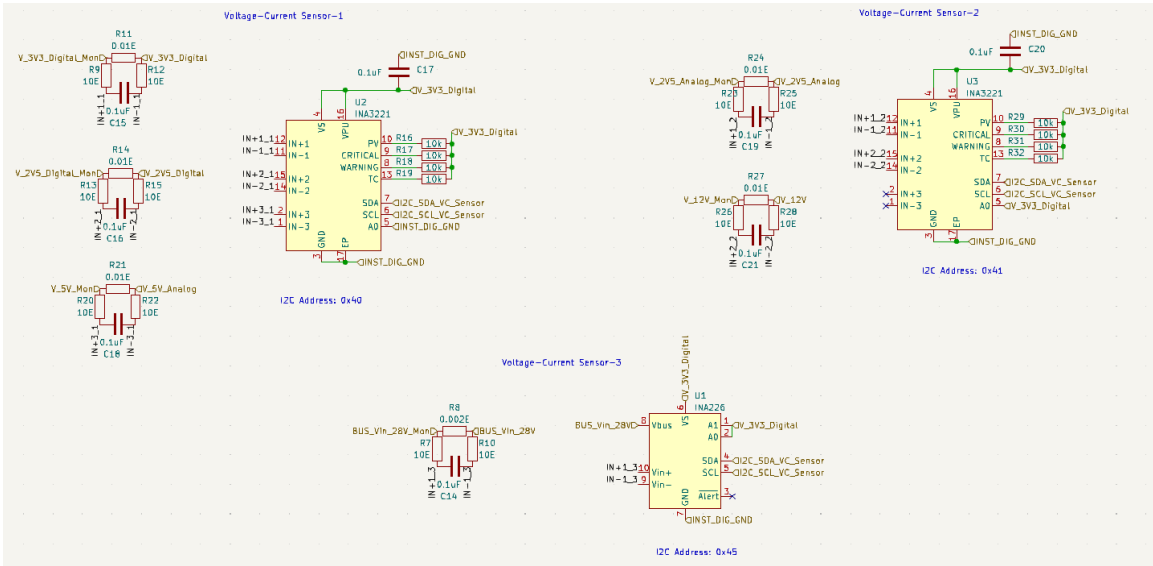


Figure A.4: Voltage Current Sensors.

A.1.5 Housekeeping - Thermistor Monitoring

This element of the board also consists of two Analog-to-Digital Converters (ADCs) that are used to monitor the the output voltage of thermistors. The thermistors chosen are Negative Temperature Coefficient (NTC) thermistors with a nominal resistance of 10 kOhms. They are connected through a resistor divider network to the ADC input channels. The ADCs have a serial output that can be used to read the voltage of all 16 channels (See Figure A.5).

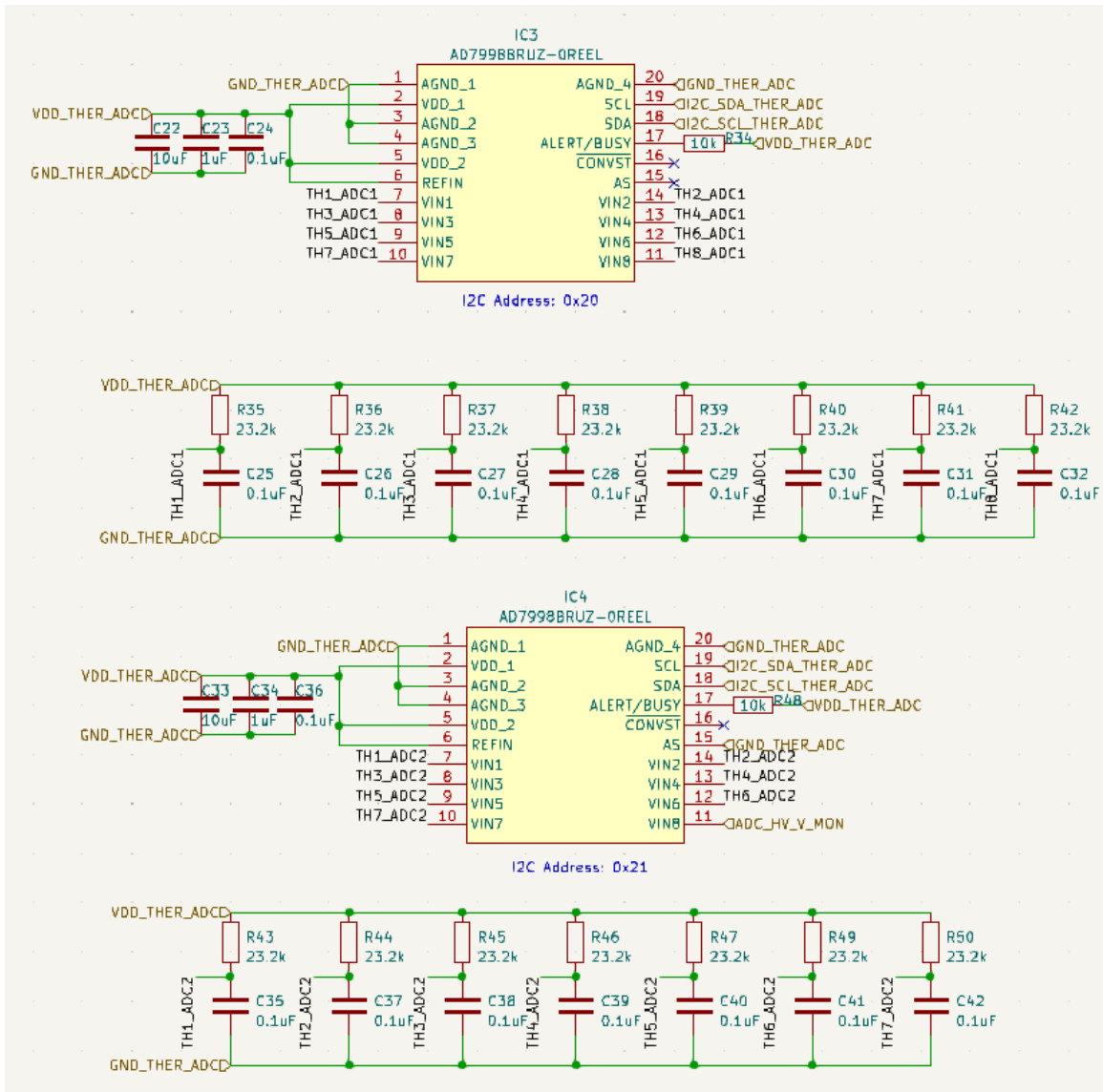


Figure A.5: Thermistor Monitoring.

A.2 Digital Processing Board

A.2.1 Peripherals RS-485/RS-232 Transceivers

This element of the board consists of both a RS-485 and RS-232 transceiver to transfer telemetry to the spacecraft. A hardware jumper is added that can be used to select either RS-485 or RS-232 (See Figure A.6).

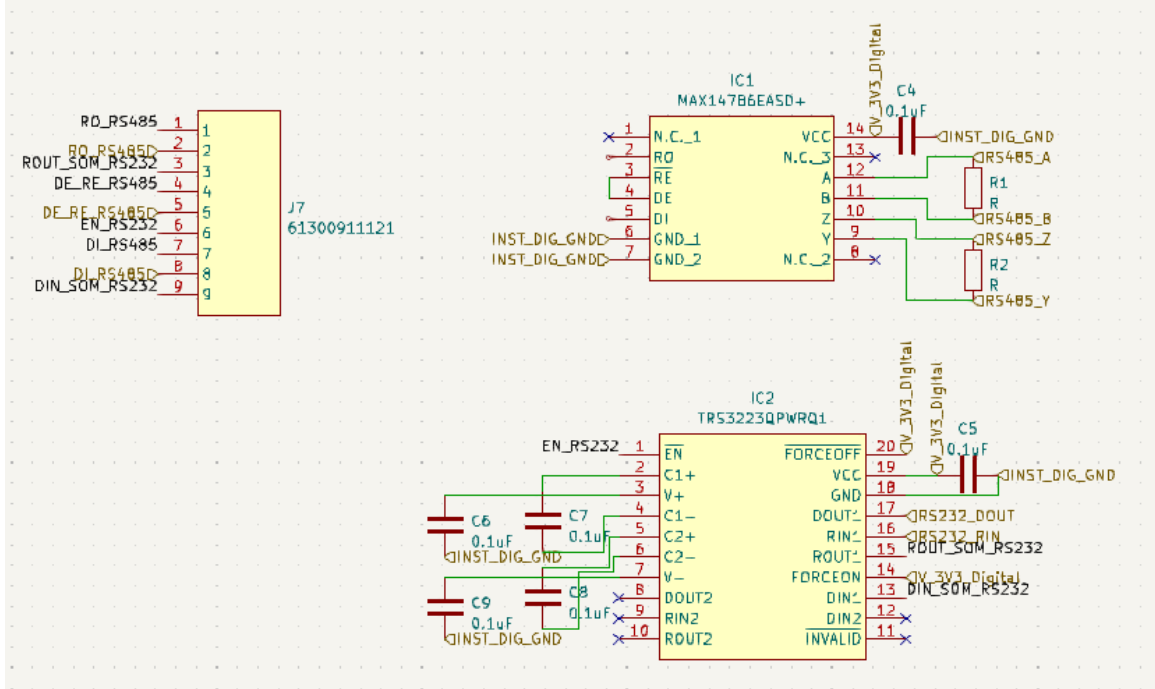


Figure A.6: RS-485 and RS-232 Transceivers.

A.2.2 On-Board Memory

This element of the board consists of three different memories of different sizes. To store different instrument parameters and variables, the SoM consists of a SPI flash memory chip. To store science data the board consists of a 1 GByte NAND Flash memory. The board also has an SD Card slot that can contain a 128 GByte SD card to store all instrument data on-board. The schematics for the NAND flash and SD Card are shown in Figures A.7 and A.8. An external switch is also added to the SD Card circuitry on the board to power cycle the SD Card if required.

A.2.3 Reset Watchdog and Real Time Counter

The board also contains a real time counter (RTC) that maintains a calendar time value which can be appended to the instrument data packets. The part chosen for this application also has a built-in watchdog feature that can be used to trigger an instrument reset in-case of any on-orbit faults. The chip also contains EEPROM to store instrument flight parameters. The IC can be powered by its independent coin

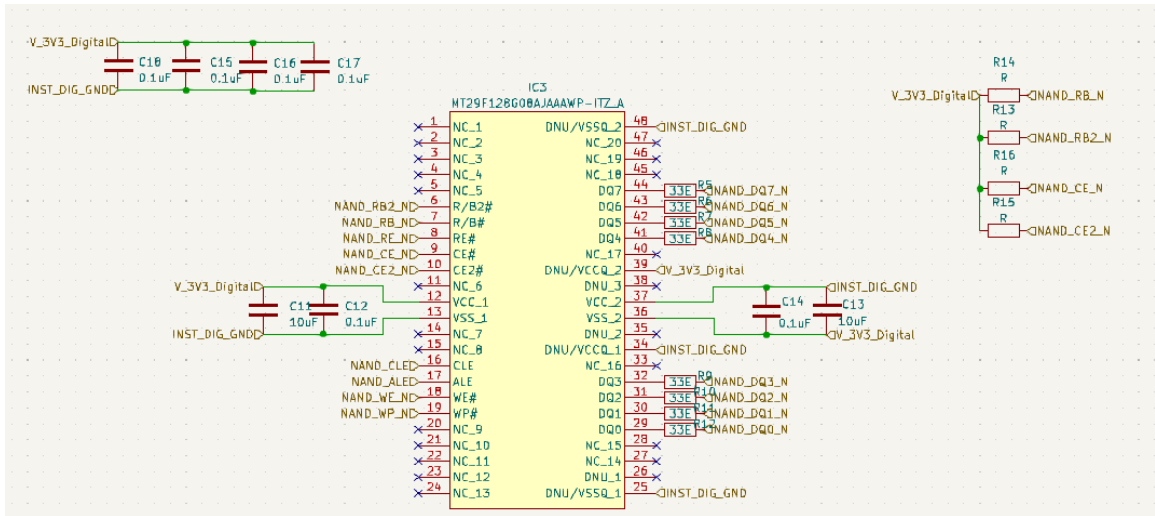


Figure A.7: NAND Flash.

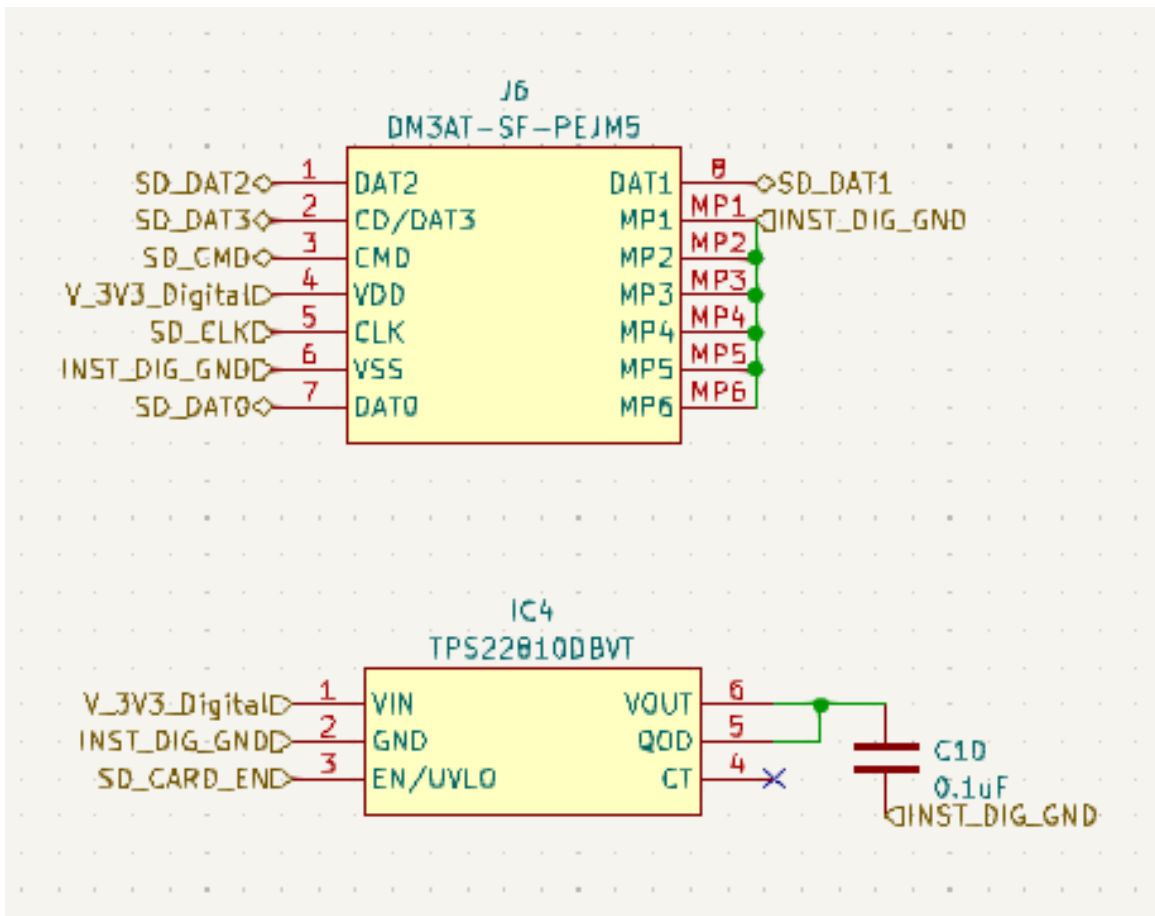


Figure A.8: SD Card.

battery and also has a trickle charge feature to charge the battery from the instrument power supply (See Figure A.9).

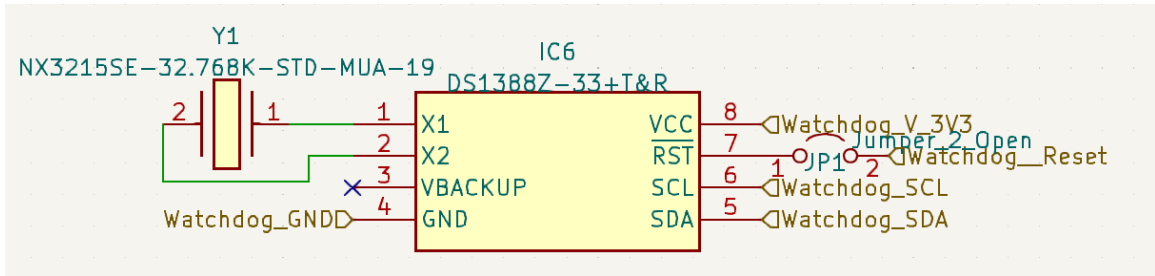


Figure A.9: Reset Watchdog and RTC.

A.3 Detector Interface Board

A.3.1 ADC

The ADC chosen has parallel interface with 12 data bits, and operates to a maximum sampling rate of 25 Msps. The ADC data is transferred to the FPGA using a 12 wire connector. The ADC requires a single ended clock input and the board has jumper provisions to select different operational modes. The schematics of the ADCs are shown in Figure A.10.

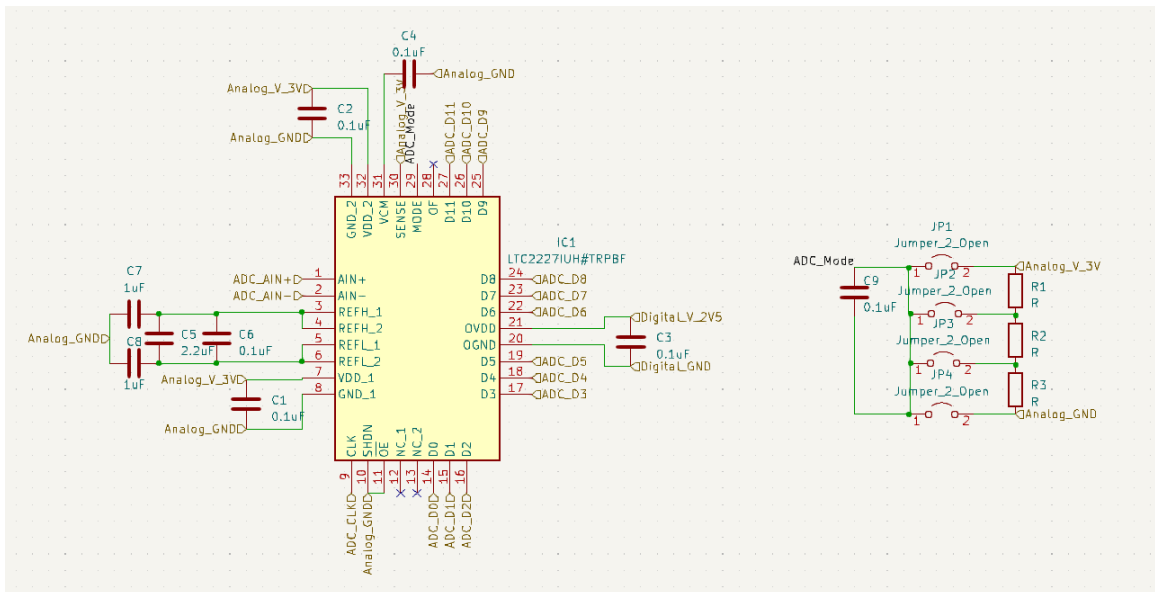


Figure A.10: ADC Schematic.